School of Science Department of Physics and Astronomy Master Degree in Physics

Characterization	of a	magneto-optical	trap	of	$^{87}\mathrm{Rb}$
		atoms			

Supervisor: Submitted by:

Prof. Francesco Minardi Letizia Loparco

Co-supervisor:

Prof. Marco Prevedelli

Academic Year 2024/2025

"Anni di voli pindarici fanno il nido sui rami degli alberi."

Alla mia famiglia.

Abstract

This thesis presents the optimization and characterization of a magneto-optical trap (MOT) setup for rubidium-87 atoms. The apparatus is designed to provide a source of cold atoms, with temperatures around 100 μ K, near the tip of a hollow-core photonic crystal fiber. The ultimate goal is to load the cold atomic cloud into the fiber to explore the unique properties of this hybrid system.

Since the number of captured atoms depends on the interplay between the magnetic field and detuning, a detailed study was conducted to investigate the number of trapped atoms as a function of different detuning values and magnetic field gradients. By comparing two measurement methods, it was determined that the MOT is capable of trapping approximately 10^7 rubidium atoms. The optimal magnetic field gradient and laser detuning frequency were found to be $B' = 9.32\,\mathrm{G/cm}$ and $\delta \approx -13\,\mathrm{MHz}$, respectively. Additionally, the number of captured atoms was found to be strongly dependent on the background pressure inside the MOT chamber. In this regard, it was observed that by closing the rubidium source valve, the pressure can be reduced by up to 80% over a 24-hour period, and one possible way to measure it could be through the background signal with the magnetic field gradient turned off. Then we analyzed the trap lifetime τ , which is also inversely proportional to the partial pressure of rubidium. Under optimal conditions, we obtained a trap lifetime of 0.31 s.

Furthermore, a temperature estimation of the atomic cloud was performed using the time-of-flight (TOF) method. The velocity distribution along the x-axis, which lie in the imaging plane, was captured with a CMOS camera and yielded temperature of $T_x = (252 \pm 20) \,\mu\text{K}$.

These results provide essential insights into the optimization of the MOT parameters and lay the foundation for future studies involving the loading of cold atoms into hollow-core photonic crystal fibers.

Contents

A	bstra	ract		i
Li	st of	of Figures		iv
Li	st of	of Tables		ix
In	trod	duction		1
1	Cha	napter 1		3
	1.1	Emission and absorption of radiation by atoms		3
		1.1.1 Hamiltonian system		4
		1.1.2 Rabi model		5
		1.1.3 Spontaneous and stimulated emission		7
		1.1.4 Bloch equation and total scattering rate		8
	1.2	2 Manipulating atoms with photons		10
		1.2.1 Dissipative and reactive processes		10
		1.2.2 Manipulation of internal and external degrees of free	dom	12
		1.2.3 Characteristic times		13
	1.3	B Magneto-Optical trap		14
		1.3.1 Transfer of momentum		14
		1.3.2 Doppler cooling and optical molasses		16
		1.3.3 Doppler cooling limit		18
		1.3.4 1D model of the MOT		20
2	Cha	napter 2		25
	2.1	General description		25
	2.2	2 Vacuum chamber		25
	2.3	B Laser system		28
		2.3.1 Cooler and Repumper		29
		2.3.2 Master laser		31
	2.4	4 Photo-detector		32
		2.4.1 Number of atoms estimation		33
		2.4.2 Trap lifetime estimation		34
	2.5	5 Imaging system		35
		2.5.1 Temperature estimation		35

3	Cha	apter 3	39
	3.1	Number of atoms estimation	39
		3.1.1 First method	39
		3.1.2 Second method	42
	3.2	Optimal Magnetic Field gradient	46
	3.3	Studying Pressure	47
	3.4	Trap lifetime estimation	49
	3.5	Temperature estimation	52
	3.6	Conclusions	58
\mathbf{A}	App	pendix	59
	A.1	Hall probe	59
		Hollow-core photonic crystal fiber	61
		A.2.1 Optical fiber	61
		A.2.2 Polarisation Maintaining Fibres	63
		A.2.3 Hollow-Core Photonic Crystal fiber	63
	A.3	Photodetector Gain	65
	A.4	Saturated Absorption Spectroscopy	66
	A.5	$^{87}\mathrm{Rb}$ and $^{85}\mathrm{Rb}$ D_2 transition hyperfine structure	70
	A.6	Results	72
	-	A.6.1 Number of atoms estimation-First method	72
		A.6.2 Number of atoms estimation-Second method	75

List of Figures

1.1	The interacting systems: light field (L) , atom system (A) , vacuum system (V) , and the various couplings V_{AL} and V_{AV}	4
1.2	Rabi frequency on $\omega_L = \omega_A$ and off-resonance $\omega_L \neq \omega_A$	6
1.3	Excitation rate R_{sc} , in units of Γ , as a function of the detuning δ . Here R_{sc} and Γ are denoted as γ_p and γ , respectively. Credits: [17]	9
1.4	Lorentzian absorption profile and dispersive phase index	11
1.5	A simplified depiction of the light pressure acting on the two-level atom. Photon absorption a) and its consequent exchange of momentum b) and emission in c). Credits: [23]	15
1.6	Moving atom in the laboratory reference frame	16
1.7	\vec{F}_+, \vec{F} and F_{OM} are shown in red, green and blue trace respectively (they are calculated for detuning $\delta = -1.3\Gamma$ and saturation $s_0 = 3$. Here the absorption rate is γ . Credits: [23]	17
1.8	Representation of the random walk of atomic momentum due to photon recoil during absorption and spontaneous emission. The blue trajectory illustrates the stochastic diffusion process, while the red arrows indicate the average force that drives the atom's motion	18
1.9	Schematic 1D MOT configuration, with two counter-propagating beams and a magnetic field of quadrupole symmetry.	20
1.10	The Zeeman splitting of hyperfine energy levels occurs in the presence of a magnetic field B_z . The energy levels, identified by the quantum numbers F and F_z , shift proportionally to the applied field due to the Zeeman effect. For a magnetic field of approximately $B \sim 1$ G, the resulting splitting between magnetic sublevels is on the order of MHz, while the hyperfine structure itself lies on the order of GHz	22
1.11	Selective absorption of the circularly polarized light	23
	Schematic representation of the Zeeman shift for a simple atomic structure with $F=0$ and $F'=1$ in a one-dimensional MOT. The magnetic field gradient $\partial_z B$ causes a splitting of the magnetic sublevels, with σ^+ and σ^- polarized laser beams interacting differently with the atoms depending on their position along the z-axis. The solid arrows indicate the laser frequencies, red-detuned from resonance, while the dotted arrows represent the Doppler-shifted frequencies	20
	experienced by the moving atoms. Credits: [23]	24

2.1	The vacuum chamber setup with all its components: the vacuum chamber is painted purple, the MOT optical system in red, the MOT coils in orange, the ionic pump in black, the Rb source on the left side in dark orange, and the HCPCF port in green, located behind the coils. Finally, on the west side, there is a glass viewport for the CMOS camera. In the text the top-bottom direction is referred to as zenith-nadir. Credits: [25]	26
2.2	Signal of the Hall prove switching off (left) and on (right) the magnetic field.	27
2.3	D_2 transition, the reference for the Master laser in orange, for the Cooler in red and for the Repumper in blue.	28
2.4	Laser system of the Cooler and Repumper lasers. The different stages of amplification, SHG and beat note locking are shown	29
2.5	The fluorescence of background rubidium gas was acquired on the oscilloscope, switching on and off AOM through the DDS monitored by FPGA	30
2.6	Scheme of the positions of cooling and repumping transition frequencies with relative to Master frequency.	31
2.7	Master laser setup schematics	32
2.8	The photodetector system circuit with a transimpedance amplifier (TIA). $$. $$.	33
2.9	Maxwell-Boltzmann probability distribution of speeds for $T=100\mathrm{K}$ (blue), $T=200\mathrm{K}$ (orange), $T=300\mathrm{K}$ (green)	36
2.10	Time sequence of a single photo MOT	37
3.1	Capture dynamics of the MOT photoemission for $B' = 9.32 \text{G/cm}$ value of the magnetic field gradient, as recorded on the oscilloscope for various beat-note frequencies (see Appendix A.6 for other results)	40
3.2	Close-up view of the MOT photoemission near the peaks, showing how the signal evolves over time for different beat-note frequencies $ BN_{photo} $	40
3.3	Lorentzian fit for $B' = 9.32 \mathrm{G/cm}$ (see A.6 for other results)	41
3.4	Time traces of the MOT fluorescence for different cooler beat-note frequencies (from 1032MHz to 1044MHz) and for a magnetic field gradient of $B'=9.32\text{G/cm}$. These oscilloscope measurements illustrate how the loading dynamics vary with detuning and magnetic field gradient (see Appendix A.6), allowing us to identify the conditions that maximize the number of trapped atoms	43
3.5	Measured peak voltages for $B' = 9.32$ G/cm as a function of the cooler beat- note frequency, with error bars representing the standard deviation of the	10
	background subtracted to set the offset (see A.6 for others)	44
3.6	Above: Background signals. Below: Stabilized voltage measurements. Both corresponding to a specific magnetic field gradient value ($B' = 9.32 \mathrm{G/cm}$), plotted against the cooler beat-note frequency. The error bars represent the	
3.7	standard deviations of the background, subtracted to set the offset	44
J.1	magnetic field gradient value of $B' = 9.32 \mathrm{G/cm}$. The error bars indicate the uncertainties in the atom number measurements (see A.6 for other results).	45
3.8	Comparison of the measured optimal voltage peak (V_{max}) and the corresponding number of trapped atoms as functions of the magnetic field gradient	46
	named of trapped atoms as functions of the magnetic held gradient	-10

3.9	MOT fluorescence at $B' = 9.32 \text{G/cm}$ as a function of the cooler beat-note frequency, illustrating the approach to the optimal detuning near 1040 MHz.	46
3.10	Evolution of the background voltage (V_{bkg}) over time, showing how the pressure	10
	in the vacuum chamber changes under different operating conditions (e.g., valve open or closed). The color-coded points indicate individual measurements with	
	their respective uncertainties, illustrating how the rubidium source and valve	
	states affect the measured voltage (and thus the chamber pressure)	47
2 11	Background voltage (V_{bkg}) measured at various cooler beat-note frequencies,	41
0.11	illustrating how the chamber pressure (inferred from the background signal)	
	changes under different conditions. The color-coded points represent measure-	
	ments taken at different times or valve states	48
3 19	Example of the MOT loading curve at $B' = 9.32 \mathrm{G/cm}$ with a cooler beat-note	40
0.12	of 1040 MHz. The original and smoothed fluorescence signals over time, showing	
	the removal of a spike	49
2 12	Example of the MOT loading curve at $B' = 9.32 \mathrm{G/cm}$ with a cooler beat-note	40
0.10	of 1040 MHz. A fit to the data without the spike for determining the lifetime	
	τ , with the best-fit value indicated in the legend	49
3 14	(Left) trap lifetime τ as a function of the cooler beat-note frequency at a fixed	10
0.11	magnetic field gradient ($B' = 9.32 \mathrm{G/cm}$). (Right) τ values at the optimal	
	detuning for each magnetic field gradient, illustrating how the trap lifetime	
	depends on both detuning and field strength	50
3 15	Variation of the trap loss rate τ^{-1} with the measured background pressure,	30
0.10	illustrating the relationship $\tau^{-1} \propto P$ discussed in Section 3.3	52
3.16	Camera at the Zenith side of the vacuum chamber, and a exposure time of the	5–
0.10	camera $t_{exp} = 0.2 \text{ ms} \dots \dots \dots \dots \dots \dots \dots \dots \dots$	53
3 17	Camera at the West side. Left image: Compensation coils acting on Zenith-	33
0.11	Nadir axis, Right image: no compensation field applied	53
3.18	A subset of images illustrating the MOT expansion at various times (1, 3, 4, 5,	
0.10	7, 9, 10, 11, 12, 14, 16, 18 ms) after the laser and magnetic field are switched	
	off. The sequence clearly shows the gradual spread of the atomic cloud once	
	the confining forces are removed	54
3.19	Comparison of the center of mass (red dot) without background in the MOT	
	images for coil currents of $+2A$ (left) and $-2A$ (right)	55
3.20	(Left) Evolution of the center-of-mass coordinates (x,y) as a function of the	
	time-of-flight (tof). (Right) Second moments of the atom cloud's position	
	distribution (σ_x^2, σ_y^2) plotted against tof^2 . These measurements illustrate both	
	the shifting center of mass and the expanding spatial width of the atomic cloud	
	over time. Note that x and y coordinates refer to the plane captured by the	
	camera positioned on the west side of the chamber	56
3.21	Second moments of the atomic cloud's position distribution plotted against	
	tof^2 along with the corresponding fits. (Left) Data processed by selecting a	
	region of interest (ROI). (Right) Data processed by applying a threshold set to	
	three times the background level, setting all pixel values below this threshold	
	to zero	56
3.22	squared widths σ_x^2 and σ_y^2 of the narrower Gaussian component, plotted as a	
	function of tof^2	57

A.1	Schematic representation of the Hall effect in a rectangular conductor. A current I flows from left to right, a magnetic field B is applied upward, and	
	the resulting Lorentz force deflects the charge carriers to one side, generating	50
A.2	the Hall voltage V_H	59
11.2	(X), the internal amplifier, and the three pins (supply, ground, and output).	60
A.3	(a) Cross section of a typical step index optical fibre, highlighting its main components. (b) Visual representation of Snell-Descartes law. (c) Schematic view of light ray guiding in a step index fibre: the incoming light is refracted in the fibre core, if and if its incidence angle at the core-cladding interface is greater than the critical value for total internal reflection θ_c , then the ray can be guided by the fibre	62
A.4	Cross section images of various types of PM fibres. Credits:[41]	63
A.5	Modal content representation of the three different optical guiding fibres: (a) Total Internal Reflection (TIR); (b) Photonic Band Gap (PBG); (c) Inhibited	0.4
A.6	Coupling (IC)	64
A.7	to the laser intensity	66 67
A.8	Saturated absorption spectrum of a Rb vapor	67
A.9	Schematic of the crossover resonance system	68
	Saturated absorption spectrum of a three-level atom	68 70
A.12	Rubidium 85 $D2$ transition hyperfine structure, with frequency splittings between the hyperfine energy levels. Credits: [28]	71
A.13	8 Capture dynamics of the MOT photoemission for $B' = 6.66 \mathrm{G/cm}$, as recorded on the oscilloscope for various beat-note frequencies.	72
A.14	Capture dynamics of the MOT photoemission for $B' = 7.99 \mathrm{G/cm}$, as recorded on the oscilloscope for various beat-note frequencies	72
A.15	Capture dynamics of the MOT photoemission for $B' = 10.66 \mathrm{G/cm}$, as recorded on the oscilloscope for various beat-note frequencies	73
A.16	Lorentzian fit for $B'=6.66\mathrm{G/cm}$	73
A.17	Lorentzian fit for $B' = 7.99 \mathrm{G/cm}.$	74
	Lorentzian fit for $B' = 10.66 \mathrm{G/cm}$	74
	Time traces of the MOT fluorescence for different cooler beat-note frequencies (from $1032\mathrm{MHz}$ to $1044\mathrm{MHz}$) and magnetic fields gradient $B'=6.66\mathrm{G/cm}$.	75
	Time traces of the MOT fluorescence for different cooler beat-note frequencies (from $1032 \mathrm{MHz}$ to $1044 \mathrm{MHz}$) and magnetic fields gradient $B' = 11.99 \mathrm{G/cm}$.	75
A.21	Time traces of the MOT fluorescence for different cooler beat-note frequencies (from $1032\mathrm{MHz}$ to $1048\mathrm{MHz}$) and magnetic fields gradient $B'=14.65\mathrm{G/cm}$.	76

	Measured peak voltages for $B' = 6.66 \mathrm{G/cm}$ as a function of the cooler beat- note frequency, with error bars representing the standard deviation of the	
	background subtracted to set the offset	76
	Measured peak voltages for $B' = 7.99 \mathrm{G/cm}$ as a function of the cooler beat-	
	note frequency, with error bars representing the standard deviation of the background subtracted to set the offset	77
A.24	Measured peak voltages for $B' = 11.99 \mathrm{G/cm}$ as a function of the cooler beat-	* *
	note frequency, with error bars representing the standard deviation of the	
A 25	background subtracted to set the offset	77
	note frequency, with error bars representing the standard deviation of the	
	background subtracted to set the offset	78
	Number of trapped atoms as a function of the cooler beat-note frequency for $P' = 6.66 C / cm$. The error bars indicate the uncertainties in the stem number.	
	B'=6.66 G/cm. The error bars indicate the uncertainties in the atom number measurements.	78
A.27	Number of trapped atoms as a function of the cooler beat-note for $B'=$	
	7.99 G/cm frequency for four different magnetic field gradient values .The error bars indicate the uncertainties in the atom number measurements	79
A.28	Number of trapped atoms as a function of the cooler beat-note frequency for	19
	$B' = 11.99 \mathrm{G/cm}$. The error bars indicate the uncertainties in the atom number	
	measurements	79
	Number of trapped atoms as a function of the cooler beat-note frequency for $B' = 14.65 \mathrm{G/cm}$. The error bars indicate the uncertainties in the atom number	
	measurements	80

List of Tables

3.1	Number of trapped atoms and the width Δf (MHz) for different magnetic field	
	gradient values	42
3.2	Optimal detuning in terms of δ/Γ and corresponding atom numbers (N_a) for	
	different magnetic field gradients B'	45
3.3	Ion pump currents compared to the background voltage. Both follows from left	
	to right the temporal sequence in Fig. 3.10	48
3.4	Values of τ obtained from the fit of seven independent measurements with a	
	magnetic field gradient of $B' = 9.32$ G/cm at $ BN_{load} = 1040$ MHz	50
A.1	Photodiode gain (in dB) and the photodiode voltage (PD) at an OD setting of	
	34 dB	65
A.2	Power values before (P^{in}) and after (P^{out}) applying the ND filter	65

Introduction

Quantum mechanics has revolutionized our understanding of nature, opening the door to entirely new domains of physics. This transformation necessitated the development of innovative experimental tools capable of probing and manipulating quantum systems with unprecedented precision. Among these advancements, laser cooling has played a fundamental role.

The concept of laser cooling was first proposed in 1975 by Hänsch and Schawlow [1] and by Wineland and Dehmelt [2], and later realized experimentally by Steven Chu, Claude Cohen-Tannoudji, and William D. Phillips. Their pioneering work on laser cooling techniques earned them the 1997 Nobel Prize in Physics [3]. As a result, laser-cooled atoms have become a powerful tool in fundamental research and applications, such as quantum sensors [4], atomic clocks [5], interferometry [6], and quantum simulation [7]. Notable developments include optical lattices[8], and studies of new quantum phases such as the Bose-Einstein condensate[9] and the supersolidity [10].

While laser cooling significantly reduced atomic motion, additional techniques were needed to confine atoms in specific regions of space. This leads to the realization of the Magneto-Optical Trap (MOT). First demonstrated in 1987 at AT&T Bell Labs, the MOT combined laser cooling with magnetic field gradients to confine neutral atoms, enabling controlled manipulation of atomic ensembles and opening new frontiers in quantum optics and precision measurements.

The focus of this thesis is the characterization of a Magneto-Optical Trap (MOT). In Chapter 1, fundamental concepts of atomic physics are reviewed, including the Hamiltonian of the atom-light interaction, with particular focus on the two-level Rabi model, as well as the principles underlying optical molasses and magneto-optical trapping. The Chapter 2 describes the experimental setup and provides a comprehensive overview of all the components used in the experiment. Finally, Chapter 3 presents and analyzes the obtained results, primarily focusing on the number of trapped atoms and the temperature of the atomic cloud. Additionally, considerations about background pressure are discussed, along with the study of the atomic trap lifetime.

Magneto-Optical trap theory

The interaction between atoms and light plays a fundamental role in atomic physics, serving as the basis for techniques such as laser cooling, trapping, and quantum state manipulation. Among these techniques, Magneto-Optical Traps (MOTs) have become the standard tool for cooling and trapping neutral atoms, particularly rubidium (Rb). The technology behind MOTs has advanced significantly, to the point where compact, chip-scale devices have been developed.

To fully grasp the principles behind atom trapping, it is essential to analyze how atoms interact with light. This requires a detailed examination of the system's Hamiltonian and the fundamental physical processes governing these interactions, namely absorption, spontaneous emission, and stimulated emission. In particular, the behavior of a quasi-two-level atomic system in the presence of an external electric field is explored. While this approach does not fully describe all physical processes (most notably, spontaneous emission is initially neglected) it provides a solid foundation for understanding the underlying physics of atom trapping.

This theoretical framework allows for the manipulation of both the internal and external degrees of freedom of an atom using photons. For our purposes, we focus on optical pumping as a means of controlling the internal degrees of freedom. By exploiting the resonance of circularly polarized light, it is possible to selectively populate specific hyperfine sublevels. Regarding external degrees of freedom, we primarily consider dispersive forces, which arise from the exchange of linear momentum between an incident photon and the atom during a resonant scattering process. However, for a more comprehensive description, other processes such as the light shift (AC Stark shift) for internal degrees of freedom manipulation and dissipative forces (dipole force) for external degrees of freedom must also be considered

With these concepts established, we proceed to a detailed discussion of Doppler cooling, a mechanism used to slow down atoms, along with its fundamental limitations. Finally, we introduce the Magneto-Optical Trap (MOT) as a method for confining atoms within a specific spatial region.

1.1 Emission and absorption of radiation by atoms

In this section, the Hamiltonian describing the atom-radiation system, fundamental for studies on laser cooling, will be introduced. The interaction will be considered with a monochromatic light field of frequency ω_L and a two-level atomic system for simplicity.

The atom consists of a ground state and an excited state, separated by an energy difference $E_e - E_g = \hbar \omega_A$ The approximation of the laser as a classical driving force can be made because the laser field contains a large number of photons. However, by making this approximation, an important phenomenon remains unexplained: spontaneous emission, which occurs when the radiation is treated as a quantum mechanical field, a fully quantum mechanical phenomenon [11]. Hence, introducing the vacuum field, which must be treated quantum mechanically, resolves this problem.

1.1.1 Hamiltonian system

Building upon the previous considerations, the total Hamiltonian of the system is described. The atomic medium is assumed to be very dilute, so that atom-atom interactions can be neglected.

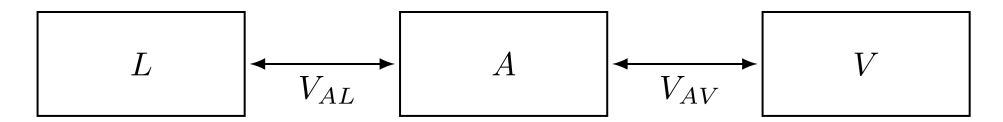


Figure 1.1. The interacting systems: light field (L), atom system (A), vacuum system (V), and the various couplings V_{AL} and V_{AV} .

The interacting components are shown in Fig. 1.1, where L is the light system, A the atom system and V the vacuum system. V_{AL} and V_{AV} are the respective couplings. Hence the total Hamiltonian is:

$$\hat{H} = \hat{H}_A + \hat{H}_V + \hat{V}_{AL} + \hat{V}_{AV} \tag{1.1}$$

Where:

•
$$\hat{H}_A = \hat{H}^{ext} + \hat{H}^{int} = \frac{\vec{P}}{2M} + \hbar\omega_A |e\rangle \langle e|$$

•
$$\hat{H}_V = \sum_j \hbar \omega_j \left(\hat{a}_j \hat{a}_j^+ + \frac{1}{2} \right)$$

•
$$\hat{V}_{AL} = -\hat{\vec{d}} \cdot \vec{E}_L(\vec{R}, t)$$

•
$$\hat{V}_{AV} = -\hat{\vec{d}} \cdot \vec{E}(\vec{r})$$

Here \vec{P} and M are the momentum and mass of the center of mass, \hat{a}_j , \hat{a}_j^+ are annihilation and creation operators of the vacuum electromagnetic modes $E(\vec{r}) = i \sum_j E_j a_j \epsilon_j e^{i\vec{k}_j \cdot \vec{r}} + \text{h.c.}$, $\hat{\vec{d}} = d\vec{\epsilon}_z(|e\rangle \langle g| + |g\rangle \langle e|)$ is the dipole operator and $\vec{E}_L(\vec{r},t) = \vec{E}_0 \cos(\omega_L t + \phi(\vec{r}))$ is the laser field

Since V represents a large system with an infinite number of degrees of freedom, V_{AV} introduces fluctuations in the evolution of A. The evolution of A is influenced by these fluctuations, leading to two distinct regimes. When the interaction time satisfies $t \ll 1/\Gamma$, spontaneous emission can be neglected, and the evolution of the system A+L is described by the Schrödinger equation. Conversely, for $t \gg 1/\Gamma$, multiple spontaneous emission processes occur, which are best described by a master equation or a Langevin equation [12].

The semiclassical picture is now analyzed in the interaction regime $t \ll 1/\Gamma$, where spontaneous emission can be neglected. Consequently, the vacuum field in Eq. (1.1) can be ignored, and a near-resonant classical field is considered. This system is described by the Rabi model.

1.1.2 Rabi model

In this section the coherent evolution of the amplitudes of a two-level atom in strong near-resonant classical field is introduced, the so-called Rabi Model. To visualize the internal dynamics and how the population of each level is affected, the new Hamiltonian, excluding the vacuum field, is recalled:

$$\hat{H}_{tot} = \hat{H}_A + \hat{V}_{AL} \tag{1.2}$$

$$\hat{H}_A = \begin{bmatrix} E_g & 0\\ 0 & E_e \end{bmatrix} = \begin{bmatrix} 0 & 0\\ 0 & \hbar \omega_A \end{bmatrix}$$
 (1.3)

Using the dipole approximation, the spatial phase factor of the electric field \vec{E}_L , which appears in the cosine term, can be neglected [11]. Consequently, the perturbation term $\vec{H}_{AL} = -\hat{d} \cdot \vec{E}_L(\vec{r},t)$ takes the form:

$$\begin{cases}
\hat{d} = d\vec{\epsilon}_z (|e\rangle \langle g| + |g\rangle \langle e|) = d\vec{\epsilon}_z (\sigma_+ + \sigma_-) \\
\vec{E}_L = \vec{\epsilon}(\vec{r}) E_0(\vec{r}) \cos(\omega_L t) = \frac{1}{2} \vec{\epsilon}(\vec{r}) E_0(\vec{r}) \left[e^{i(\omega_L t)} + e^{-i(\omega_L t)} \right]
\end{cases}$$
(1.4)

Using the rotating wave approximation [11], is possible to write in matrix form:

$$\hat{H}_{tot} = \frac{\hbar}{2} \begin{bmatrix} 0 & \Omega(\vec{r})e^{i\omega_L t} \\ \Omega(\vec{r})e^{-i\omega_L t} & 2\omega_A \end{bmatrix}$$
 (1.5)

where $\Omega(\vec{r}) = -dE_0(\vec{r})\vec{\epsilon}_z \cdot \vec{\epsilon}(\vec{r})/\hbar$ is the Rabi frequency at resonance, and for the simplest case, i.e. of a laser plane wave, $\Omega(\vec{r}) = \Omega$ since the amplitude and polarization of the laser electric field don't depend on \vec{r} . Let's apply a rotating frame of reference to the dynamics at the same frequency as the driving field ω_L :

$$\hat{H}_{tot} = \frac{\hbar}{2} \begin{bmatrix} \omega_L & \Omega \\ \Omega & 2\omega_A - \omega_L \end{bmatrix}$$
 (1.6)

Now let's see the dynamics of the system through the time-dependent Schrödinger equation assuming the atom to be in the state $|g\rangle$ at t=0.

$$i\hbar \frac{\partial |\psi(t)\rangle}{\partial t} = \hat{H}(t) |\psi(t)\rangle$$
 (1.7)

whose eigenvalues read:

$$\begin{cases}
E_{+} = \frac{\hbar}{2} \left[\omega_{A} + \sqrt{\delta^{2} + \Omega^{2}} \right] \\
E_{-} = \frac{\hbar}{2} \left[\omega_{A} - \sqrt{\delta^{2} + \Omega^{2}} \right]
\end{cases}$$
(1.8)

with $\delta = \omega_A - \omega_L$.

The corresponding eigenstates are

$$\begin{cases} |\psi_{+}\rangle = e^{-i\phi/2}\cos\left(\frac{\theta}{2}\right)|g\rangle + e^{+i\phi/2}\sin\left(\frac{\theta}{2}\right)|e\rangle \\ |\psi_{-}\rangle = -e^{-i\phi/2}\sin\left(\frac{\theta}{2}\right)|g\rangle + e^{+i\phi/2}\cos\left(\frac{\theta}{2}\right)|e\rangle \end{cases}$$
 (1.9)

with

$$\theta = \tan^{-1} \left(\frac{2\hbar\Omega}{E_g - E_e} \right) \tag{1.10}$$

Subtracting $|\psi_{+}\rangle$ and $|\psi_{-}\rangle$ the new superposition initial state can be obtained $|\psi(t=0)\rangle = |g\rangle$ and then applying the usual time dependence it's possible to find the evolution state of $|\psi(t=0)\rangle$ as:

$$|\psi(t)\rangle = e^{+i\phi/2} \left[e^{-iE_{+}t/\hbar} \cos\left(\frac{\theta}{2}\right) |\psi_{+}\rangle - e^{-iE_{-}t/\hbar} \sin\left(\frac{\theta}{2}\right) |\psi_{-}\rangle \right]$$
(1.11)

So the probability of finding the system in the state $|e\rangle$ at time t, after some easy algebra, is:

$$P_e(t) = |\langle e|\psi(t)\rangle|^2 = \sin^2\theta \sin^2\left(\frac{E_+ - E_-}{2\hbar}t\right) = \frac{\Omega^2}{\delta^2 + \Omega^2}\sin^2\left(\frac{\sqrt{\delta^2 + \Omega^2}}{2}t\right). \tag{1.12}$$

Hence if the laser is on resonance $\omega_L = \omega_A$ then the electron oscillates with maximum amplitude between $|g\rangle$ and $|e\rangle$, otherwise the population is not fully transmitted to the excited level. This behavior can be observed in Fig. 1.2:

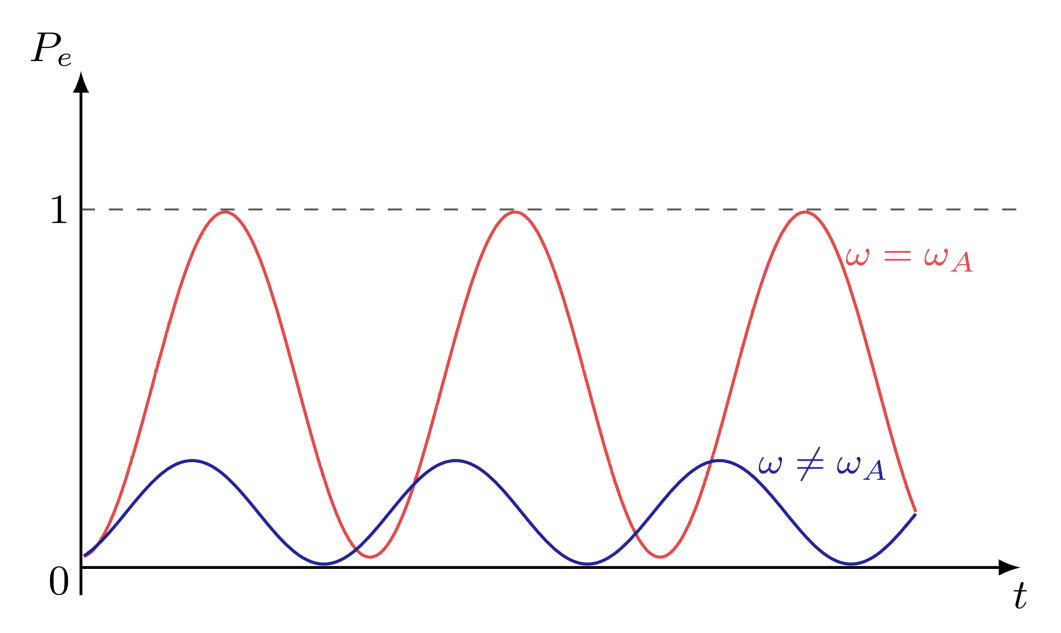


Figure 1.2. Rabi frequency on $\omega_L = \omega_A$ and off-resonance $\omega_L \neq \omega_A$.

As previously mentioned, due to the presence of a classical field in this dynamics, the phenomenon of spontaneous emission is ignored. However, this can be introduced through the Jaynes-Cummings model, the fully quantum counterpart of the Rabi model. Unlike the semiclassical approach, this leads to conclusions with no classical analog, such as the occurrence of Rabi oscillations even in the absence of photons; these are known as vacuum-field Rabi oscillations [11].

However, this result holds for a single-mode field, where the emission, reabsorption, and re-emission of a photon create a reversible spontaneous emission process. In contrast, as discussed in Section 1.1.1, we are dealing with multiple modes of the vacuum field.

1.1.3 Spontaneous and stimulated emission

Experimentally, it is observed that an excited atom undergoes a transition to a lower state and eventually reaches the ground state, but it does not oscillate back and forth indefinitely (as seen in Section 1.1.2). In physical reality, the single-mode field model is often insufficient, as in many cases, a continuum of modes must be considered, corresponding to a quantization cavity that extends infinitely. Hence spontaneous emission is a complex phenomenon and it is described by Weisskopf-Wigner theory[13] as an irreversible decay process.

The atom decays in a characteristic lifetime which, according to the uncertainty principle, limits the precision with which we can measure the energy. Specifically, the longest time during which energy measurements can be made is approximately the atomic lifetime τ , and hence the energy difference of the levels is uncertain by the amount [14]:

$$\Delta E = \frac{\hbar}{\tau} \tag{1.13}$$

This relation implies that the spontaneously emitted radiation is not perfectly monochromatic, but instead has a frequency spectrum with a width inversely proportional to τ .

For a multi-mode field, this produces a band of shifted frequencies, which, in the simple two-level atom case, follows a Lorentzian profile [14] in the emission spectrum of an atom.

Thus, even in the absence of interaction with an external light field, the atom still exhibits a non-zero linewidth, known as the natural linewidth. This linewidth is given by:

$$\Gamma = \frac{1}{\tau} \tag{1.14}$$

which is why the natural linewidth is also referred to as the decay width or decay rate. This linewidth, however, can be broadened by additional mechanisms such as the Doppler effect and power broadening, which will be discussed in Section 1.1.4.

A final consideration can be made regarding stimulated emission. All of these processes (absorption, stimulated emission, and spontaneous emission) were already studied by Einstein [15]. Revisiting his analysis, for a natural source such as the Sun, which can be approximated as a black body with a surface temperature of $T \approx 6000\,\mathrm{K}$, the ratio between spontaneous and stimulated emission's coefficients is approximately 400 for $\lambda = 400\,\mathrm{nm}$ and 30 for $\lambda = 700\,\mathrm{nm}$ [16]. Thus, at both ends of the visible spectrum, spontaneous emission dominates stimulated emission.

In the visible range, stimulated emission surpasses spontaneous emission only in "unnatural" sources, where a population inversion occurs) i.e., where more atoms are in the excited state than in the ground state. This is the case in lasers, where stimulated emission becomes the dominant process.

1.1.4 Bloch equation and total scattering rate

The spontaneous decay of the excited states, resulting from the interaction with the vacuum field, has so far been omitted, while only the purely oscillatory behavior of the atomic states has been considered. This phenomenon, however, is not straightforward to analyze. A common approach in quantum mechanics involves introducing the density matrix ρ , which allows the description of atomic excitation in terms of populations and coherences rather than state amplitudes [17]. Starting from the equation:

$$i\hbar \frac{d\rho}{dt} = \left[\rho, H_{tot}\right] \tag{1.15}$$

The damping terms due to spontaneous emission can be found after some considerations [12]:

$$\left(\frac{d\rho_{ee}}{dt}\right)_{sp} = -\left(\frac{d\rho_{gg}}{dt}\right)_{sp} = -\Gamma\rho_{ee} \tag{1.16}$$

describing the transition of the atom from $|e\rangle$ to $|g\rangle$ by spontaneous emission with rate Γ

$$\left(\frac{d\rho_{eg}}{dt}\right)_{eg} = -\frac{\Gamma}{2}\rho_{eg} \tag{1.17}$$

is the damping of optical coherences with a rate $\Gamma/2$. These are called the optical Bloch equations, where the steady-state solution for $w = \rho_{gg} - \rho_{ee}$ is [17]:

$$w = \frac{1}{1+s} {(1.18)}$$

with the saturation parameter s given by

$$s \equiv \frac{|\Omega|^2}{2|(\Gamma/2 - i\delta)|^2} = \frac{|\Omega|^2/2}{\delta^2 + \Gamma^2/4} = \frac{s_0}{1 + (2\delta/\Gamma)^2}$$
(1.19)

where the last step defines the on-resonance saturation parameter:

$$s_0 \equiv \frac{2|\Omega|^2}{\Gamma^2} = \frac{I}{I_c} \tag{1.20}$$

in terms of saturation intensity

$$I_s \equiv \frac{\pi h c}{3\lambda^3 \tau} \tag{1.21}$$

Moreover, for $s \ll 1$, the population is mostly in the ground state $(w \simeq 1)$ and ρ_{ee} reads:

$$\rho_{ee} = \frac{1}{2}(1 - w) = \frac{1}{2} \frac{s_0}{1 + s_0 + (2\delta/\Gamma)^2}$$
(1.22)

When $s \gg 1$ the population is equally distributed between the ground and excited state (w=0) then is $\rho_{ee}=1/2$. Now we discuss the total scattering rate [17]:

$$R_{sc} = \Gamma \rho_{ee} = \left[\frac{s_0}{1 + s_0} \right] \left[\frac{\Gamma/2}{1 + (2\delta/\Gamma')^2} \right]$$
 (1.23)

where $\Gamma' = \Gamma \sqrt{1+s_0}$ is called the power-broadened linewidth of the transition. From Fig. 1.3, it is clear that, at large s_0 , the excited state population is nearly half for $\delta = 0$ but decreases for $|\delta| \gg \gamma$.

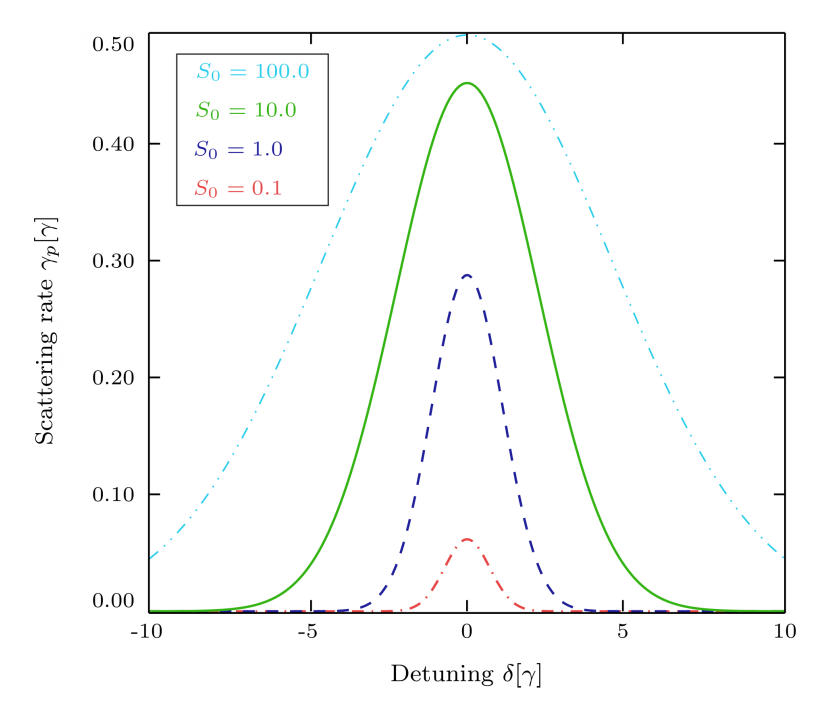


Figure 1.3. Excitation rate R_{sc} , in units of Γ , as a function of the detuning δ . Here R_{sc} and Γ are denoted as γ_p and γ , respectively. Credits: [17].

It is useful to note that other broadening mechanisms, such as the Doppler effect, have been left out of this discussion. In fact, considering the D_2 transition of ⁸⁷Rb at a temperature of $T = 1 \,\mathrm{mK}$, the Doppler broadening is estimated as:

$$\omega_D = \omega_0 \sqrt{\frac{2k_B T}{Mc^2}} \simeq 2\pi \times 560 \,\mathrm{kHz}$$
 (1.24)

with $\omega_0 = 2\pi \times 384\,\mathrm{THz}$ and $M = 1.41 \times 10^{-25}\,\mathrm{kg}$ [18]. This value is significantly smaller than the power-broadened linewidth, which is $\Gamma' \approx 2\pi \times 20\,\mathrm{MHz}$ for $s_0 = 10$ and still $\Gamma' \approx 2\pi \times 6.3\,\mathrm{MHz}$ even for a low intensity of $s_0 = 0.1$. Since $\Gamma' \gg \omega_D$ in both cases, Doppler

broadening is negligible compared to power broadening and can be safely ignored in this analysis.

1.2 Manipulating atoms with photons

The interaction between light and matter represents a cornerstone of atomic physics, influencing both the internal states and external motion of atoms. Light is not only a source of information about atomic structure but also a versatile tool for manipulating atomic behavior through carefully controlled interactions. Before examining these interactions in detail, it is essential to introduce two key physical processes that form their foundation: dissipative and reactive processes.

1.2.1 Dissipative and reactive processes

Consider a light beam with frequency ω_L propagating through a medium composed of atoms with a resonance frequency ω_A . Two principal processes can occur: the incident photons may be absorbed and subsequently scattered in all directions, while the propagation speed of light is altered. As a result of this interaction, atoms experience both dissipative and reactive effects. These effects manifest as a broadening and a shift of the atomic energy levels, respectively [19]. Hence:

- Dissipative (Absorptive) processes: These involve energy exchange between the atom and the radiation field, primarily due to photon absorption and spontaneous emission.
- Reactive (Dispersive) processes: These correspond to coherent interactions where the phase of the light field is modified without direct energy absorption by the atom.

It is possible to explain these two phenomena from a classical description of the interaction between light and atoms, introducing the refractive index of atomic vapors. This is a good approximation when there are weak atomic excitations and there are many photons since the field can be treated as a set of harmonic oscillators. The atom can be described by [20]:

$$m\ddot{x}^{(+)} + m\Gamma\dot{x}^{(+)} + m\omega_A^2 x^{(+)} = -e\varepsilon E_0^{(+)} e^{-i\omega_L t}$$
 (1.25)

Where the first term is the inertial force, the second is the damping force describing the loss of energy due to radiation emission, the third term is the restoring force (electron oscillating on an external electrical field) and finally in the right-hand side there is the external driving force. Here x represents the average position of the electron, since, quantum mechanically, the electron is not localized, and ω_A is the resonant frequency of the harmonic potential. From few calculations [20] the phase index and absorption coefficient can be derived, which are the real and imaginary part of refractive index(\tilde{n}) respectively:

$$n(\omega_L) := \operatorname{Re}[\tilde{n}(\omega_L)] = n(\omega_L) \approx 1 + \frac{Ne^2}{2m\varepsilon_0} \frac{(\omega_A - \omega_L)/2\omega_L}{(\omega_A - \omega_L)^2 + (\Gamma/2)^2}$$
(1.26)

$$a(\omega_L) := 2k_0 \operatorname{Im}[\tilde{n}(\omega_L)] = a(\omega_L) \approx \frac{Ne^2}{m\varepsilon_0 c\Gamma} \frac{(\Gamma/2)^2}{(\omega_A - \omega_L)^2 + (\Gamma/2)^2}$$
(1.27)

The **dissipative process**, related to the **imaginary part** of the refractive index, $\text{Im}(\tilde{n})$, is responsible for photon absorption [19]. The variation of $\text{Im}(\tilde{n})$ with the detuning:

$$\delta = \omega_L - \omega_A$$

follows a Lorentzian curve, indicating the resonance behavior of the atomic transition, or that the corresponding attenuation of the light beam is maximum at resonance. Physically, this process leads to the broadening of atomic energy levels, which is quantified by the natural linewidth Γ . This broadening, as previously mentioned, corresponds to spontaneous emission and defines the timescale for atomic relaxation.

The **reactive process** is related to **real part** of the refractive index, $\operatorname{Re}(n)$. As light propagates through an atomic ensemble, the phase velocity of light is altered due to the refractive index. The dispersion follows a Lorentzian curve, where the change in refractive index relative to vacuum, n-1, depends on detuning δ . The real and imaginary part of $n(\omega)$ are shown in Fig. 1.4.

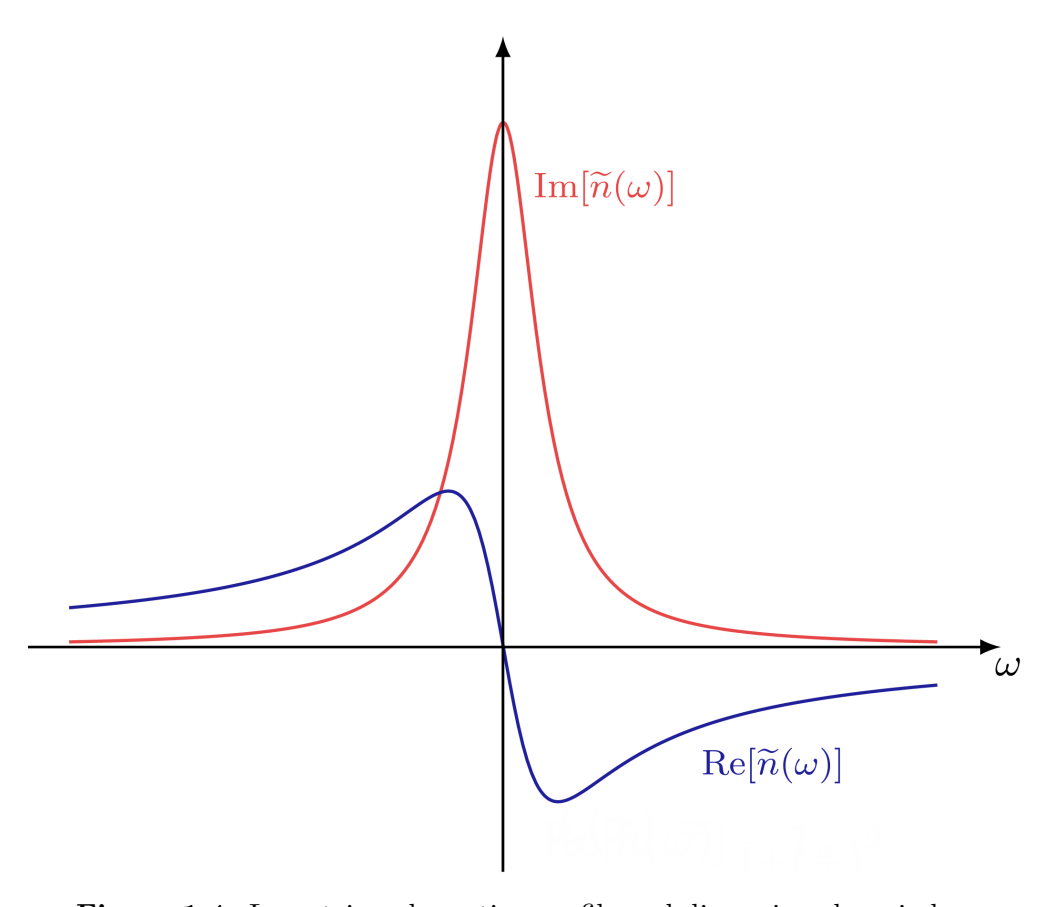


Figure 1.4. Lorentzian absorption profile and dispersive phase index.

1.2.2 Manipulation of internal and external degrees of freedom

An atom possesses multiple degrees of freedom, categorized into internal and external degrees of freedom [19]. Internal degrees of freedom include electronic configuration, which describes the energy levels occupied by electrons, and spin polarization, related to the orientation of electron and nuclear spins. Their manipulation is achieved through optical pumping. External degrees of freedom describe the motion and spatial orientation of the atom, particularly its center-of-mass motion. Manipulating these degrees of freedom relies on two primary forces: dissipative forces and reactive (dispersive) forces.

Manipulation of internal degrees of freedom

The internal degrees of freedom of an atom can be manipulated using light in two key ways:

- Optical pumping: This technique relies on resonant excitation of atoms by circularly polarized light to transfer angular momentum from photons to atoms. By selectively driving transitions between specific atomic sublevels and it is used for different objectives e.g. populate specific Zeeman or hyperfine sublevels.
- Light shifts (AC Stark shift): This process occurs due to the interaction between an atom and an off-resonant laser field, which induces a shift in the atomic energy levels. The resulting energy shift at high detuning depends on the light intensity and detuning:

$$\Delta E \propto \frac{I}{\delta}$$
 (1.28)

where I is the laser intensity and $\delta = \omega_L - \omega_A$ is the detuning. Light shifts allows the creation of optical potentials in optical lattices and dipole traps.

Manipulation of external degrees of freedom

To manipulate an atom's center-of-mass motion, two fundamental types of radiative forces can be employed, which originate from light-matter interactions:

• Dissipative forces (radiation pressure force): These forces arise from the exchange of linear momentum between an incident photon and the atom during a resonant scattering process. Each absorbed photon transfers momentum $\hbar k$, and spontaneous emission occurs in a random direction, leading to a force given by (details in Section 1.3.2):

$$F_{\rm rad} = \frac{\hbar k \Gamma}{2} \frac{s_0}{1 + s_0 + (2\delta/\Gamma)^2},$$
 (1.29)

where Γ is the natural linewidth, s_0 is the saturation parameter, and δ is the detuning. This force enables Doppler cooling and the mechanism behind the Magneto-Optical trap.

• **Dispersive forces (dipole force)**: Unlike radiation pressure, the dipole force is a conservative force that arises from spatially varying light intensities.

The dipole potential of an oscillating field $\vec{E} = \vec{E}_0 \cos(\omega_L t)$ interacting with a two-level atom reads [21]:

$$\hat{U}_{dip} = -\frac{1}{2} \langle \hat{\vec{d}} \cdot \vec{E} \rangle \tag{1.30}$$

where $\hat{\vec{d}}$ is the atomic dipole moment induced by the oscillating field. Since $\hat{\vec{d}} \propto \vec{E}$, and based on certain considerations [22]:

$$\hat{U}_{dip} \propto \frac{I \,\Gamma}{\delta} \tag{1.31}$$

where I is the beam intensity.

Given the upcoming discussion on laser cooling and magneto-optical traps, it is useful to clarify that the focus will be primarily on radiation pressure and optical pumping, while excluding the treatment of light shift and dipole forces. This focus is justified by the condition $\delta/\Gamma \ll 1$ and intensity beam $I \gg 1 \,\mathrm{W/m^2}$, under which radiation pressure becomes the dominant effect. Additionally, although there is a coupling between internal and external variables, the adiabatic approximation allows for the elimination of the fast internal variables, as discussed in [12, 20], a process that will be analyzed in the following sections.

1.2.3 Characteristic times

Recalling the system in Fig. 1.1, the characteristic times are examined to integrate previously separate notions into a unified understanding of its dynamics. This discussion follows [12]. The shortest characteristic time in this context is the correlation time τ_c of the **vacuum field**. Vacuum fluctuations exhibit a broad frequency spectrum $J(\omega)$, which varies only slightly around the atomic resonance frequency ω_A . The vacuum correlation time is approximately [12]:

$$\tau_c \simeq \frac{1}{\omega_A} \tag{1.32}$$

Moving to the **internal degrees of freedom**, the most prominent characteristic time is the radiative lifetime τ_R of the excited state e:

$$\tau_R = \frac{1}{\Gamma}$$

where Γ is the natural linewidth of the excited state, directly related to the spontaneous emission rate. The relation $\Gamma \ll \omega_A$ implies:

$$\tau_R \gg \tau_c$$

In atoms with multiple Zeeman sublevels, additional internal timescales emerge due to optical pumping. Absorption followed by spontaneous emission can redistribute the atomic population among different Zeeman sublevels. The characteristic timescale for these cycles is given by the optical pumping time τ_P :

$$au_P = rac{1}{\Gamma'}$$

where Γ' is the optical pumping rate, which depends linearly on the laser intensity I_L . At low intensities:

$$\tau_P \gg \tau_R$$

In multi-level atoms, this optical pumping time plays a crucial role. In contrast, for simple two-level atoms, the primary relaxation mechanism remains spontaneous emission, and the internal dynamics can be fully characterized by τ_R .

Turning to the **external degrees of freedom**, an important characteristic time is the velocity damping time, which describes how quickly the atom's translational motion is affected by photon recoil. This timescale is:

$$T_{\rm ext} = \frac{\hbar}{E_R}$$

where

$$E_R = \frac{\hbar^2 k_L^2}{2M}$$

is the recoil energy imparted to the atom when it absorbs or emits a single photon. Here, $k_L = \omega_L/c$ is the wavevector of the light field.

For most optical transitions used in atomic manipulation:

$$\hbar\Gamma \gg E_R$$

which implies:

$$T_{\rm ext} \gg T_{\rm int}$$

This clear separation of timescales greatly simplifies the description of atomic motion. In particular, the fast internal dynamics can be adiabatically eliminated, leaving a reduced set of equations that describe the atomic motion alone [12, 20].

1.3 Magneto-Optical trap

Having established the fundamental physical processes involved, this section will focus on the principles behind atomic cooling and trapping. The discussion will follow a semiclassical approach, leaving out the complexities of the full quantum treatment while highlighting the key mechanisms that enable these techniques.

1.3.1 Transfer of momentum

Building on the behavior of a two-level atom interacting with a light field, the focus now shifts to the fundamental instruments required to implement a magneto-optical trap. In this framework, the atom is once again modeled as a two-level system irradiated by a resonant photon beam. As previously discussed, this interaction results in a continuous cycle of absorption and emission.

The absorption of a single photon, due to the momentum conservation alters the velocity of the atom by recoil velocity $v_{rec} = \hbar k/M \simeq 0.6 \,\mathrm{cm/s}$ for Rb. The spontaneous emission follows the absorption with a natural lifetime $\tau = 1/\Gamma$ of the excited state, where, again, Γ is its decay rate (or width).

Since the spontaneous emission is isotropic, the recoil of the atom associated with this process is in a random direction, thus there is no net change of momentum on average.

Hence, after N absorption-spontaneous emission cycles, the momentum transfer is [21]:

$$\Delta \vec{p}_N = N\hbar \vec{k}_L + \hbar \sum_{i=0}^{N} \vec{k}_{i,sp}$$
(1.33)

with $\vec{k}_{i,sp}$ being the wavevector associated with the spontaneously emitted photon in the i^{th} cycle and as it has been said before, $\sum_{i=0}^{N} \vec{k}_{i,sp} \simeq 0$ due its isotropic nature. Noticing that, if the laser intensity is high, stimulated emission plays a crucial role, resulting in the emission of photons in the same direction as the laser beam. However, cycles of absorption and stimulated emission don't change the momentum \vec{p} . In Fig. 1.5 is shown the whole process.

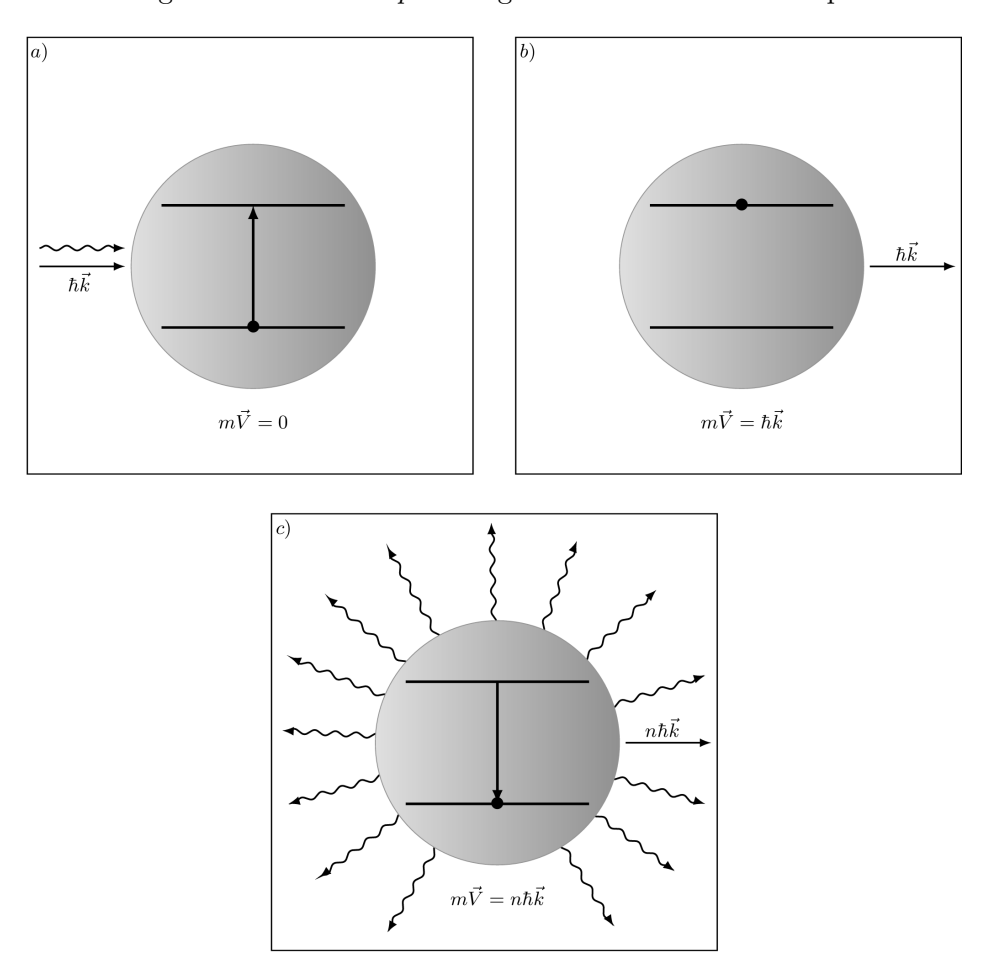


Figure 1.5. A simplified depiction of the light pressure acting on the two-level atom. Photon absorption a) and its consequent exchange of momentum b) and emission in c). Credits: [23].

Since there is a momentum variation, there is also a force applied on the atom $\vec{F} = d\vec{p}/dt$ directed along the laser beam itself. The force can be calculated:

$$\vec{F} = M \cdot \vec{a} = \hbar \vec{k}_L \frac{\Delta N}{\Delta t} = \hbar \vec{k}_L R_{sc} = \hbar \vec{k}_L \Gamma \rho_{ee}$$
 (1.34)

where ΔN is the number of photon absorbed and $R_{sc} = \Gamma \rho_{ee}$ is the absorption rate or photon scattering rate as already seen. \vec{F} has the same dependence of ρ_{ee} on $\delta = \omega_L - \omega_A$ detuning Eq. (1.22), hence plotting \vec{F} as function of δ it varies as a Lorentzian absorption curve centered about $\delta = 0$, as expected for a dissipative process.

1.3.2 Doppler cooling and optical molasses

In the reference frame of an atom moving with velocity \vec{v} , the frequency ω_L of a laser beam with wavevector \vec{k} is Doppler shifted to:

$$\omega' = \omega_L - \vec{k} \cdot \vec{v} \tag{1.35}$$

When ω_L is tuned below the atomic resonance frequency ω_A ($\omega_L < \omega_A$), ω' gets closer to resonance if the atom moves against the laser beam $(\vec{k} \cdot \vec{v} < 0)$; conversely, if the atom moves along the direction of the laser beam $(\vec{k} \cdot \vec{v} > 0)$, the detuning increases, shifting the atom further from resonance. As a result, atoms moving opposite to the laser direction experience stronger interactions, forming the basis of Doppler cooling.

This occurs because they perceive the laser beam at a frequency closer to resonance, allowing them to absorb photons. Since the momentum exchange follows the direction of the beam's propagation, the atoms are gradually slowed down.

In optical molasses (OM), red-detuned lasers are typically used to create a viscous medium where atoms experience a resistive force. In a one-dimensional model (as shown in Fig. 1.6), the laser frequency in the atom's reference frame is given by $\omega'_L = \omega_L \pm k_L v$, where the sign depends on the direction of the atom's motion relative to the beam.



Figure 1.6. Moving atom in the laboratory reference frame.

Now let's consider two counter-propagating beams weak enough so that their effects taken separately are additive (namely $s_0 \ll 1$). Then the total light pressure force :

$$F_{OM} = F_{+} + F_{-} \tag{1.36}$$

where F_{+} is the force applied on the atom from the left laser beam and F_{-} is the force applied on the atom from the right laser beam:

$$\begin{cases}
F_{+} = \hbar k_{L} \Gamma \rho_{ee} = \hbar k_{L} \Gamma \frac{s_{0}}{1 + s_{0} + (2(\delta - |k_{L}|v)/\Gamma)^{2}} \\
F_{-} = -\hbar k_{L} \Gamma \rho_{ee} = -\hbar k_{L} \Gamma \frac{s_{0}}{1 + s_{0} + (2(\delta + |k_{L}|v)/\Gamma)^{2}}
\end{cases} (1.37)$$

where the total force described in Eq. (1.36) is represented in Fig. 1.7.

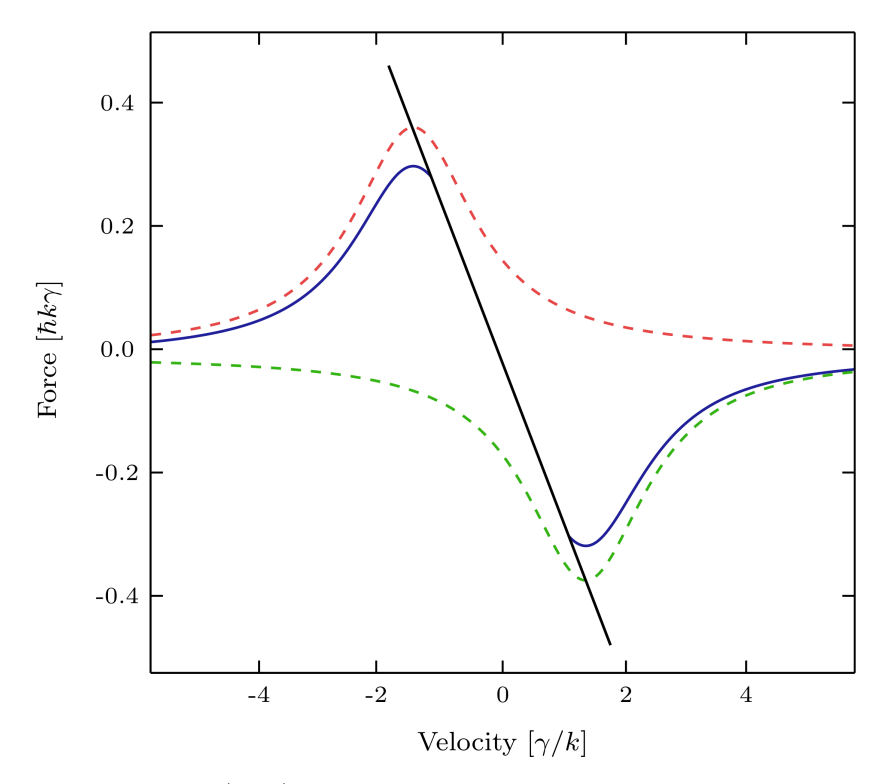


Figure 1.7. \vec{F}_+ , \vec{F}_- and F_{OM} are shown in red, green and blue trace respectively (they are calculated for detuning $\delta = -1.3\Gamma$ and saturation $s_0 = 3$. Here the absorption rate is γ . Credits: [23].

Assuming that atoms are slow, the force can be approximated in:

$$F_{OM} \simeq \frac{8\hbar k^2 \delta s_0 v}{\Gamma[1 + s_0 + (2\delta/\Gamma)^2]^2} = -\alpha(\delta)v$$
(1.38)

where α is the damping constant, positive for $\delta < 0$. For slow atoms F_{OM} is proportional to the velocity and it resembles the viscous damping. By using three intersecting orthogonal pairs of counter-propagating laser beams, the above elucidated slowing effect can be extended to 3D

$$\vec{F}_{OM} \simeq -\alpha(\delta)\vec{v} \tag{1.39}$$

Cooling is possible only for negative values of δ , in the opposite case heating occurs and the atom gains energy. It should be noted that the resonance radiation pressure force of the type in Eq. (1.36) alone is not able to provide stable trapping of atoms.

1.3.3 Doppler cooling limit

Laser cooling has been introduced in which atoms are slowed down through interactions with resonant photons, exploiting the momentum exchange that occurs during absorption and spontaneous emission processes. When an atom absorbs a photon, it experiences a recoil in the direction of the incoming photon, while spontaneous emission, being isotropic, introduces a random recoil.

It could seem that in the end the initially moving atoms will decelerate rapidily to zero velocity but this is not possible due to intrinsic limitations: the interplay between these processes results in a nonzero equilibrium velocity, which can be understood as a random walk in momentum space with steps of size $\hbar k$ (in Fig. 1.8). The temperature of the atomic ensemble arises from the balance between two competing effects:

- Cooling, induced by the radiation pressure force, which is obtained through an ensemble average and leads to a reduction in the atomic velocity.
- **Heating**, caused by fluctuations in the cooling force, which result in an increase in atomic energy.

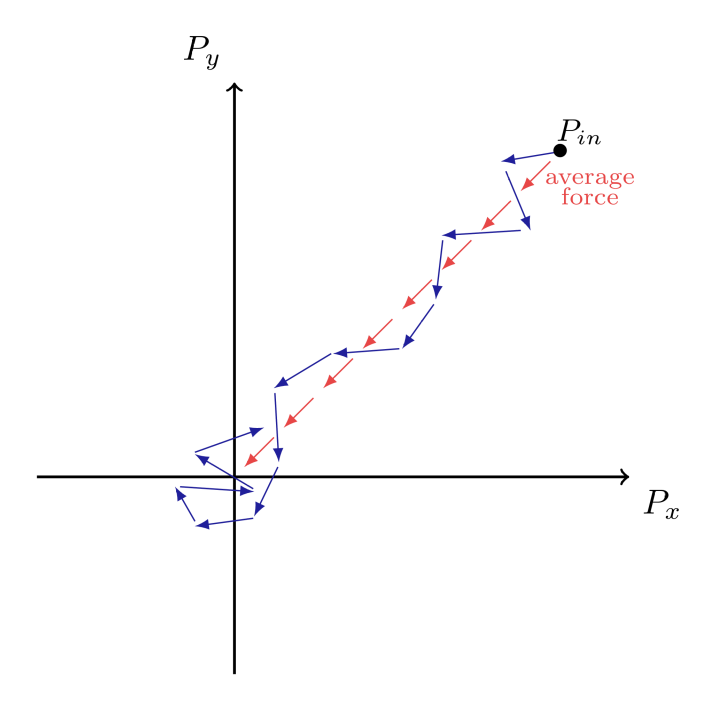


Figure 1.8. Representation of the random walk of atomic momentum due to photon recoil during absorption and spontaneous emission. The blue trajectory illustrates the stochastic diffusion process, while the red arrows indicate the average force that drives the atom's motion.

The cooling process can be analyzed starting from the velocity distribution's variance [20]:

$$\frac{d}{dt}\langle v^2 \rangle = 2 \left\langle \vec{v} \cdot \frac{d\vec{v}}{dt} \right\rangle = \frac{2}{M} \left\langle \vec{v} \cdot \frac{d\vec{p}}{dt} \right\rangle = \frac{2}{M} \langle \vec{v} \cdot \vec{F}_{OM} \rangle \tag{1.40}$$

where M is the atomic mass, and the angle brackets denote an ensemble average.

Recalling Eq. (1.38) in the low-velocity regime, the equation of motion can be rewritten as:

$$\frac{d}{dt} \langle v^2 \rangle \Big|_{cooling} = \frac{16\hbar k^2 \delta}{M \Gamma} \cdot \frac{s_0}{\left[1 + s_0 + \left(\frac{2\delta}{\Gamma}\right)^2\right]^2} \cdot \langle v^2 \rangle \tag{1.41}$$

Therefore, from this equation, we see that the velocity decreases to zero for $\delta < 0$.

For the heating process, a more rigorous treatment can be performed using quantum mechanics to account for fluctuations [20]. However, here we limit ourselves to an heuristic approach. During the scattering of a photon from one of the laser beams, an absorption event occurs, followed by an emission event. Each absorption event imparts a momentum "kick" of magnitude $\hbar k$ in a well-defined direction, while the subsequent emission occurs in a random direction, leading to a second momentum kick of the same magnitude.

Thus, each scattering event effectively corresponds to two steps in a random walk in velocity space, where the step size is $\hbar k/M$. To further justify this, let us focus on the atomic momentum changes occurring in each cycle (j = 1, ..., N cycles):

$$\vec{p}_j = \hbar \vec{q}_j - \hbar \vec{k}_j \tag{1.42}$$

where \vec{q}_j is the wavevector corresponding to one of the six laser beams, and \vec{k}_j is the wavevector of the spontaneously emitted photon. The total momentum change is given by:

$$\vec{p}_{tot} = \sum_{j=1}^{N} \vec{p}_j = 0 \tag{1.43}$$

Now, considering the variance:

$$\langle \vec{p}_{tot}^2 \rangle = \hbar^2 \sum_{ij} \left\langle \left(\vec{q}_i - \vec{k}_i \right) \cdot \left(\vec{q}_j - \vec{k}_j \right) \right\rangle = \hbar^2 \sum_{ij} \left(\vec{q}_i^2 \delta_{ij} + \vec{k}_i^2 \delta_{ij} \right) = 2\hbar^2 \vec{k}^2 N \tag{1.44}$$

which, since $dN/dt = R_{sc}$ leads to:

$$\frac{d}{dt}\langle \vec{v}^2 \rangle \bigg|_{heating} = \frac{d}{dt} \left\langle \frac{\vec{p}_{tot}^2}{M^2} \right\rangle = 2 \left(\frac{\hbar k}{M} \right)^2 R_{sc}$$
(1.45)

Summing Eq. (1.41) and Eq. (1.45), we obtain:

$$\frac{d}{dt} \langle \vec{v}^2 \rangle = \frac{d}{dt} \langle \vec{v}^2 \rangle \Big|_{heating} + \frac{d}{dt} \langle \vec{v}^2 \rangle \Big|_{cooling}$$

$$= 2 \left(\frac{\hbar k}{M} \right)^2 \cdot 6 \frac{\Gamma}{2} \frac{s_0}{\left[1 + s_0 + \left(\frac{2\delta}{\Gamma} \right)^2 \right]^2} + \frac{16\hbar k^2 \delta}{M\Gamma} \cdot \frac{s_0}{\left[1 + s_0 + \left(\frac{2\delta}{\Gamma} \right)^2 \right]^2} \cdot \langle v^2 \rangle \tag{1.46}$$

where we have taken into account that, in the MOT, there are 6 beams, hence R_{sc} is six times larger than for a single beam.

From above, at low intensity $s \ll 1$, the steady-state solution is:

$$\langle v^2 \rangle = -\frac{3}{8} \frac{\hbar \Gamma^2}{M \delta} \cdot \left[1 + \left(\frac{2\delta}{\Gamma} \right)^2 \right]$$
 (1.47)

This is an expression for the equilibrium kinetic energy, which we can convert to a temperature

$$\frac{1}{2}M\langle v^2\rangle = \frac{3}{2}k_BT\tag{1.48}$$

The temperature is minimized for the detuning $\delta = -\Gamma/2$, giving the Doppler temperature:

$$k_B T = \frac{\hbar \Gamma}{2} \tag{1.49}$$

Hence, laser cooling in optical molasses reaches an equilibrium temperature determined by the balance between photon recoil heating and velocity-dependent cooling forces. For example taking into account a rubidium atom, this limit is found to be:

$$T_D = \frac{\hbar\Gamma}{2k_B} \simeq 140 \ \mu K \tag{1.50}$$

with $\Gamma \simeq 2\pi \times 6$ MHz. It has been demonstrated that considering a multilevel atomic structure leads to significantly stronger cooling forces for slow atoms. This effect explains the observation of atoms cooled in optical molasses to temperatures an order of magnitude below the Doppler limit [24], a phenomenon not predicted by the simplified two-level atom model, where the role of polarization gradients is neglected.

1.3.4 1D model of the MOT

To trap atoms, it is necessary not only to cool them but also to confine them using a position-dependent force. This confinement is achieved by applying a magnetic field. For simplicity, let us consider a 1D model of the Magneto-Optical Trap (MOT). The setup consists of two counter-propagating laser beams along the z-axis with opposite circular polarizations, denoted as σ^+ and σ^- . Additionally, the system includes a coaxial, inhomogeneous magnetic field \vec{B} with a quadrupole symmetry.

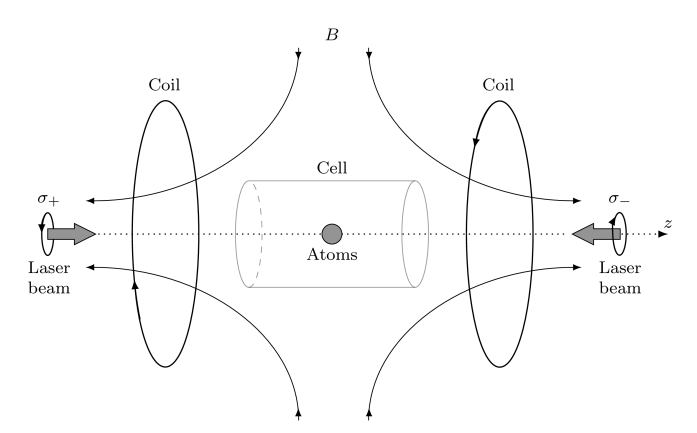


Figure 1.9. Schematic 1D MOT configuration, with two counterpropagating beams and a magnetic field of quadrupole symmetry.

The analysis proceeds as follows: first, the hyperfine structure is introduced, followed by the effect of the magnetic field, and finally, a discussion of the resulting behavior.

Real Atoms and Hyperfine Structure

The hyperfine structure results from the interaction between the electronic angular momentum \vec{J} and the nuclear angular momentum \vec{I} . The corresponding Hamiltonian is:

$$\hat{H}_{HF} = A\vec{I} \cdot \vec{J} \tag{1.51}$$

Here, A is the hyperfine coupling constant. Defining the total angular momentum as:

$$\vec{F} = \vec{I} + \vec{J}$$

the interaction can be expressed as:

$$\vec{I} \cdot \vec{J} = \frac{1}{2} \left[\vec{F}^2 - \vec{J}^2 - \vec{I}^2 \right] \tag{1.52}$$

The hyperfine Hamiltonian is diagonal in the $|F, F_z\rangle$ basis:

$$\langle F, F_z | H_{HF} | F', F_z' \rangle = \delta_{FF'} \delta_{F_z F_z'} A_{\frac{1}{2}}^{\frac{1}{2}} [F(F+1) - J(J+1) - I(I+1)]$$
 (1.53)

When a small magnetic field is applied, we choose the z-axis along the \vec{B} field and the degeneracy over F_z is lifted due to the Zeeman effect, whose shifts are $\propto B$. In particular:

$$\hat{H}_{tot} = \hat{H}_0 + \hat{H}_z \tag{1.54}$$

where the interaction is represented by $\hat{H}_z = -\vec{\mu} \cdot \vec{B}$, where $\vec{\mu}$ is the magnetic moment of the atom. Using perturbation theory at first order, the Zeeman shift of the sublevel is proportional to its magnetic quantum number m_F or $\langle F_z \rangle$ and to the B field:

$$\Delta E(F, F_z) = \langle F, F_z | H_z | F, F_z \rangle = g_F \mu_B B_z \langle F_z \rangle \tag{1.55}$$

Where g_F is the Landé factor that is given by :

$$g_F = g_J \frac{1}{2} \left[\frac{F(F+1) + J(J+1) - I(I+1)}{F(F+1)} \right], \tag{1.56}$$

which can be derived using the Wigner-Eckart theorem [20]. The factor g_J in the equation for g_F is the Landé factor associated with the total electronic angular momentum J, given by:

$$g_J = \frac{3}{2} + \frac{S(S+1) - L(L+1)}{2J(J+1)}. (1.57)$$

For our purposes, we consider the hyperfine structure of the ground state of 87 Rb, characterized by the quantum numbers L=0, S=1/2, J=1/2, and I=3/2. This results in two possible total angular momentum states:

$$F = |I - J|, \dots, |I + J| = 1, 2.$$
 (1.58)

Thus, the ground state of ⁸⁷Rb exhibits two hyperfine levels.

When a small magnetic field is applied, the Wigner-Eckart theorem allows us to determine the Landé factors for these levels, yielding $g_{F=2} = \frac{1}{2}$ and $g_{F=1} = -\frac{1}{2}$, which leads to the splitting of the hyperfine states in Fig. 1.10.All hyperfine splittings for ⁸⁷Rb and ⁸⁵Rb D_2 transitions can be found in Appendix A.5.

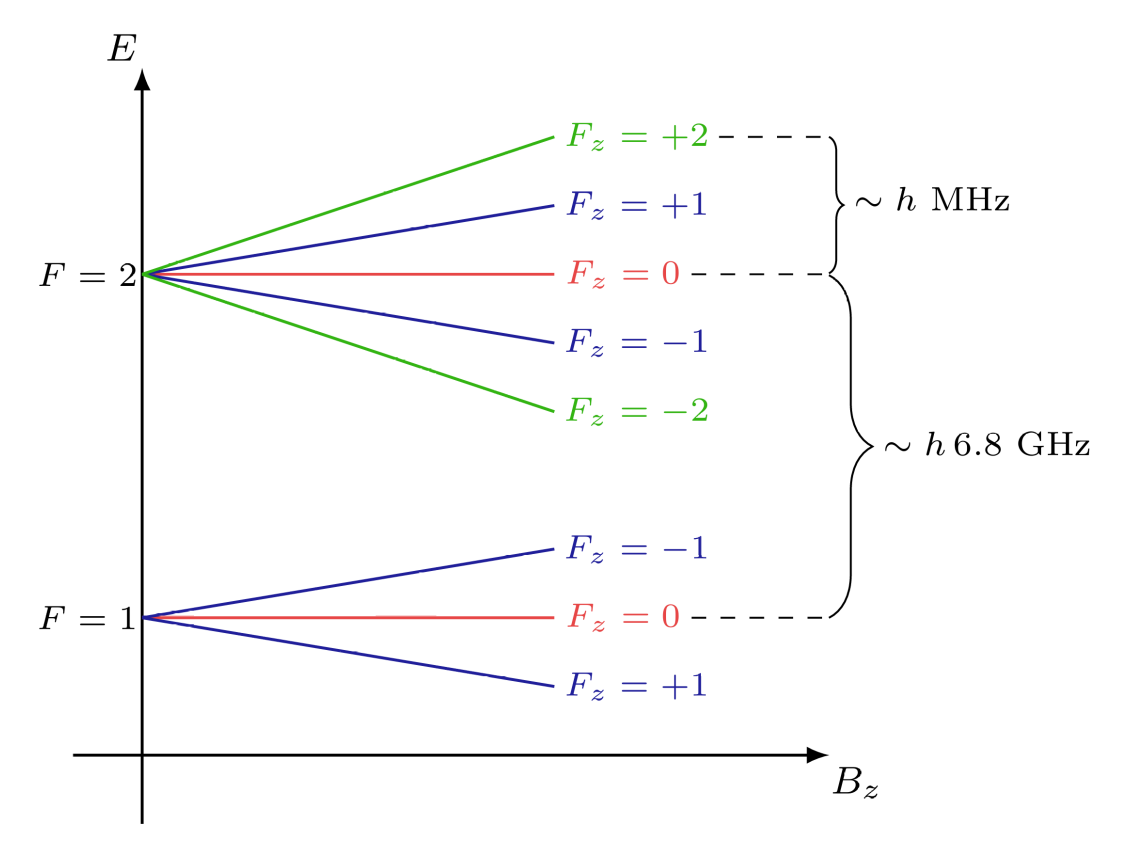


Figure 1.10. The Zeeman splitting of hyperfine energy levels occurs in the presence of a magnetic field B_z . The energy levels, identified by the quantum numbers F and F_z , shift proportionally to the applied field due to the Zeeman effect. For a magnetic field of approximately $B \sim 1$ G, the resulting splitting between magnetic sublevels is on the order of MHz, while the hyperfine structure itself lies on the order of GHz.

Hyperfine structure and selective absorption of the circularly polarized light

The selection rules dictate which transitions are excited by the counter-propagating beams (Fig. 1.11):

$$\begin{cases} \sigma^+ \to \Delta m_F = 1\\ \sigma^- \to \Delta m_F = -1 \end{cases} \tag{1.59}$$

where the electric field of the circularly polarized light can be written as:

$$\vec{E} = E_0 \left(\frac{\hat{x} \pm i\hat{y}}{\sqrt{2}} \right) e^{-i\omega_L t} + c.c.$$

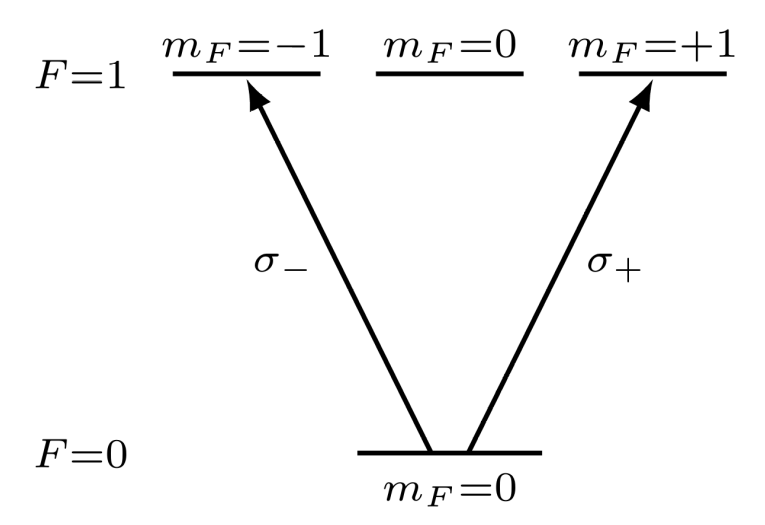


Figure 1.11. Selective absorption of the circularly polarized light.

Applying an inhomogeneous magnetic field

A magnetic field with a constant gradient $\partial_z B$ is applied along the z-axis, resulting in a position-dependent energy shift of the atomic sublevels. As an atom moves away from the trap center, these shifts bring it closer to resonance with the laser beam that exerts a restoring force directed toward the trap center.

To illustrate this, consider an atom at rest positioned to the left of the reference frame (see Fig. 1.12). In this region, the magnetic field B is negative. The beam traveling from the left toward the trap center is σ^+ -polarized. Due to the red detuning of the lasers relative to the zero-field atomic resonance, the transitions from F = 0 to F' = 1 are predominantly driven by the σ^+ light, resulting in a momentum transfer that pushes the atom toward the center.

Meanwhile, the counter-propagating σ^- -polarized beam is shifted further out of resonance due to Zeeman effect. Consequently, the momentum transfer from this beam, which would push the atom away from the trap center, is significantly weaker. As a result, the atom experiences a net force directing it toward the B=0 region.

On the right side of the trap, the situation is reversed. In this region, the σ^- beam becomes more resonant, while the σ^+ beam is shifted out of resonance. The atom again receives a net force directing it back toward the center.

Thus, the combined effect of the two laser beams and the position-dependent magnetic field ensures that atoms are always pushed toward the trap center, where the total force vanishes.

Allowing for the B field in an OM Eq. (1.36) modifies it. It assumes the form [23]:

$$F_z = \pm \frac{\hbar k \Gamma}{2} \frac{s_0}{1 + s_0 + [2(\delta \mp |k_L|v \mp \mu'B/\hbar)/\Gamma]^2},$$
(1.60)

where $\mu' = (g_e m_e - g_g m_g) \mu_B$ the effective magnetic moment for the cooling transition, g_g (e.g. g_e) Lande factor of the excited (ground) state, m_e (m_g) magnetic number of the excited (ground) state, $|\omega_D| = |k_L|v$ the Doppler shift: $|\omega_z| = \mu' B/\hbar$ in the Zeeman shift.

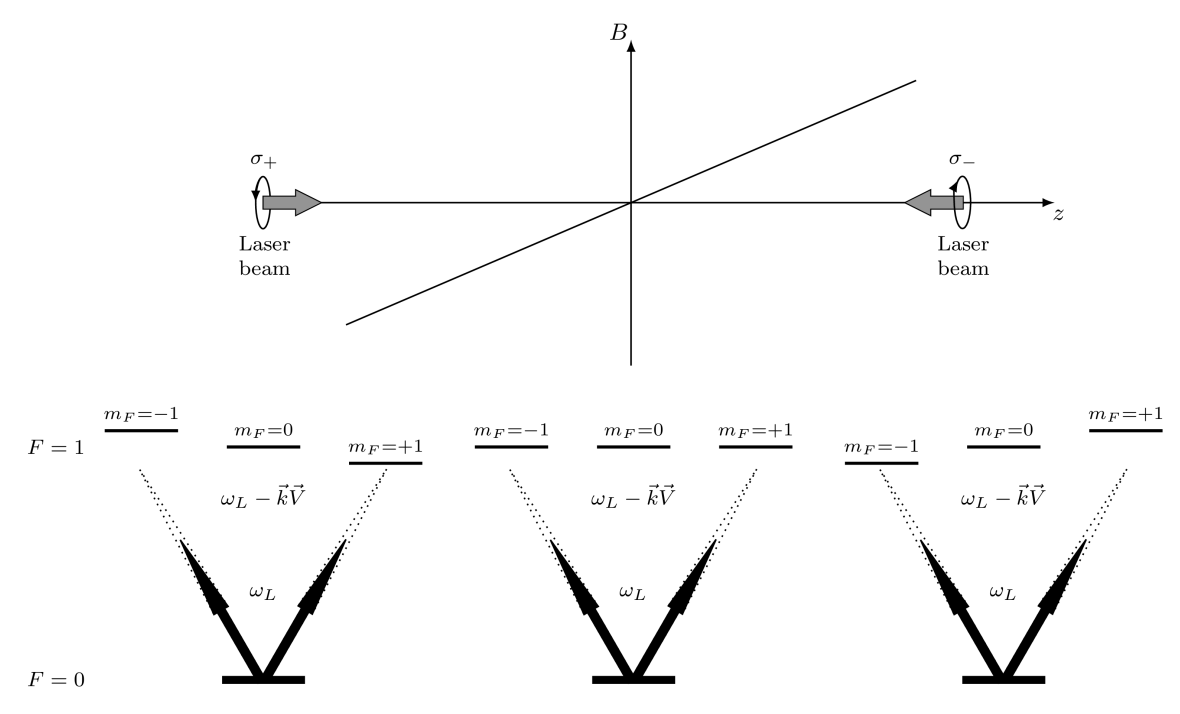


Figure 1.12. Schematic representation of the Zeeman shift for a simple atomic structure with F = 0 and F' = 1 in a one-dimensional MOT. The magnetic field gradient $\partial_z B$ causes a splitting of the magnetic sublevels, with σ^+ and σ^- polarized laser beams interacting differently with the atoms depending on their position along the z-axis. The solid arrows indicate the laser frequencies, red-detuned from resonance, while the dotted arrows represent the Doppler-shifted frequencies experienced by the moving atoms. Credits: [23]

Assuming that both $|\omega_z|$ and $|\omega_D|$ are small as compared to δ :

$$F_z \approx -\alpha v - \xi z. \tag{1.61}$$

where can be found [23]:

$$\xi = \frac{\partial B}{\partial z} \frac{\mu' \alpha}{\hbar k} \tag{1.62}$$

The 3D generalization of the 1D model is rather natural. There are three pairs of counter-propagating beams and a quadrupole magnetic field that follows the anti-Helmholtz configuration. In a real MOT, a field gradient $\partial_z B$ of the order of 10 to 20 G/cm is typically used along the axial direction. Due to the condition $\nabla \cdot \mathbf{B} = 0$, the radial gradient must be half of the axial one, i.e., $\partial_r B = \frac{1}{2} \partial_z B$.

Materials and methods

In order to reproduce the MOT described in the previous Chapter 1 it has been employed for this experiment rubidium 87 atoms (⁸⁷Rb), which is the workhorse of atom cooling. In this chapter we're going to introduce the experimental setup and the methodology used to trap and study the Rb atoms behavior. It is important to mention that the aim of this experiment is to transport the rubidium atoms in the hollow core fiber through the implementation of a dipole trap.

2.1 General description

In order to achieve a stable Magneto-Optical Trap (MOT), the entire experimental setup requires a vacuum chamber under Ultra-High Vacuum (UHV) conditions, a quadrupole magnetic field, a laser control system, and an imaging system. The apparatus is fully fiber-coupled using standard solid-core fibers, ensuring no light propagates in free space except for the MOT beams near the vacuum chamber. This design makes the setup far more stable against temperature fluctuations and eliminates the need for periodic realignment, thus making it significantly more user-friendly compared to traditional systems. Moreover, because there is no stray light, the risk of health hazards to operators is greatly reduced.

The use of widespread, telecom-grade, and highly reliable components ensures easy replacement, repair, and upgrades when needed. Furthermore, all fibers used in this experiment are polarization-maintaining (PM) to preserve and control the light polarization.

Since wavelength stability and precision are critical for MOT operation, the Cooler and Repumper lasers are frequency-locked to a Master laser, which is itself locked to a hyperfine transition of rubidium (Rb). Notably, the Master laser setup is the only free-space optical system in the experiment.

2.2 Vacuum chamber

The vacuum chamber is essential in this experiment as it provides the environment to host the Rb atom cloud. The vacuum chamber is positioned at the center of an optical breadboard and consists of various components attached to different subsystems: optical components for lasers, a pair of magnetic coils, three pairs of compensating coils, and an HCPCF port.

The chamber is supported by a clamping structure designed to provide mechanical stability, ensuring structural integrity and secure attachment to the optical breadboard. This structure also helps minimize mechanical vibrations, thereby improving the reproducibility of the experiments and protecting the system from accidental impacts.

The chamber contains the fundamental components required for the MOT construction, namely laser beams and magnetic coils. To create a 3D MOT, three pairs of laser beams are employed.

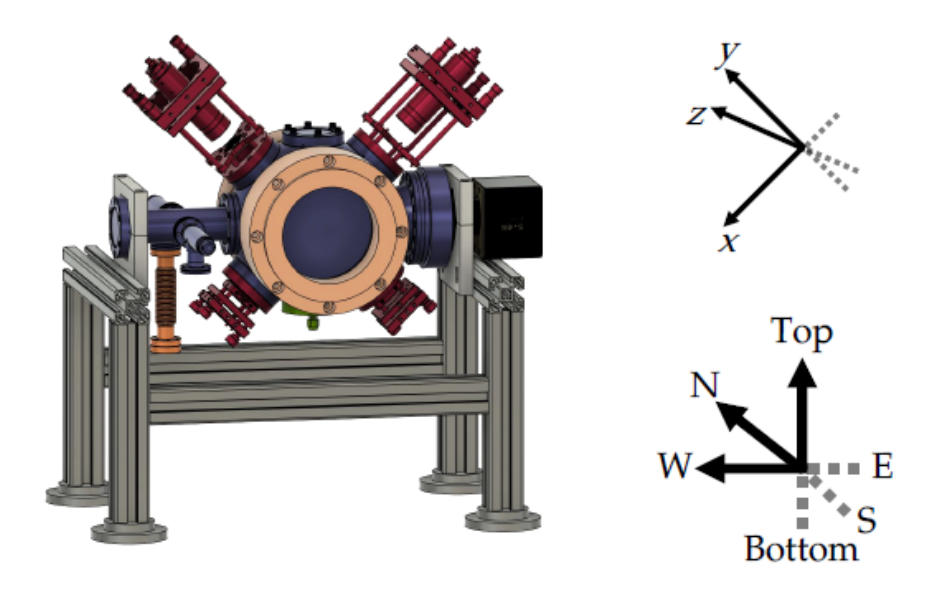


Figure 2.1. The vacuum chamber setup with all its components: the vacuum chamber is painted purple, the MOT optical system in red, the MOT coils in orange, the ionic pump in black, the Rb source on the left side in dark orange, and the HCPCF port in green, located behind the coils. Finally, on the west side, there is a glass viewport for the CMOS camera. In the text the top-bottom direction is referred to as zenith-nadir. Credits: [25]

Although only two pairs of beams are visible in Fig. 2.1, the third pair is positioned along the north-south axis, with one beam directed towards the chamber from the front (south) and the other from behind (north). The viewports for these beams are equipped with 780 nm anti-reflective coatings to reduce light reflections at the trap wavelength, which enhances trapping efficiency.

For simplicity, the setup uses only three beams—one per axis—instead of six. Each beam is reflected back by mirrors to create the counter-propagating beams required for the MOT. This configuration is feasible since the power imbalance caused by the MOT's absorption of the reflected beams is expected to be negligible.

Collimators are placed along each beam path to maintain a non-diverging beam with the desired beam waist. The mirrors, with a 25 mm diameter, are coated for near-infrared wavelengths using a dielectric layer. Additionally, a $\lambda/4$ waveplate is positioned before each mirror to ensure the correct polarization after reflection, as the MOT requires σ^+ and σ^- polarizations.

In addition to the laser beams, the MOT requires a magnetic field gradient. This is achieved using a pair of coils connected in an anti-Helmholtz configuration, where the coils generate magnetic fields with the same direction but opposite orientations. This configuration ensures a zero magnetic field at the center of the chamber and a non-zero field gradient in all directions. In this experiment, the MOT gradient is measured to be 1.332 G·cm⁻¹/A in the axial direction, and the atom dynamics are investigated using coil currents ranging from 4 A to 11 A [26].

Since it is crucial for the experiment to rapidly switch the magnetic field on and off, this task is performed using a MOSFET controlled by a TTL signal generated by the Field-Programmable Gate Array (FPGA). The magnetic field was measured with a Hall probe [Appendix A.1], with the measurement displayed on the oscilloscope. A trigger signal is sent to the oscilloscope simultaneously with the TTL signal that switches the MOSFET on and off, revealing switching times on the order of a few milliseconds (Fig. 2.2).

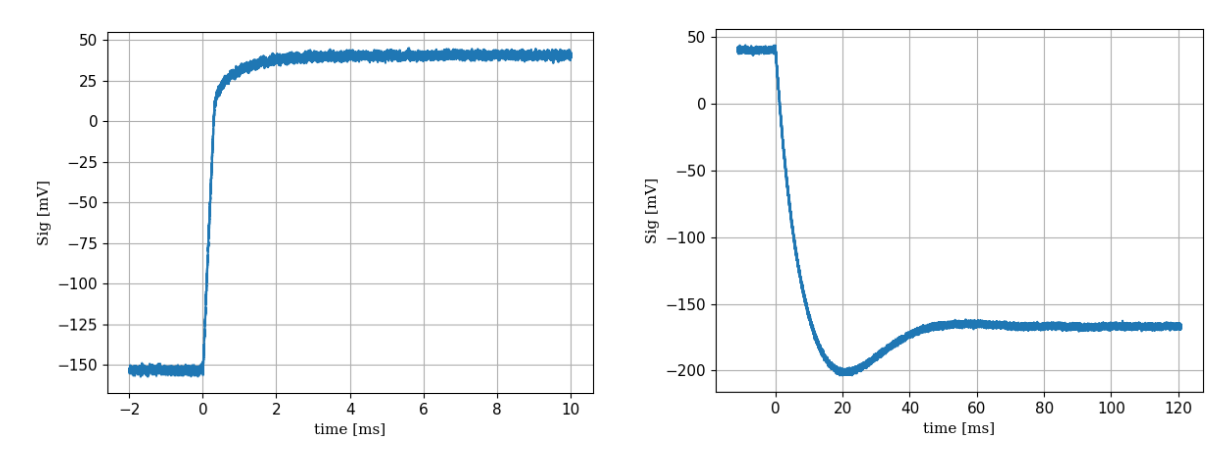


Figure 2.2. Signal of the Hall prove switching off (left) and on (right) the magnetic field.

Although the compensation coils are not visible in the figure above Fig. 2.1, it is important to introduce their role. In this experiment, it is crucial to achieve a zero magnetic field at the center of the trap, precisely where the six laser beams intersect. However, external magnetic fields (such as the Earth's) can interfere with this condition, making it difficult to reach a perfectly field-free region.

To address this, the setup includes three pairs of compensation coils arranged in a cubic configuration. Each pair is oriented along a different axis: North-South, East-West, and Top-Bottom (Zenith-Nadir). These coils are arranged with parallel currents and can operate within a current range of ± 1 A, which allows each pair to generate a magnetic field of approximately $\approx \pm 1$ G at the center of the main chamber.

The vacuum in this chamber was obtained in two steps: first, using an external pump that achieved a pressure of approximately $\sim 10^{-7}$ mbar, and then with an internal pump attached to the chamber that reached a pressure of approximately $\sim 10^{-10}$ mbar.

The external pumping system consists of a diaphragm pump, which acts as both a roughing and backing pump, and a turbo pump. Once the diaphragm pump brought the pressure down to approximately \sim mbar, as measured by the Pirani pressure sensor, a turbo pump was activated. At that stage, the diaphragm pump served as the backing pump, expelling the remaining gases.

The internal pump is composed of an ion pump and a passive non-evaporable getter (NEG), which is a passive component that absorbs residual gases. It can be reactivated, but no more than 100 times; otherwise, it will deteriorate [27]. This setup allowed the system to achieve a pressure of approximately 10^{-10} mbar.

After this procedure, opening the rubidium source increased the pressure to approximately 10^{-8} mbar, as measured by the Pirani sensor connected to the internal ion pump, which remained active as a pressure monitor. This pressure level is employed during the experiment, as a low background gas pressure is crucial for achieving a stable and reproducible MOT.

The Rb atoms to be trapped in the MOT and loaded into the HCPCF [Appendix A.2] are provided by a source connected to a vacuum valve on the chamber. A glass vial contained 1 g of pure ⁸⁷Rb, and by heating the bellow, the Rb sublimates and enter into the chamber. The heating process is achieved using a heating band wrapped around the bellow, powered by a variac.

2.3 Laser system

As mentioned in the previous Section 1.3.4, it is essential to consider the hyperfine structure, defined by the total angular momentum quantum number F = I + J. For the Rb atoms, the $5^2S_{1/2} \rightarrow 5^2P_{3/2}$ and $5^2S_{1/2} \rightarrow 5^2P_{1/2}$ transitions are the components of a fine-structure doublet [18], and each of these transitions have hyperfine structure.

For cooling D_2 transition $5^2S_{1/2} \to 5^2P_{3/2}$ is chosen and occurs at a wavelength of approximately 780 nm. In the D_2 transition, the ground state splits into two hyperfine levels, F=1 and F=2, with I=3/2 and J=1/2, as shown in Fig. 2.3. The atoms can decay into either of these hyperfine levels, with the probabilities determined by the Clebsch-Gordan coefficients [18, 28].

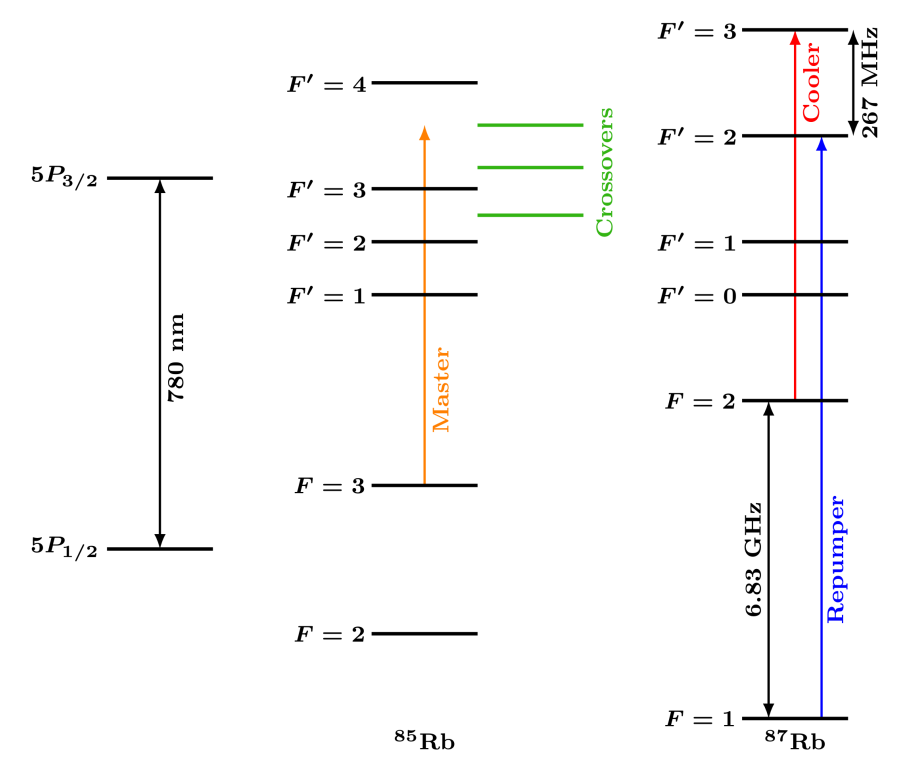


Figure 2.3. D_2 transition, the reference for the Master laser in orange, for the Cooler in red and for the Repumper in blue.

The cooling (and trapping) transition is chosen to be $F = 2 \rightarrow F' = 3$, most atoms decay back into their initial states since this is a cyclic transition. This allows the atoms to interact with the trapping beams for many consecutive cycles. However, a small fraction of the atoms may be off-resonantly excited to the F' = 2 and then decay into the dark state F = 1, which is not addressed by the trapping laser. These atoms experience no trapping forces and eventually escape the trap.

To prevent atom loss, a second field, known as the repumping field, is introduced. This field excites the atoms in the dark state from F = 1 to F' = 2, allowing them to decay back into F = 2, where they can be cooled and trapped again. To lock this repumping frequency, an additional Master laser that has the frequency of another hyperfine level has been introduced, which will be discussed later.

2.3.1 Cooler and Repumper

Let's start with the Cooler and Repumper laser system, referring to Fig. 2.4. We will go through the different stages involved: amplification, SHG, AOM, and beat note locking.

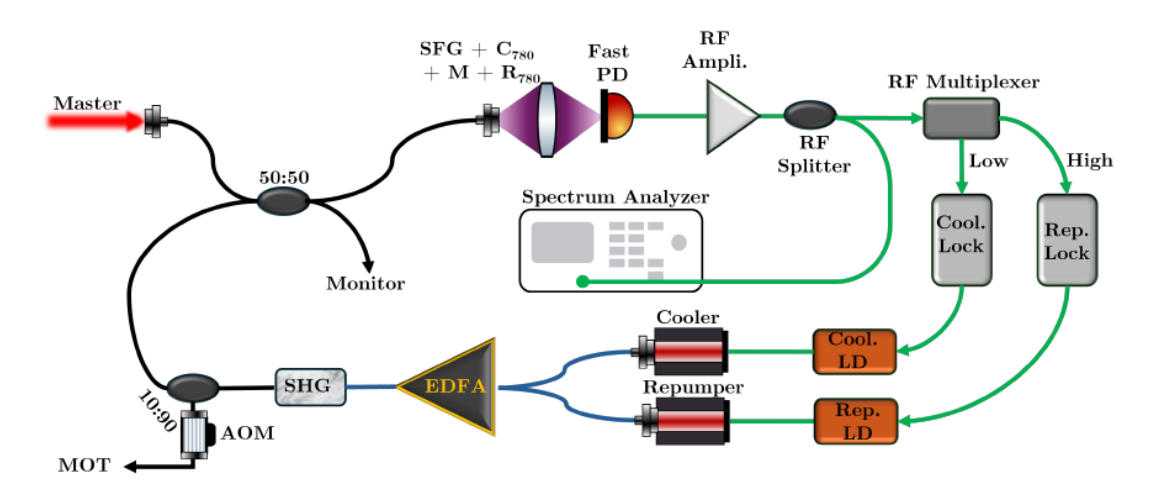


Figure 2.4. Laser system of the Cooler and Repumper lasers. The different stages of amplification, SHG and beat note locking are shown.

The laser sources consist of two $1560 \sim \text{nm}$ laser diodes from Eblana Photonics (EP1562). These diodes are fiber-coupled and combined into a single fiber, which is then directed into an Erbium-Doped Fiber Amplifier (EDFA). Although EDFAs can typically deliver up to $5\,\text{W}$, in our setup it is currently operated at $200\,\text{mW}$.

The fiber-coupled output of the EDFA is sent to a **nonlinear crystal for second harmonic generation** (SHG), which converts the input wavelength from 1560 nm to 780 nm. Since the EDFA output contains two frequencies (the Cooler frequency ν_C and the Repumper frequency ν_R) the nonlinear crystal, in addition to performing SHG for both, also generates light through sum-frequency generation (SFG). This results in an additional frequency component equal to $\nu_C + \nu_R$, which lies halfway between the two SHG frequencies $2\nu_C$ and $2\nu_R$.

After the SHG stage, a beam splitter splits 90% of the laser beam to the MOT apparatus via an optical fiber, while the remaining 10% is sent to the locking system in a separate rack.

Before describing the locking system, it is essential for our experiment to have the capability to switch the MOT beams on and off rapidly. To achieve this, an **AOM** (**Acousto-Optic Modulator**) is placed after the beam splitter 90/10 on the 90% port. Specifically, we use an AOM from Aerodiode with a driving frequency of RF = 100 MHz and a DDS (Direct Digital Synthesizer) control. The frequency and amplitude are modulated in real time by the FPGA, ensuring fast and efficient laser switching of the order of few μ s (in Fig. 2.5).

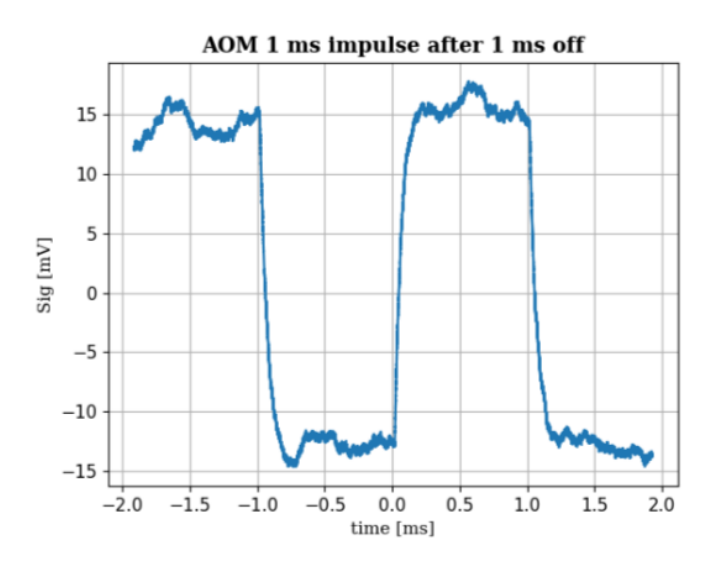


Figure 2.5. The fluorescence of background rubidium gas was acquired on the oscilloscope, switching on and off AOM through the DDS monitored by FPGA.

However, the insertion of the AOM introduces some power losses, reducing the beam power delivered through the fiber from P=13 mW to approximately $P\simeq 8$ mW. Additionally introducing the AOM, a frequency shift of 100 MHz is applied to both the Cooler and Repumper frequencies.

In this experiment, the AOM is utilized solely for the estimation of the MOT temperature. However, the discussion will continue while considering the presence of the AOM. As previously mentioned, the remaining 10% of the beam is used for **laser locking**.

The system responsible for controlling the Cooler and Repumper laser frequencies uses a technique called frequency offset locking, or "beat note locking", which references the Master laser as the primary frequency standard, ensuring a highly stable and precise reference against which the other laser frequencies are measured and locked. The Master laser is locked to the frequency corresponding to the 85 Rb D_2 crossover resonance, specifically the crossover between $F = 3 \rightarrow F' = 3/4$.

The beat notes generated by the relative frequency differences (Fig. 2.6) are used as feedback signals to stabilize the frequencies of the Cooler and Repumper lasers. The monitoring of the Cooler and Repumper beat notes requires the identification of all the peaks present in the power spectrum of the signal generated by the fast photodiode.

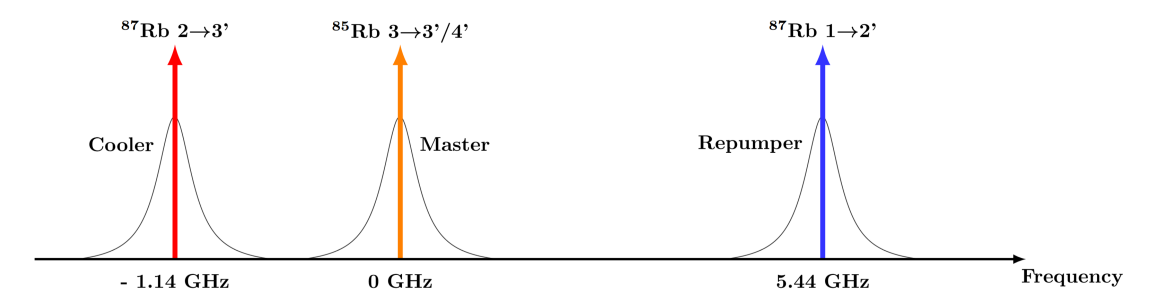


Figure 2.6. Scheme of the positions of cooling and repumping transition frequencies with relative to Master frequency.

In order to lock the frequencies, a reference signal is generated by a DDS (Direct Digital Synthesizer) which generates 10 MHz reference signal and it is monitored by the FPGA. The goal is to maintain the relationship $10\,\mathrm{MHz} \cdot m = f_{locking}$ constant, where m is a constant determined when the frequencies of the Cooler and Repumper lasers are individually locked.

By adjusting the DDS frequency in real time, it is possible to achieve rapid frequency changes, which are crucial for the experiment. As shown in Fig. 2.4, after the fast photodiode, the signal can be visualized on the spectrum analyzer. Additionally, part of the signal is sent through an RF multiplexer, which separates the beat notes of the Cooler and Repumper frequencies. These separated signals are then compared with the 10 MHz reference, and, if necessary, corrections are applied to the laser diodes of the respective lasers.

It is worth mentioning that the laser frequencies can be controlled using dedicated electronic boards, such as Laser Diode Drivers (LDDs) and Temperature Controllers (TCs). Fine-tuning the diode laser's supply current or temperature results in slight wavelength adjustments, which are essential to accurately lock the lasers to the desired frequencies.

2.3.2 Master laser

As mentioned earlier, the Master laser provides the reference for locking the Cooler and Repumper lasers. Since it is convenient for the Master laser frequency to lie midway between these two, the chosen transition is $F = 3 \rightarrow F' = 3/4$ of the ⁸⁵Rb D_2 line.

To identify the correct hyperfine transition and lock the laser, a saturated absorption spectroscopy is used, as described in Appendix A.4. The laser operates at 780 nm and is generated by a Distributed Feedback (DFB) laser diode. Similar to the Cooler and Repumper lasers, it is current-driven and temperature-stabilized using external electronics.

Initially (Fig. 2.7), a beam splitter (Thorlabs BSX11) reflects 90% of the Master laser light, while the remaining 10% is transmitted and labeled as the **probe beam**, which is used for spectroscopy measurements. The reflected portion is directed toward a second beam splitter (Thorlabs BSN11), which reflects 10% of the light to form the **pump beam**, responsible for optically pumping the rubidium atoms during the saturated absorption spectroscopy. The remaining 90% of the transmitted light serves as a reference for frequency-locking the Cooler and Repumper lasers. The pump beam is then reflected by a pair of mirrors, which allow for fine adjustments in beam position and direction.

Next, the beam reaches a polarizing beam-splitter (PBS) cube, oriented so that 100% of the light is reflected toward the rubidium cell. The probe beam, on the other hand, travels a longer path along the perimeter of the optical box.

After being reflected by a pair of mirrors, the probe beam passes through an AOM, which modulates its frequency as required for the locking protocol. Just before entering the cell, a $\lambda/2$ waveplate rotates the beam's polarization, allowing it to pass through the aforementioned PBS and impinge on the photodiode, which is equipped with two SMA output ports: a slow port and a fast port. The slow output is connected to an oscilloscope, which enables real-time monitoring of the light absorption and reveals the hyperfine structure of the 85 Rb D_2 transition. The fast output is connected to the DDS board, mentioned earlier, which demodulates the spectroscopy signal and extracts its derivative. This derivative serves as an error signal for locking the laser frequency.

This method is particularly effective because the Master laser frequency is locked to a saturation peak, which has an even symmetry with respect to its center. The derivative, being an odd function, naturally provides a convenient error signal for the feedback control loop. To achieve this, the photodiode signal is sent to the same DDS that modulates the laser beam. After demodulation, the signal passes through a PID controller, which regulates the current driver of the Master laser to maintain the desired frequency lock.

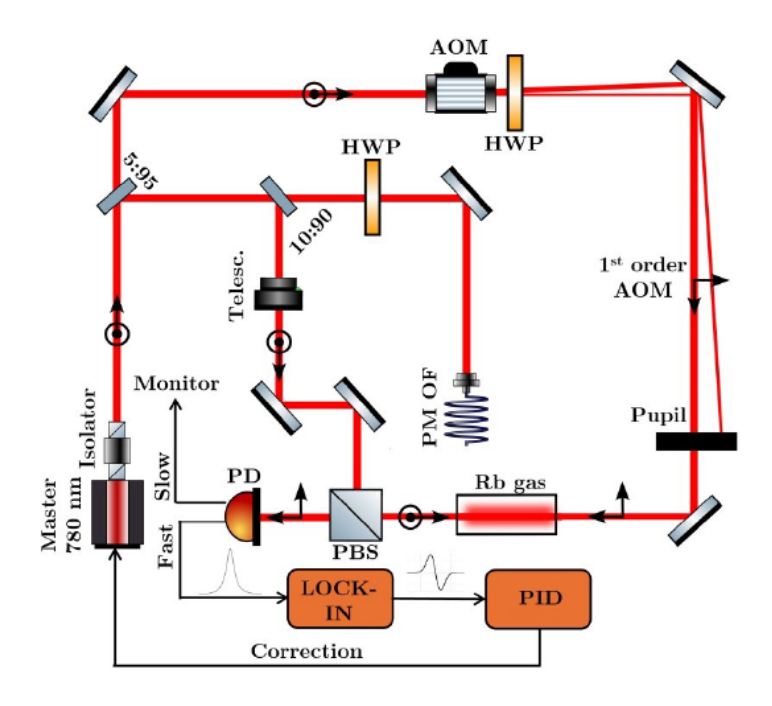


Figure 2.7. Master laser setup schematics.

2.4 Photo-detector

In this setup, the PDA100A(-EC) photodetector, in conjunction with a converging lens with focal length $f = 100 \,\mathrm{mm}$ and diameter 4 cm, is placed approximately 430 mm away from the atoms, mounted on a breadboard positioned behind the northern side of the chamber. The converging lens is used to direct more photons onto the sensor. This device is an amplified, switchable-gain silicon (Si) detector designed to detect light signals in the range of 340 nm to $1100 \,\mathrm{nm}$ [29]. Figure 2.8 shows the main components of the photodetector system.

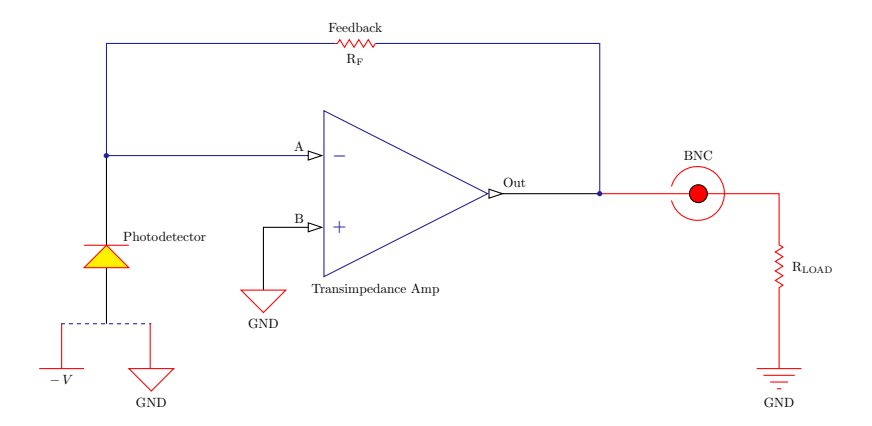


Figure 2.8. The photodetector system circuit with a transimpedance amplifier (TIA).

The **Photodetector** (**PIN Photodiode**) is reverse-biased and converts incoming light (optical power) into a photocurrent. Its responsivity depends on the wavelength of the incident light power and is defined as:

$$\eta = \frac{I_{PD}}{P_{light}} \tag{2.1}$$

where I_{PD} is the generated photocurrent and P_{light} is the incident light power. For our detector, the responsivity is $\eta = 0.52 \pm 0.2$ A/W (see the User's Guide [29], sec. 6.1 at 780 nm).

The **Transimpedance Amplifier** (**TIA**) is implemented using an operational amplifier (op-amp), which converts the photocurrent into a voltage output. The feedback resistor, chosen from an eight-position rotary switch that allows the gain to be varied in 10 dB steps, determines the trans-impedance gain. In this experiment, we selected a gain of $G = 4.75 \times 10^6$ V/A $\pm 5\%$.

The Voltage Output is measured on a digital oscilloscope with a $1 \,\mathrm{M}\Omega$ termination chosen to maximize the output voltage. Since the voltage output is determined solely by the transimpedance gain and the responsivity, the final output voltage is given by:

$$V_{out} = \eta \cdot G \cdot P_{in} \tag{2.2}$$

2.4.1 Number of atoms estimation

The number of atoms trapped by the MOT can be found from the fluorescence of the atom cloud. In particular, we start from the power emitted by a single atom:

$$P_0 = E_p \cdot R_{sc} \tag{2.3}$$

where $E_p = hc/\lambda$ is the energy of a single photon with $\lambda = 780\,\mathrm{nm}$ and

$$R_{sc} = \frac{\Gamma}{2} \frac{s_0}{1 + s_0 + (2\delta/\Gamma)^2} \tag{2.4}$$

is the scattering rate considering $s \ll 1$.

Hence, the power emitted by N independent atoms is

$$P_n = P_0 \cdot N_{atoms} \tag{2.5}$$

and, since the photodiode measures the photons that reach the lens, the fractional solid angle must be considered $\sigma=D^2/(16d^2)=0.98\cdot 10^{-3}$, since the collection lens has a diameter D=50 mm and is placed at distance d=400 mm from the atoms. The power detected by the photodetector is:

$$P = P_n \cdot \sigma \tag{2.6}$$

Now, from Eq. (2.2), it is possible to obtain the output voltage of the photodetector:

$$V_{out} = \eta \cdot G \cdot P = \eta \cdot G \cdot \sigma \cdot N_{atoms} \cdot E_p \cdot R_{sc}$$
(2.7)

from which finally, it is possible to obtain the number of atoms in the MOT:

$$N_{atoms} = \frac{V_{out}}{\eta \cdot G} \frac{1}{\sigma \cdot E_p R_{sc}}.$$
 (2.8)

To apply this equation, it is necessary to determine s_0 .

Since in this part of the experiment the AOM was bypassed, the total power delivered by the fiber is $P=13\,\mathrm{mW}$. The power of the Cooler beam corresponds to 25% of the total power, as measured using a Fabry-Pérot interferometer. By retro-reflecting each beam, the total power output from the three collimators is effectively doubled, resulting in $P_c=6.5\,\mathrm{mW}$. Considering the saturation intensity $I_s=1.67\,\mathrm{mW/cm^2}$ [18]:

$$s_0 = \frac{I}{I_s} = \frac{2P_c}{\pi w^2 I_s} \approx 1.75 \tag{2.9}$$

According to Townsend et al. [30], when considering multi-level effects, the effective saturation parameter is given by $s_{0,eff} = s_0 \cdot 0.73 = 1.28$. However, the number of atoms in the MOT also depends on other factors, such as the strength of the magnetic field gradient, trapping laser's beam diameter, intensity and detuning [31]. In the next chapter, we will analyze its behavior under a selection of these parameters (Section 3.1).

2.4.2 Trap lifetime estimation

The number of atoms contained in a trap is determined by the balance between the capture rate into the trap and the loss rate from the trap. When the loss rates due to non-rubidium background gas collisions and intra-trap atomic collisions are negligible [32], the loading dynamics of a MOT can be described by:

$$\frac{dN}{dt} = R - \frac{N}{\tau}. (2.10)$$

The number of atoms entering the trap per second is represented by R, while the loss rate due to collisions with hot rubidium atoms in the background is characterized by $1/\tau$, where τ it the trap lifetime.

The loading rate R is given by [33]:

$$R = 0.5 \, n \, V^{2/3} \, v_c^4 \, \left(\frac{M}{2kT}\right)^{3/2} \tag{2.11}$$

where n is the density of the Rb atoms, M is the mass, T is the temperature, V is the trapping volume. The parameter v_c defines the maximum velocity of rubidium atoms that can be captured by the trap. The loss rate, given by $1/\tau$, is described by:

$$\frac{1}{\tau} = n \,\sigma \, \left(\frac{3kT}{M}\right)^{1/2} \tag{2.12}$$

where σ represents the cross-section for a vapor-phase atom to collide with, and eject, a trapped atom. The solution of Eq. (2.10), taking an initial condition of N(t=0)=0, reads

$$N(t) = N_s(1 - e^{-t/\tau}) (2.13)$$

where the steady-state number of trapped atoms is given by $N_s = R\tau$. Since the number of atoms is proportional to the fluorescence signal Section 2.4.1, τ can be determined as a fit parameter. Additionally, N_s depends on the background pressure through τ [32], as well as on the trapping laser's beam diameter, intensity, detuning, and the magnetic field gradient of the trap [31].

2.5 Imaging system

To observe atoms in the vacuum chamber, a Complementary Metal-Oxide-Semiconductor (CMOS) camera has been placed on the western side of the chamber (Fig. 1.9). A CMOS sensor consists of an array of coupled transistors that convert incoming photons into electrical charges. The efficiency of this conversion is determined by the quantum efficiency of the device, which depends on the wavelength of the detected photons. The camera used is the BFS-U3-04S2M-CS, a model from the Blackfly S series, manufactured by Teledyne FLIR. It is a USB 3.1 monochrome camera, designed for machine vision applications. The camera is equipped with a Sony IMX287 sensor, featuring a 720×540 pixel resolution with a pixel size of 6.9 μ m. FLIR provides a Software Development Kit (Spinnaker SDK) for camera control, image acquisition, and data processing. In particular, Python support is enabled through the PySpin library, which in this experiment allows for the configuration of an external trigger and the adjustment of the exposure time to $t_{exp} = 0.1$ ms. The external trigger signal is sent from the FPGA to one of the 6-pin GPIO connectors on the camera.

2.5.1 Temperature estimation

The temperature of a gas is defined by its kinetic energy. An atom moving in a three-dimensional space with $\vec{v} = v_x \vec{e}_x + v_y \vec{e}_y + v_z \vec{e}_z$ can be described by the Maxwell-Boltzmann distribution, which is a probability density function:

$$f(v) = \left(\frac{M}{2\pi k_B T}\right)^{3/2} 4\pi e^{-\frac{Mv^2}{2k_B T}} v^2$$
 (2.14)

where k_B is the Boltzmann constant, T is the atomic temperature, and M is the mass of a rubidium-87 atom. Fig. 2.9 shows the Maxwell-Boltzmann distributions at different temperatures. We observe that as the temperature decreases, the distribution narrows (the standard deviation decreases) and the mean velocity decreases.

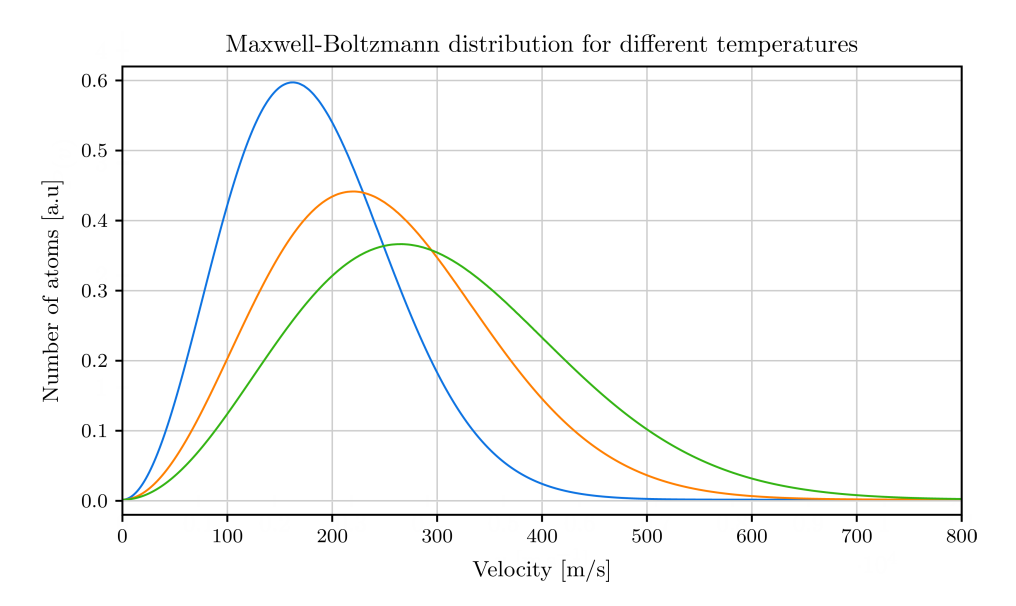


Figure 2.9. Maxwell-Boltzmann probability distribution of speeds for $T = 100 \,\mathrm{K}$ (blue), $T = 200 \,\mathrm{K}$ (orange), $T = 300 \,\mathrm{K}$ (green).

The second moment of this distribution (i.e., the mean of the squared velocity), is:

$$\langle v^2 \rangle = \frac{3k_B T}{M} \tag{2.15}$$

which shows that the mean squared velocity is directly proportional to the temperature. Hence, the quadratic velocity can be expressed as a function of T. When the atoms are cooled, the mean speed approaches zero and the distribution becomes narrower.

In this part of the experiment, the AOM was reintroduced to control the laser beams used for imaging the atomic cloud. Figure 2.10 illustrates the timing sequence employed (not to scale) to measure the Time-of-Flight (TOF) of the atomic cloud. This method involves capturing images at different time intervals after switching off both the cooling laser and the magnetic field. By analyzing the expansion of the cloud in the absence of external forces, the velocity distribution of the atoms can be determined.

This sequence is controlled by an FPGA that manages the DDS for both the cooler reference and the AOM, as well as the MOSFET and the trigger signal. Initially, during the MOT loading phase, the frequency is set to the optimal 1140 MHz. The AOM is then adjusted to an amplitude that allows the laser to pass through the chamber, after which the magnetic field is activated. After 5 seconds, both the magnetic field and the AOM are turned off. At this stage, the cooler reference frequency is shifted to resonance at 1127 MHz, enabling fluorescence from the atomic cloud to be captured. A variable delay is introduced before the trigger signal is activated, allowing the cloud to expand over time; this expansion is used to extract the velocity distribution. Finally, an image frame is acquired, marking the end of the cycle.

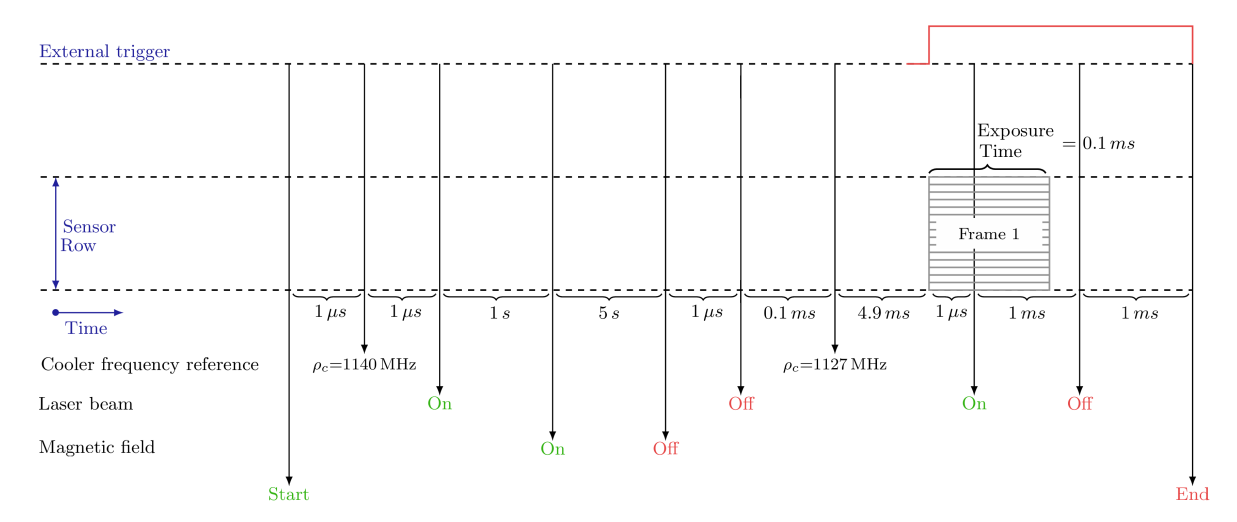


Figure 2.10. Time sequence of a single photo MOT.

Results and discussion

3.1 Number of atoms estimation

The Eq. (2.8) provides the equation used to determine the number of atoms trapped in the vacuum chamber. There are two methods to achieve this measurement:

- The MOT is loaded to its maximum, and then the frequency is switched at a certain detuning δ/Γ .
- The MOT is loaded at a specific detuning δ/Γ , and then the frequency is switched to resonance and the atoms fluorescence is recorded.

In the first method, the number of atoms is determined by averaging the peaks and dips observed during the sweep. This approach also provides information about the Lorentzian broadening and the beat note of the cooler corresponding to resonance.

In the second method, the fluorescence signal directly yields the number of atoms in the cloud, although it does not provide additional information.

It is important to note that when referring to the cooler frequencies and the magnetic field gradient, we are addressing the parameters that can be directly controlled. Specifically, we refer to the beat note between the master and the cooler, which, as mentioned in Section 2.3.1, is negative; however, here we consider its absolute value. Similarly, for the magnetic field gradient, we also sometimes report the values corresponding to the coil current, using the conversion factor $\alpha = 1.332$ G/(cm A). For the compensation coils, the conversion between the controlled current and the resulting magnetic field is approximately 1.4 G/A for each individual coil.

3.1.1 First method

First, the dynamics of the atom capture were recorded using an oscilloscope and a photodiode with gain $G = (4.75 \pm 0.02) \cdot 10^6$ V/A. This measurement allowed us to determine the beat note corresponding to resonance; therefore, a wide range of detuning was scanned. The gradient of the magnetic field was studied in the range of 6.66 G/cm to 10.66 G/cm, by varying the current from 5 A to 8 A. The cooler beat note (in absolute value), $|BN_{\rm photo}|$, was scanned from 1023 MHz to 1050 MHz (see Fig. 3.1 and Appendix A.6). To load the MOT, we must operate at a negative detuning:

$$\delta = -|BN_{load}| + |BN_{resonance}| < 0 \tag{3.1}$$

which implies that $|BN_{load}| > |BN_{resonance}|$. Before selecting the optimal loading frequency (i.e., the cooler beat note at which we achieve the maximum signal and, consequently, the highest number of trapped atoms) a scan over different frequencies was performed. It was determined that the optimal loading beat note for the cooler is $|BN_{load}| = 1036$ MHz for all studied magnetic field gradients, except for 10.66 G/cm that is $|BN_{load}| = 1042$ MHz. The master laser was locked to the $3' \rightarrow 4'$ crossover.

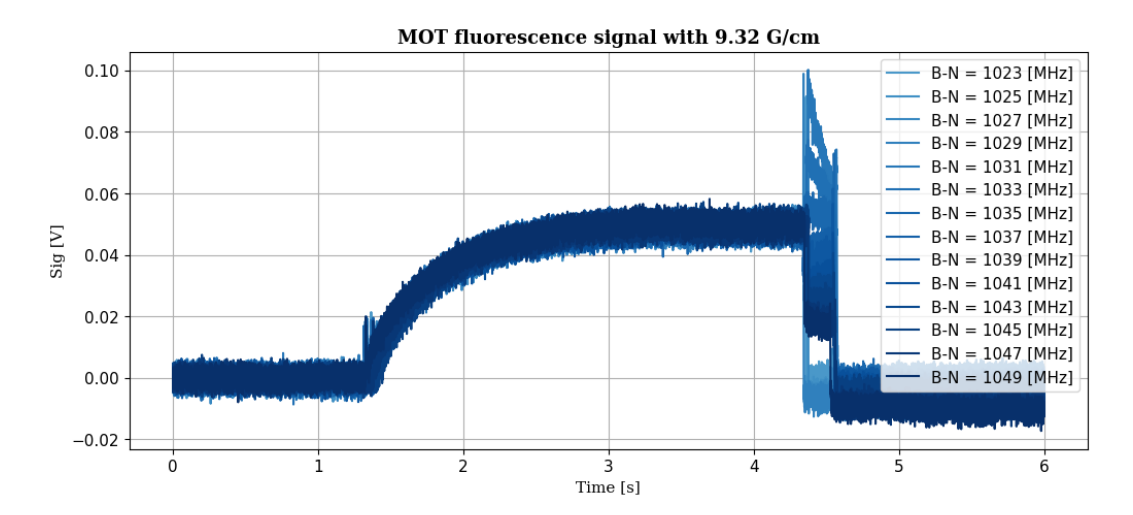


Figure 3.1. Capture dynamics of the MOT photoemission for $B' = 9.32 \,\text{G/cm}$ value of the magnetic field gradient, as recorded on the oscilloscope for various beat-note frequencies (see Appendix A.6 for other results).

Zooming then on the peaks:

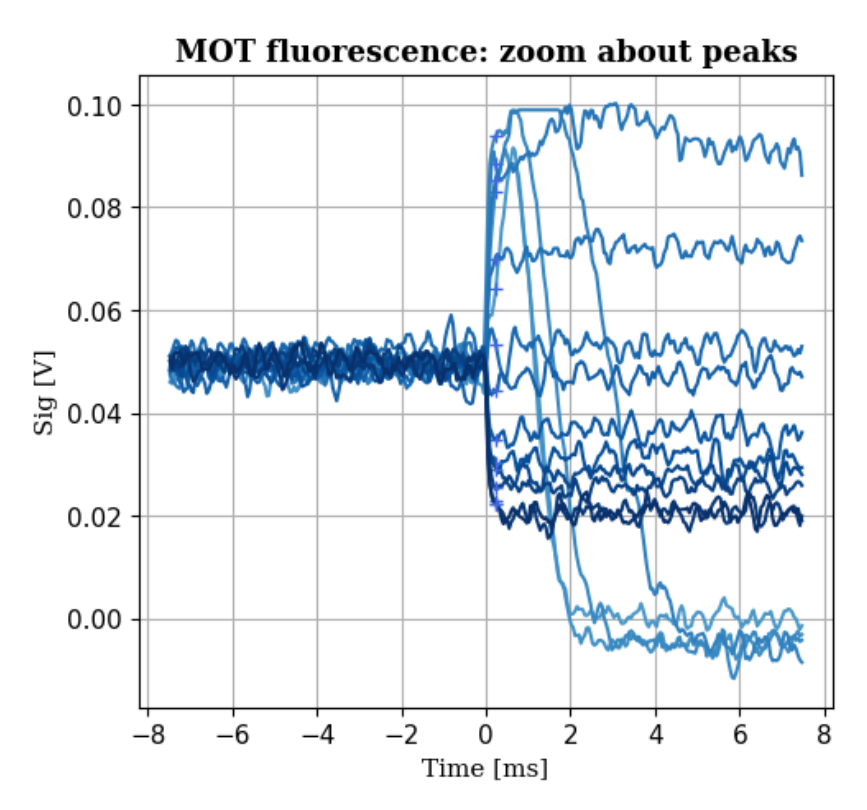


Figure 3.2. Close-up view of the MOT photoemission near the peaks, showing how the signal evolves over time for different beat-note frequencies $|BN_{photo}|$.

From the figure above, it is evident that the signal exhibits several peaks and dips. When the frequencies are below the loading frequency—that is, when $|BN_{photo}| < |BN_{load}|$ (with $|BN_{load}|$ equal to 1036 MHz or 1042 MHz for B'= 10.66 G/cm) —we observe peaks that increase in amplitude as they approach resonance in absolute value (the precise resonance value will be determined later).

Conversely, when $|BN_{photo}| > |BN_{load}|$, the signal drops. However, we aim to analyze the photoemission following Eq. (2.7). To do this, we identify the peaks and drops in the signal by locating the points where its derivative reaches a maximum or minimum. Then, we compute the average signal value over a short interval ($\simeq 0.15$ ms) immediately following these extrema Fig. 3.2. This mean value is taken as the photoemission corresponding to that particular measurement.

The errors are estimated by combining the standard deviation of the initial background (which is subtracted from the signal to zero the offset) with the standard deviation computed over the interval used to determine the peak. Finally a fit is performed using the following function and assuming $s_0 = 1.28$:

$$V_0 \cdot \frac{1}{\left(1 + 4\left(\frac{|BN_{photo}| - |BN_0|}{\Delta f}\right)^2\right)} + y_0 \tag{3.2}$$

where the fit parameters are the amplitude V_0 , the width Δf , the beat-note at resonance BN_0 and the offset y_0 as shown in Fig. 3.3 (and in Appendix A.6).

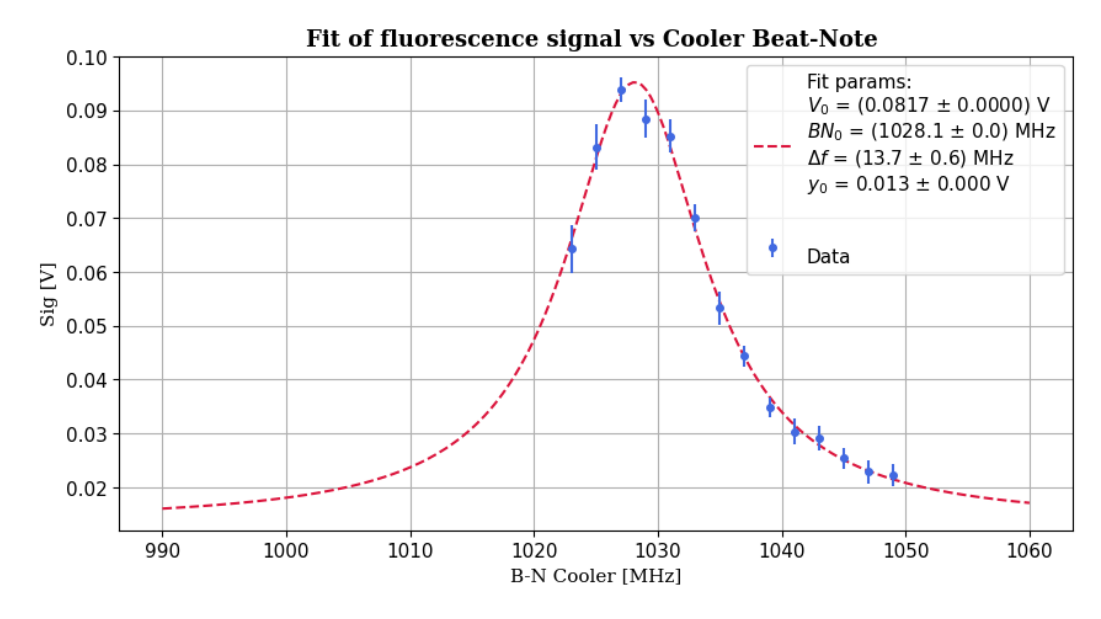


Figure 3.3. Lorentzian fit for $B' = 9.32 \,\mathrm{G/cm}$ (see A.6 for other results)

From the amplitude we obtain the number of atoms:

$$N_{atoms} = \frac{V_0}{(\eta \cdot G \cdot \sigma \cdot E_n \cdot \Gamma)} \cdot \frac{s_0 + 1}{s_0}$$
(3.3)

We observe that Δf remains approximately 14 MHz even at higher magnetic field gradients, within the margin of error, as reported in Table 3.1. This result has been further investigated: while an increasing magnetic field gradient would typically cause more atoms to experience a wider range of Zeeman shifts (leading to a broadening of the Lorentzian profile) the strong gradient could also confine the MOT more tightly around the zero-field point.

As a result, the effective volume of the MOT may be reduced, minimizing variations in the magnetic field gradient experienced by the atoms. However, if Δf were primarily due to power broadening, replacing Δf with

$$\frac{\Gamma'}{2\pi} = \frac{\Gamma}{2\pi} \sqrt{1 + s_0}$$

would yield $s_0 = 9$, which differs significantly from our estimated value of 1.75. This discrepancy suggests that further measurements should be performed in the absence of the magnetic field. Furthermore, for each magnetic field gradient, the number of atoms can be determined by substituting the fitted value into V_0 in Eq. (3.3). The corresponding values are reported in Table 3.1. The associated errors are obtained by propagating the uncertainties in the fit parameter ΔV_0 , the gain ΔG , the responsivity $\Delta \eta$, and the fractional solid angle $\Delta \sigma$.

Magnetic field gradient (G/cm)	6.66	7.99	9.32	10.66
$\Delta f \; (\mathrm{MHz})$	14.6 ± 1.3	17.5 ± 8.1	13.7 ± 0.6	16.6 ± 7.7
Number of atoms (10^6)	8.35 ± 2.09	7.06 ± 1.77	6.52 ± 1.63	11.43 ± 2.86

Table 3.1. Number of trapped atoms and the width Δf (MHz) for different magnetic field gradient values.

It can be observed from Table 3.1 that the number of trapped atoms varies significantly between the first three values (obtained for $B' = 6.66, 7.99, 9.32 \,\mathrm{G/cm}$) and $B' = 10.66 \,\mathrm{G/cm}$. These differences are primarily due to the choice of $|BN_{load}|$. In particular, for $B' = 9.32 \,\mathrm{G/cm}$, the number of trapped atoms deviates significantly from its optimal $|BN_{load}|$, as will be discussed in the following section. As a result, it does not reach the maximum atom number that could be captured with its optimal value.

We can anticipate that, with the optimal $|BN_{\text{load}}|$, the number of trapped atoms would increase by 40%, making it comparable to the value obtained for $B' = 10.66 \,\text{G/cm}$, which is confirmed in the following section.

3.1.2 Second method

In this part of the experiment, we employed various values of $|BN_{load}|$ and then switched to the resonance frequency previously determined as $|BN_0| = 1027 \,\mathrm{MHz}$. In this method, the beat note for each loading is chosen between 1032 MHz and 1048 MHz, while different magnetic field gradients ranging from 5.33 G/cm to 14.65 G/cm are investigated by varying the coils current from 4 A to 11 A in steps of 1 A. The dynamics observed on the oscilloscope are shown in Fig. 3.4 and in Appendix A.6 for four selected magnetic field gradient.

Figure 3.4. Time traces of the MOT fluorescence for different cooler beat-note frequencies (from $1032\,\text{MHz}$ to $1044\,\text{MHz}$) and for a magnetic field gradient of $B' = 9.32\,\text{G/cm}$. These oscilloscope measurements illustrate how the loading dynamics vary with detuning and magnetic field gradient (see Appendix A.6), allowing us to identify the conditions that maximize the number of trapped atoms.

This methodology enables us to determine the detuning and the magnetic field gradient that maximize the number of captured atoms.

The peaks, V_{max} , indicate which loading detuning captures the most atoms, as the highest peak value corresponds to the maximum fluorescence, which is proportional to the number of atoms (essentially serving as a "photo"). See Fig. 3.5 and Fig. 3.7.

It is also noticeable that the signal is significantly smaller compared to the previous experiment, likely due to a vacuum leak on the hollow-core fiber that was discovered later, which led to an increased background pressure.

To determine whether the issue is caused by a vacuum problem, one can estimate the ratio between the voltage at which the MOT signal stabilizes after switching on the magnetic field gradient, V_{load} , and the trap lifetime constant τ . This ratio should remain constant across different experiments if all other parameters are unchanged [34, 35]. However, in Fig. 3.5 is shown the voltage peak values for a magnetic field gradient of $B' = 9.32 \,\text{G/cm}$ (see A.6 for other results).

Moreover, the background signal V_{bkg} , along with V_{load} as previously defined, is shown for only one magnetic field gradient value in Fig. 3.6. Given that the background signal originates from hot atoms, i do not expect it to depend on the cooler frequency over a range of approximately 10 MHz, as the Doppler width is 520 MHz, as mentioned in Appendix A.4.

Once again, using Eq. (2.7), we can determine the number of captured atoms (Fig. 3.7 and Appendix A.6). In this case, since we are on resonance, no beat note is involved in the scattering rate. Therefore, the scattering rate is given by

$$R_{sc} = \frac{\Gamma}{2} \frac{s_0}{1 + s_0}$$

and the corresponding errors are calculated using the same method as before, yielding ΔNa .

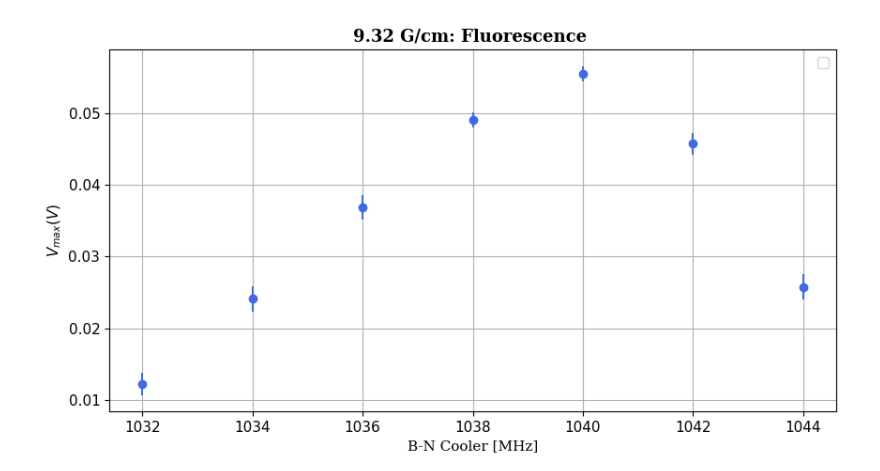


Figure 3.5. Measured peak voltages for B' = 9.32 G/cm as a function of the cooler beat-note frequency, with error bars representing the standard deviation of the background subtracted to set the offset (see A.6 for others).

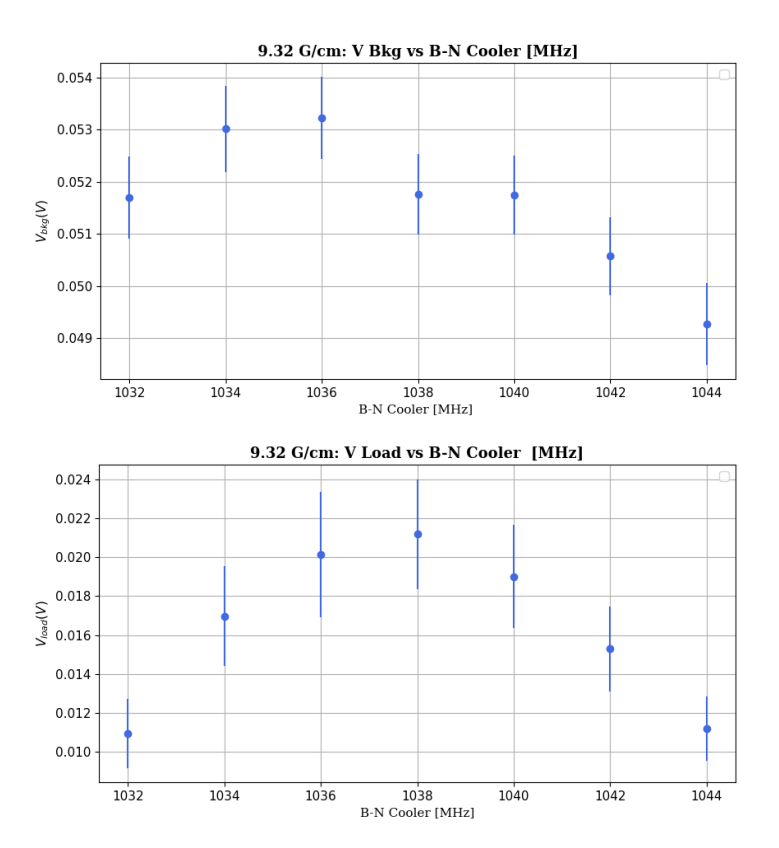


Figure 3.6. Above: Background signals. Below: Stabilized voltage measurements. Both corresponding to a specific magnetic field gradient value ($B' = 9.32 \,\mathrm{G/cm}$), plotted against the cooler beat-note frequency. The error bars represent the standard deviations of the background, subtracted to set the offset.

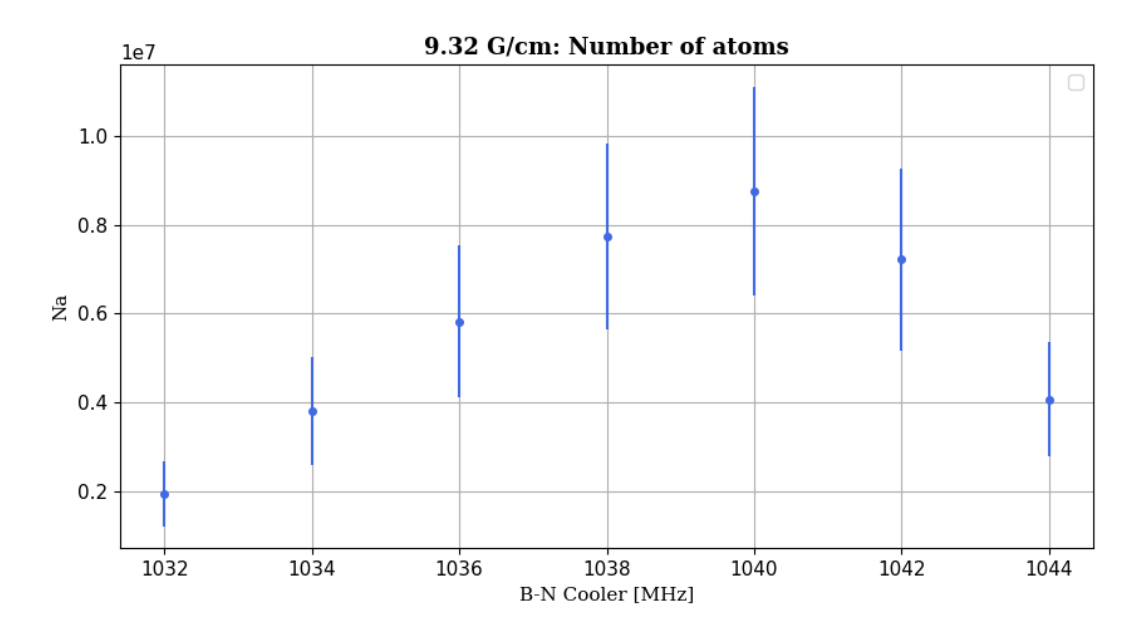


Figure 3.7. Number of trapped atoms as a function of the cooler beat-note frequency for a magnetic field gradient value of $B' = 9.32 \,\text{G/cm}$. The error bars indicate the uncertainties in the atom number measurements (see A.6 for other results).

In Table 3.2 we report the maximum number of atoms in the MOT and the corresponding optimal detuning, for each magnetic field gradient.

I	B' (G/cm)	δ/Γ	$N_a (10^6)$	B' (G/cm)	δ/Γ	$N_a (10^6)$
	5.33	-1.5	5.82 ± 1.80	10.66	-2.2	8.53 ± 2.50
	6.66	-1.8	7.82 ± 2.23	11.99	-2.5	8.01 ± 2.16
	7.99	-1.8	8.60 ± 2.61	13.32	-2.5	7.51 ± 2.13
	9.32	-2.2	8.75 ± 2.36	14.65	-2.8	6.55 ± 1.82

Table 3.2. Optimal detuning in terms of δ/Γ and corresponding atom numbers (N_a) for different magnetic field gradients B'.

It can be observed that increasing the current supplying the MOT coils, i.e. increasing the magnetic field gradient, leads to a higher optimal detuning. This is because as the magnetic field gradient increases, the Zeeman shift becomes larger, necessitating a greater detuning to compensate.

From these two methodologies for measuring the number of captured atoms, it can be confirmed that the MOT traps approximately 10^7 atoms under optimal detuning and magnetic field gradient conditions. Furthermore, as shown in Fig. 3.7, the number of trapped atoms can vary significantly depending on the cooler beat-note frequency. In particular, for $B' = 9.32 \,\text{G/cm}$, the atom number increases by approximately 40% when shifting from a beat-note frequency of $1036 \,\text{MHz}$ to the optimal value of $1040 \,\text{MHz}$, confirming the findings of the previous section.

3.2 Optimal Magnetic Field gradient

Once the optimal detuning value is obtained, we can determine the optimal magnetic field gradient at which the maximum number of atoms is captured. In our experiment, this occurs for $B' = 9.32 \,\mathrm{G/cm}$.

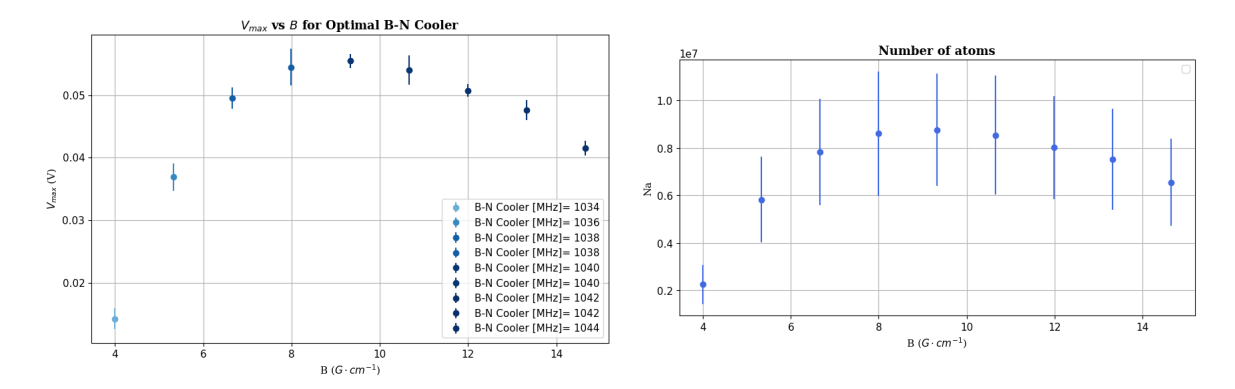


Figure 3.8. Comparison of the measured optimal voltage peak (V_{max}) and the corresponding number of trapped atoms as functions of the magnetic field gradient.

This behavior is consistent with the findings of [31]. For the magnetic field gradient value that captures the largest number of atoms, namely $B' = 9.32 \,\text{G/cm}$, we carried out a more precise study of the optimal detuning. However, considering an uncertainty of 1 MHz per laser, we set the optimal detuning for $B' = 9.32 \,\text{G/cm}$ to 1040 MHz.

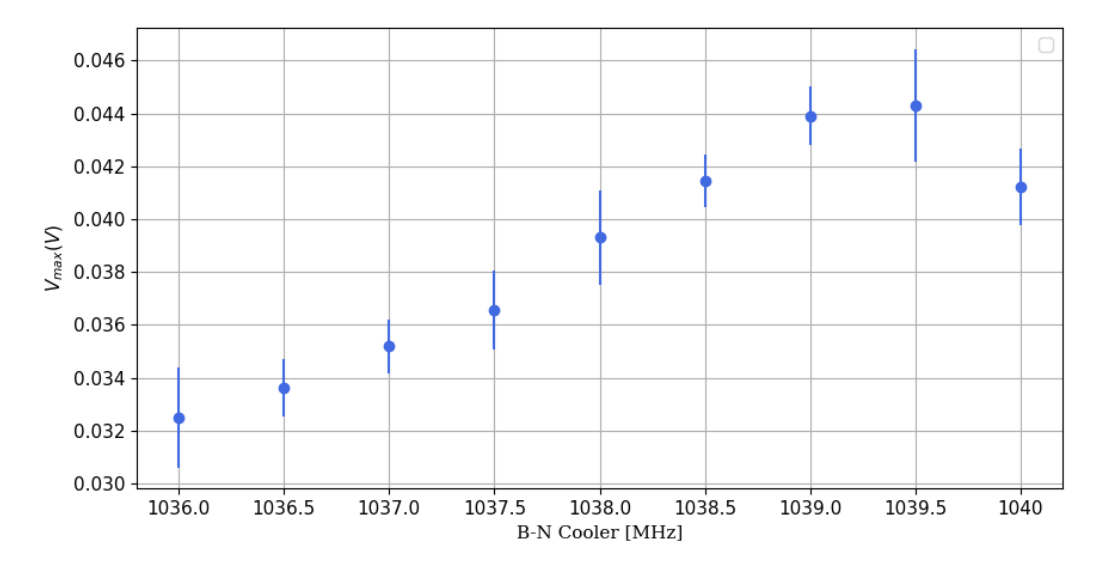


Figure 3.9. MOT fluorescence at $B' = 9.32 \,\mathrm{G/cm}$ as a function of the cooler beat-note frequency, illustrating the approach to the optimal detuning near 1040 MHz.

3.3 Studying Pressure

Since the signal was low, we investigated the vacuum chamber pressure. Since there is no pressure gauge in the main chamber, an estimate of the pressure is only obtained by the ion pump current. To compare, we decided to have an independent estimate by analyzing the background voltage, i.e. the photodetector signal while illuminating the chamber at the loading frequency BN_{load} with no current supplying the MOT coils (see Table 3.3). This background signal is proportional to the atomic density, which is in turn proportional to the pressure, assuming the pressure is primarily due to rubidium.

We performed this study under different conditions. As shown in Fig. 3.10, in the morning the rubidium source was left on, and we measured the background signal (blue point). Later, with the rubidium valve open, the pressure rose, and by the afternoon the background signal was higher (light red point). After these measurements, we closed the rubidium source; 20 minutes later, we took a new measurement that showed a lower background signal (indicating lower pressure). The following day, with the valve still closed, we recorded another measurement (purple curve). We then opened the valve and took measurements every 30 minutes, observing a gradual increase in pressure (shown by the yellow and dark red curves, respectively).

The Fig. 3.11 presents all measurements taken under various experimental conditions, with colors corresponding to the description above. It also includes data at different beat-note cooler frequencies, as these measurements were part of the experiment described earlier, where the number of atoms was compared at different frequencies. They are retained here as they provide additional context for analyzing and comparing background signals.

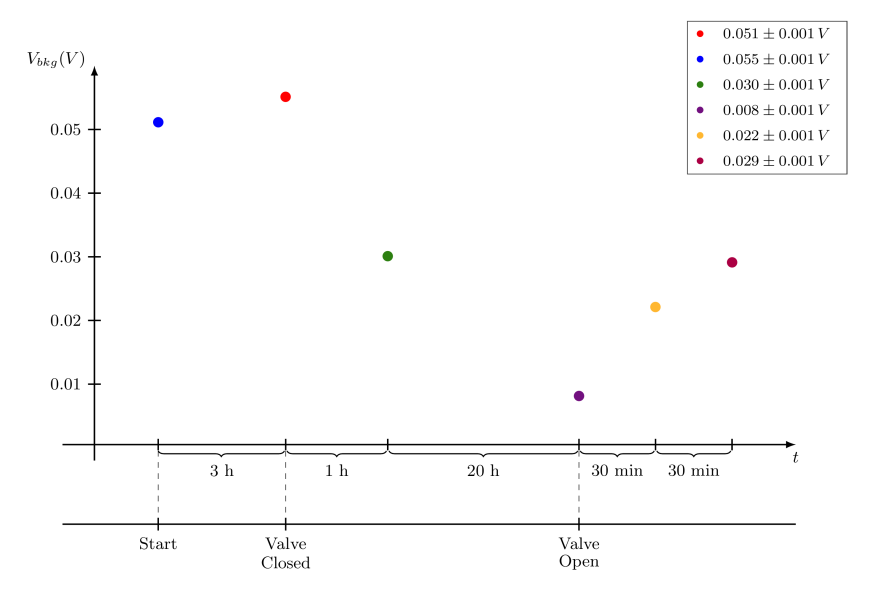


Figure 3.10. Evolution of the background voltage (V_{bkg}) over time, showing how the pressure in the vacuum chamber changes under different operating conditions (e.g., valve open or closed). The color-coded points indicate individual measurements with their respective uncertainties, illustrating how the rubidium source and valve states affect the measured voltage (and thus the chamber pressure).

From Fig. 3.10, it can be observed that over a 24-hour period, the background signal, which provides information about the pressure, decreased from 0.051 V to 0.008 V, corresponding to a reduction of approximately 80%. Consequently, the pressure is expected to decrease by the same proportion. However, this is not an efficient method, as achieving a higher or lower pressure requires manually adjusting the rubidium source valve and subsequently analyzing the background signal. A more reliable approach would be to control the pressure in real time by monitoring the ion pump current. Ideally, a more sensitive measurement would be preferable, as Table 3.3 shows that the current reading is not highly sensitive.

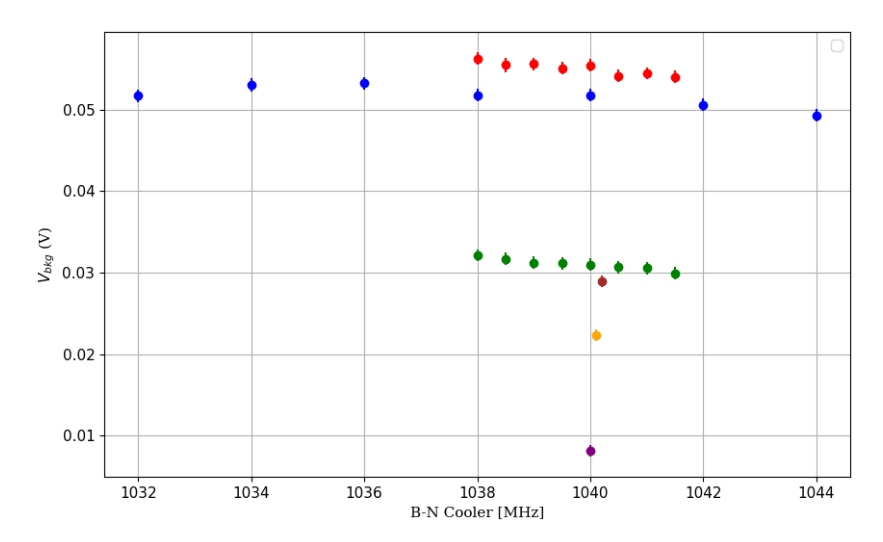


Figure 3.11. Background voltage (V_{bkg}) measured at various cooler beat-note frequencies, illustrating how the chamber pressure (inferred from the background signal) changes under different conditions. The color-coded points represent measurements taken at different times or valve states.

Ion pump current (μA)	1	2	2	0.9	0.9	0.9
$V_{bkg} \; (\mathrm{mV})$	51 ± 1	55 ± 1	30 ± 1	8 ± 1	22 ± 1	29 ± 1

Table 3.3. Ion pump currents compared to the background voltage. Both follows from left to right the temporal sequence in Fig. 3.10.

As seen in Fig. 3.10, the currents, which should be on the order of nA, are significantly higher, indicating that vacuum issue had already begun to arise. However, it is evident that measuring the background voltage V_{bkg} provides a more accurate and sensitive assessment than the ion currents, as previously discussed.

3.4 Trap lifetime estimation

In this section, we study the trap lifetime using Eq. (2.13) and its dependence on detuning, magnetic field gradient, and pressure. From the oscilloscope data, I decided to remove the spike caused by electronic fluctuations when the magnetic field is switched on, as these fluctuations could affect the fitting of the parameter τ of the fit. In Fig. 3.12 we present both the original data and the data with the spike removed, while in Fig. 3.13, we show the corresponding fit obtained for a specific detuning and magnetic field gradient value.

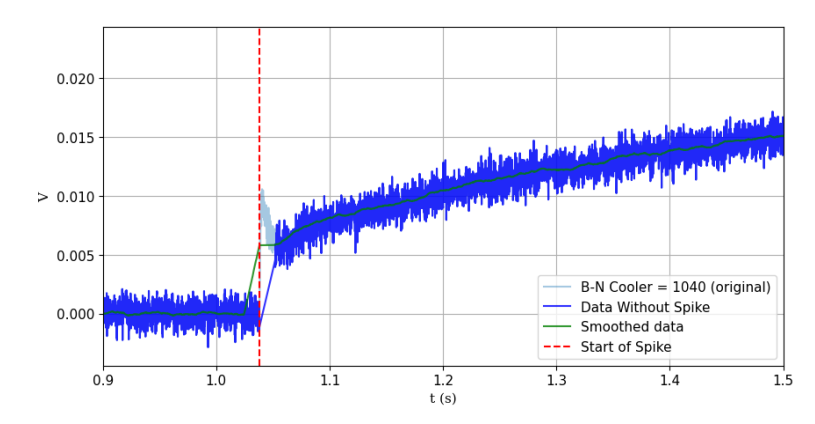


Figure 3.12. Example of the MOT loading curve at $B' = 9.32 \,\text{G/cm}$ with a cooler beat-note of 1040 MHz. The original and smoothed fluorescence signals over time, showing the removal of a spike.

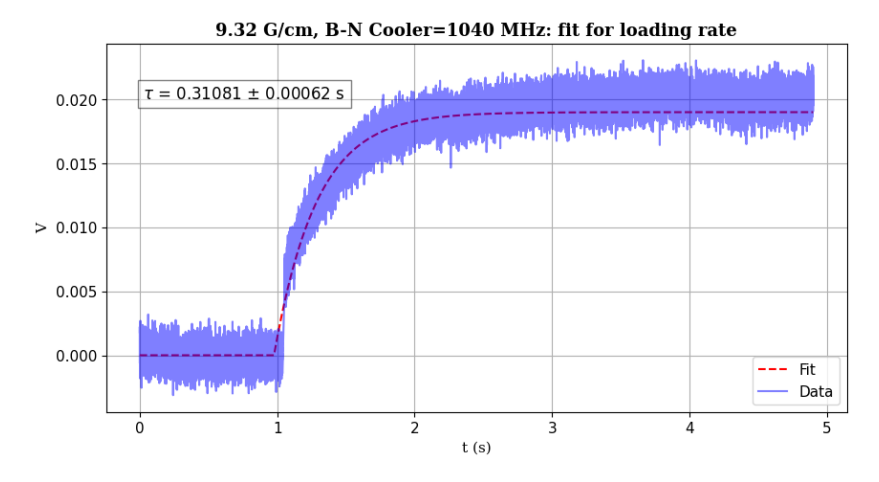


Figure 3.13. Example of the MOT loading curve at $B' = 9.32 \,\mathrm{G/cm}$ with a cooler beat-note of 1040 MHz. A fit to the data without the spike for determining the lifetime τ , with the best-fit value indicated in the legend.

From Fig. 3.13, it is evident that the error on τ is significantly underestimated. As a result, the χ^2 value is notably large. To obtain a more accurate estimation of the error, I performed fits on seven values of the magnetic field gradient at B'=9.32 G/cm at $|BN_{load}|=1040$ MHz, obtaining the values reported in Table 3.4. From the weighted average, we obtain $\tau=0.356\pm0.008$ s.

au (s)				
0.37178 ± 0.00045	0.37013 ± 0.00037	0.35366 ± 0.00042		

au (s)					
0.36202 ± 0.00040	0.31372 ± 0.00035	0.34624 ± 0.00037	0.34143 ± 0.00041		

Table 3.4. Values of τ obtained from the fit of seven independent measurements with a magnetic field gradient of B' = 9.32 G/cm at $|BN_{load}| = 1040$ MHz.

This analysis should be conducted for each value of detuning and magnetic field gradient to achieve a more precise study and to clarify the trend shown in the following figures. Nevertheless, this extended analysis could not be performed. To provide insight into the behavior, the values of τ are still reported with the uncertainties given solely by the fits.

We first studied the behavior of τ for different detunings at a fixed magnetic field gradient. Then, for the optimal detuning at each magnetic field gradient, we examined how τ varies with the magnetic field gradient. See Fig. 3.14.

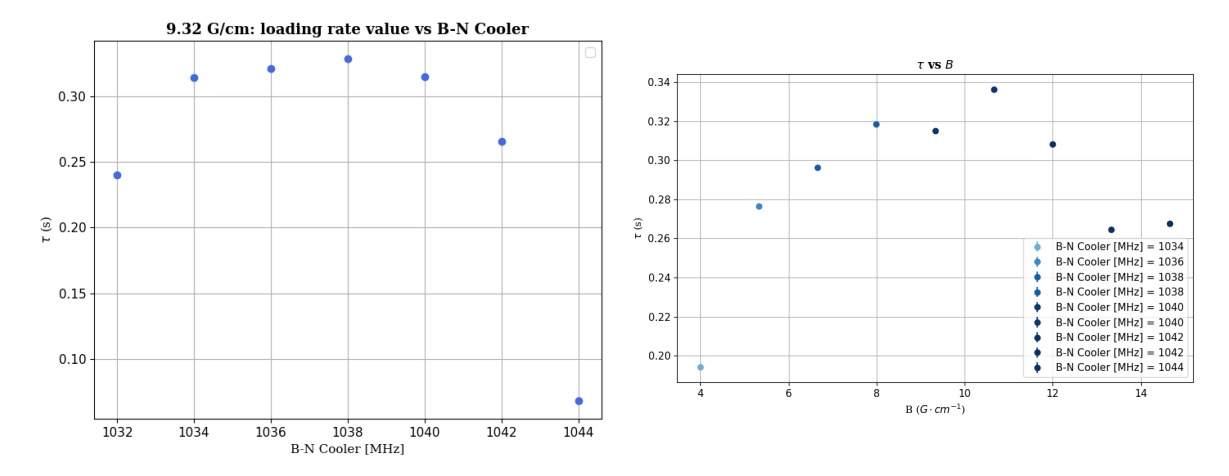


Figure 3.14. (Left) trap lifetime τ as a function of the cooler beat-note frequency at a fixed magnetic field gradient ($B' = 9.32 \,\mathrm{G/cm}$). (Right) τ values at the optimal detuning for each magnetic field gradient, illustrating how the trap lifetime depends on both detuning and field strength.

This behavior is not straightforward to model. In Section 2.4.2, we ignored inelastic intra-trap collisions (characterized by a rate constant β) and did not delve into the details of losses due to collisions with the hot background (τ). The complete solution can be written, following [34], as

$$N_{\rm st} = \frac{R}{\Gamma} (1 - e^{-\Gamma t}),\tag{3.4}$$

where now

$$\Gamma = \gamma + \beta \,\bar{n},\tag{3.5}$$

 \bar{n} is the mean density of the trapped atoms, and $\gamma = \tau^{-1}$ can generally be expressed as

$$\gamma = \sum_{i} n_i \langle \sigma_i v_i \rangle, \tag{3.6}$$

where the sum runs over the different gas species i, with density n_i , speed v_i , and collision cross section σ_i . Through further calculations (see [34]), one finds

$$\gamma_i \propto P_i U_{\rm trap}^{-\frac{1}{6}},$$
 (3.7)

where $U_{\rm trap}$ represents the trap depth, which depends on the experimental parameters and P_i is the partial pressure. Typically, $U_{\rm trap}/k_B \sim 1$ K, making γ only weakly dependent on $U_{\rm trap}$. However, for shallower traps, Gensemer et al. [36] showed that the loss rate varies significantly with $U_{\rm trap}$. The behavior observed in the figures can therefore be explained by noting that trap losses follow the "strength" of the trap potential, which is more effective at suitable detunings and magnetic field gradients.

Regarding intra-trap collisions, at low laser intensities the trap is sufficiently weak that inelastic ground-state hyperfine-changing (ΔF) collisions can eject both colliding atoms from the trap [36]. Since the laser intensity is low, this factor also contributes to the losses.

Anyway, we once again neglect intra-trap collisions, as our goal is to study the dependence of the trap lifetime on pressure, and this simplification allows for a more straightforward analysis. From Eq. (3.7), and considering that $\gamma = 1/\tau$, we can express the inverse trap lifetime (trap loss rate) as:

$$\frac{1}{\tau} = \alpha P_{Rb} + \eta P_{non-Rb} \tag{3.8}$$

Thus, by plotting $1/\tau$ as a function of the rubidium pressure, which, based on the analysis in Section 3.3, corresponds to $V_{\rm bkg}$, we observe a linear trend.

However, as shown in Fig. 3.15, despite this linear behavior, obtaining a reliable linear fit of the form y = ax + b is challenging. This difficulty might arises primarily from vacuum-related issues, which cause fluctuations in the value of b from one measurement to another, introducing uncertainties that affect the accuracy of the fit. Additionally, the limitations of measuring pressure through the background voltage, an approach that might not be inherently optimal for this type of measurement, further contribute to this challenge.

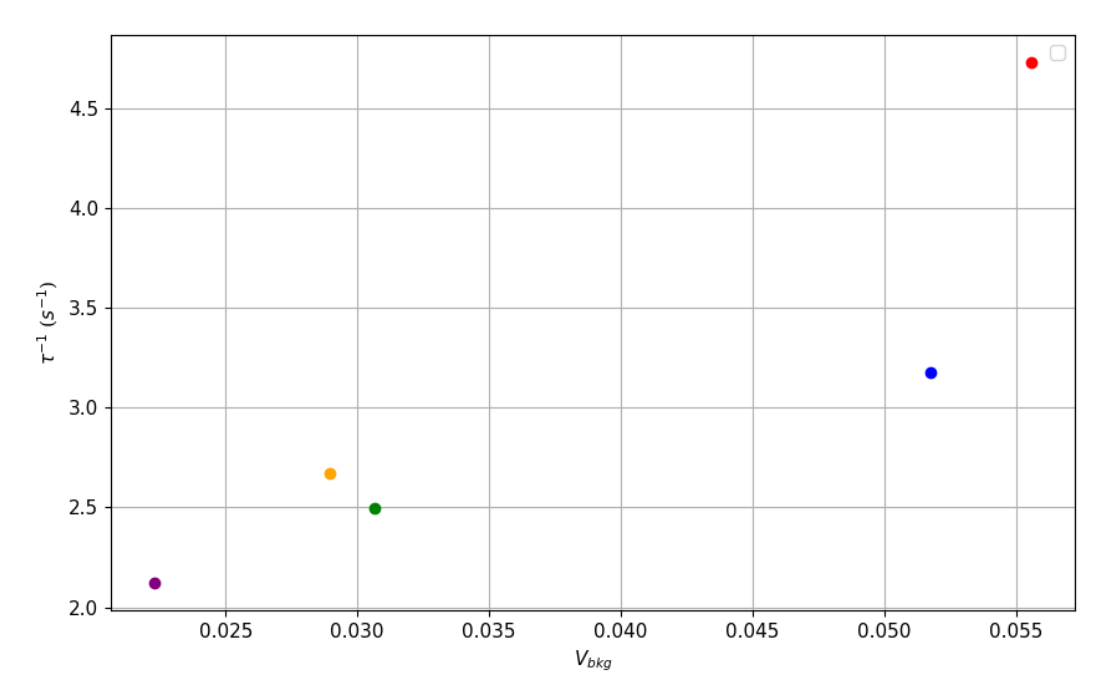


Figure 3.15. Variation of the trap loss rate τ^{-1} with the measured background pressure, illustrating the relationship $\tau^{-1} \propto P$ discussed in Section 3.3

3.5 Temperature estimation

Before proceeding with the analysis of the atomic cloud expansion, a study was conducted by positioning the camera at the top (zenith) window of the vacuum chamber to investigate the potential effects of external magnetic fields (e.g., the Earth's magnetic field) on its expansion. The procedure followed was the same as that described in Section 2.5.1.

It was observed that when compensation magnetic fields were added along the North-West plane (the one visible from the camera positioned at the zenith), the MOT shifted significantly from its center (as identified in the photo by the HCPCF located beneath the MOT), and during the expansion its center of mass was notably displaced. We examined various configurations for the West-East and North-South magnetic fields, but the best performance and expansion were achieved when no compensation fields were applied along these axes. In Fig. 3.16, we show a photo obtained from this camera with no compensation field applied.

Then, the camera was positioned on the West side of the vacuum chamber, and the field compensation along the Zenith-Nadir axis was studied in two configurations: one with the compensation coils active (using a current of -1 A, corresponding to 1.5 G) and one with no compensation Fig. 3.17.

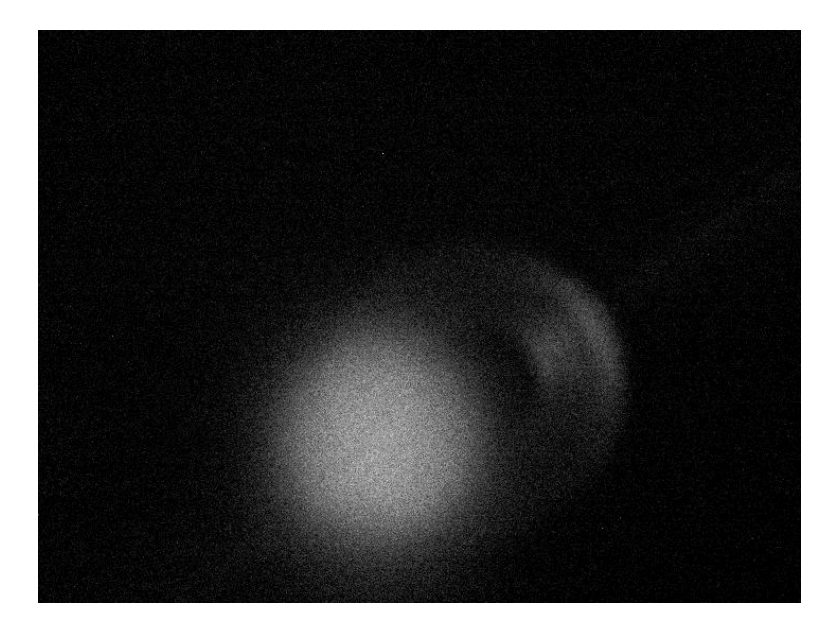


Figure 3.16. Camera at the Zenith side of the vacuum chamber, and a exposure time of the camera $t_{exp} = 0.2 \text{ ms}$

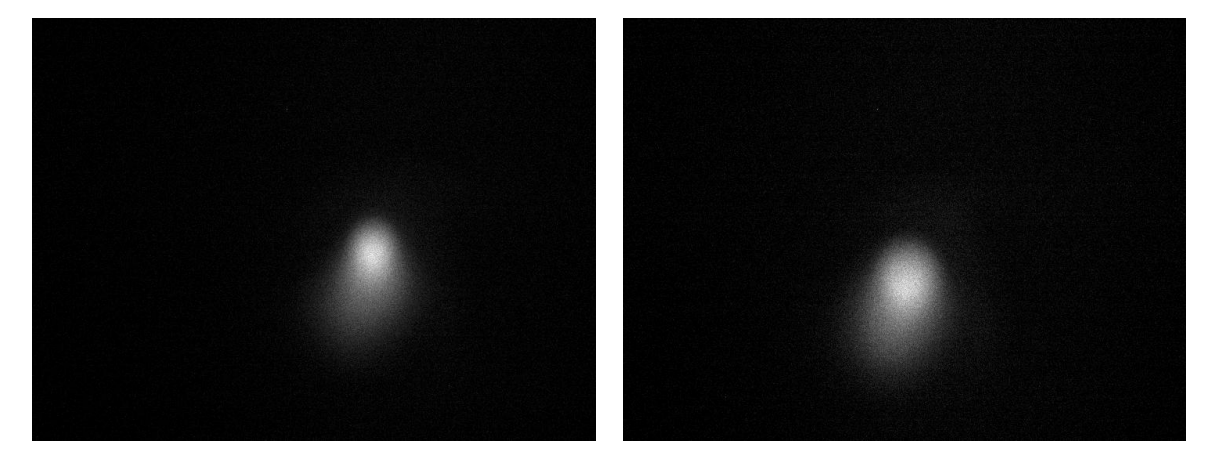


Figure 3.17. Camera at the West side. Left image: Compensation coils acting on Zenith-Nadir axis, Right image: no compensation field applied.

These results show a slight difference in both the position and shape of the cloud. For the expansion study, we chose to analyze the case without any compensation because it exhibits a more spherical shape, making it easier to determine the center of mass. It should be noted that the magnetic field of the ion pump also has an effect, but it is more difficult to compensate for.

Hence, we studied the expansion of the MOT without any compensation field. We acquired images over a time range from 1 ms to 20 ms, in 1 ms increments, starting from the moment when both the laser and the magnetic field gradient were switched off. In Fig. 3.18 a subset of these images is shown, clearly illustrating the expansion of the MOT cloud.

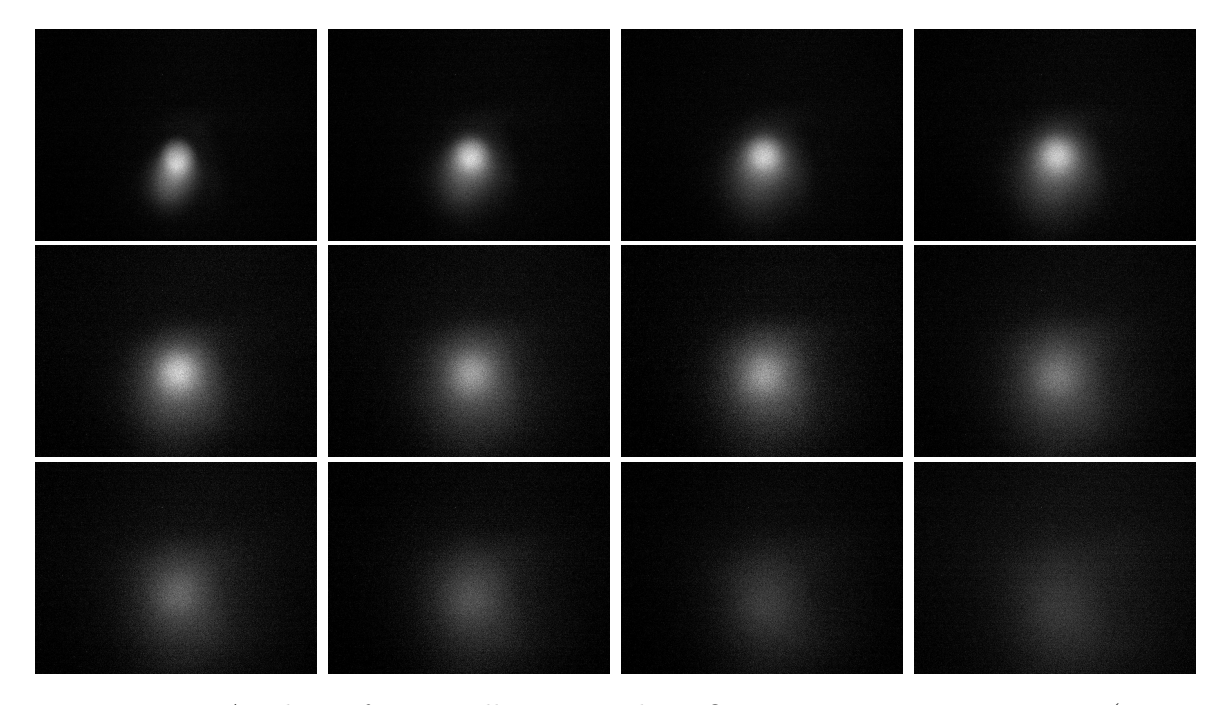


Figure 3.18. A subset of images illustrating the MOT expansion at various times (1, 3, 4, 5, 7, 9, 10, 11, 12, 14, 16, 18 ms) after the laser and magnetic field are switched off. The sequence clearly shows the gradual spread of the atomic cloud once the confining forces are removed.

Before proceeding with the temperature analysis, it is necessary to determine the magnification of the camera. This can be achieved by considering that when the compensation coils are activated, the MOT is displaced. The magnification can be expressed as

$$M = \frac{\Delta x_{\rm CMOS}}{\Delta x_{\rm MOT}},\tag{3.9}$$

where $\Delta x_{\rm CMOS}$ is the displacement of the center-of-mass observed on the camera (taking into account the pixel size of 0.0069 mm), and $\Delta x_{\rm MOT}$ is the actual displacement of the MOT. The latter can be determined from the fact that the zero of the magnetic field shifts according to

$$0 = \frac{\partial B_x}{\partial x} \cdot \Delta x_{MOT} + B_0 \implies \Delta x_{MOT} = -B_0 \left(\frac{\partial B_x}{\partial x}\right)^{-1}$$
 (3.10)

With $\partial_x B = 1.332 \,\text{G/(cm} \cdot \text{A}) \times 7 \,\text{A} = 9.32 \,\text{G/cm}$, $B_0 = 2 \,\text{A} \times 1.4 \,\text{G/A}$, representing the field generated by the compensation coils, the resulting displacement is $\Delta x_{\text{MOT}} \simeq 3.0 \,\text{mm}$.

To measure the corresponding displacement captured by the camera, two configurations were studied, with coil currents set to $2 \,\mathrm{A}$ and $-2 \,\mathrm{A}$ in north-south axis. Due to image saturation and interference from background noise, the center of mass was not accurately calculated. To address this issue, the strategy employed was to remove the background (Fig. 3.19).

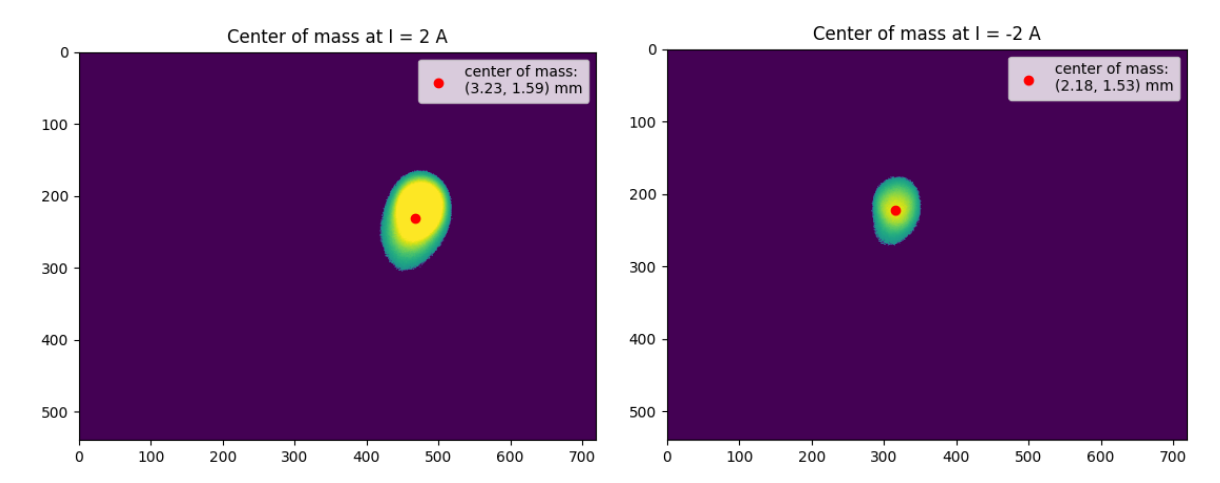


Figure 3.19. Comparison of the center of mass (red dot) without background in the MOT images for coil currents of +2 A (left) and -2 A (right).

Hence from this we've obtained a displacement of

$$\Delta x_{CMOS} = \frac{1.05 \,\mathrm{mm}}{2} = 0.53 \,\mathrm{mm}$$

and hence

$$M = \frac{\Delta x_{CMOS}}{\Delta x_{MOT}} = \frac{0.53\,\mathrm{mm}}{3.0\,\mathrm{mm}} = 0.18$$

For the temperature estimation, we use the second moment of the position distribution of Fig. 3.18:

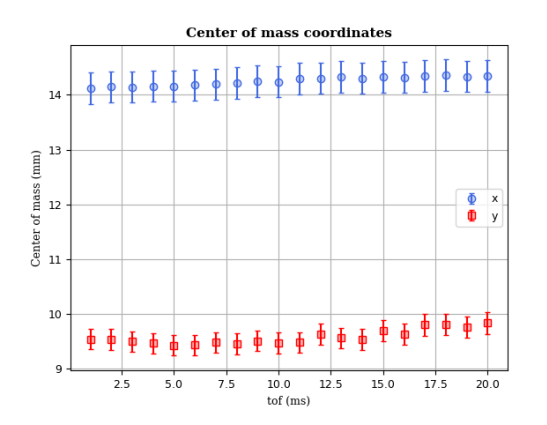
$$\sigma_x^2 = \frac{\sum_j n_j x_j^2}{N} - x_c^2, \tag{3.11}$$

which represents the variance of the atomic cloud along the x-axis.

Here, n_j is the intensity (or number of counts) of the j-th pixel, x_j is its coordinate, N is the total intensity (or total number of counts), and x_c is the center of mass along x. By observing how σ_x^2 evolves over time (after switching off the confining fields in a time-of-flight experiment), one can fit the resulting data to extract the second moment of the velocity distribution through $\langle x^2 \rangle(t) = \langle x^2 \rangle(0) + \langle v_x^2 \rangle t^2$. From this, the temperature can be estimated using a relation of the form

$$T = \frac{M\langle v_x^2 \rangle}{k_B}$$

where M is the (atomic) mass and k_B is the Boltzmann constant. The same procedure applies along the y-axis, thereby providing a full characterization of the cloud's temperature in two dimensions.



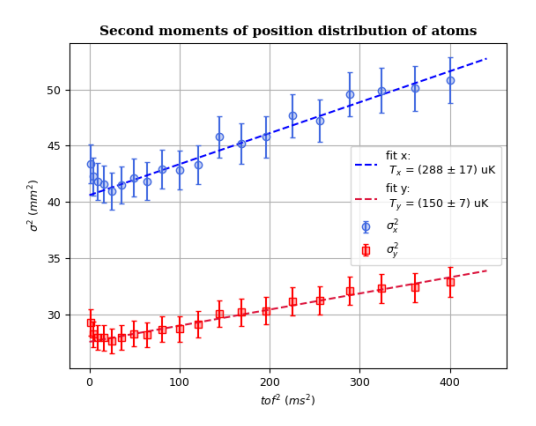
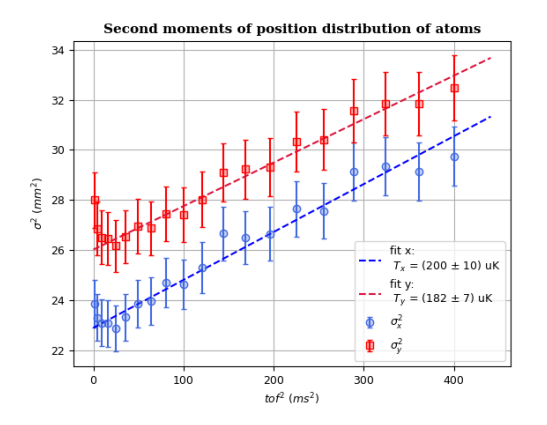


Figure 3.20. (Left) Evolution of the center-of-mass coordinates (x,y) as a function of the time-of-flight (tof). (Right) Second moments of the atom cloud's position distribution (σ_x^2, σ_y^2) plotted against tof^2 . These measurements illustrate both the shifting center of mass and the expanding spatial width of the atomic cloud over time. Note that x and y coordinates refer to the plane captured by the camera positioned on the west side of the chamber.



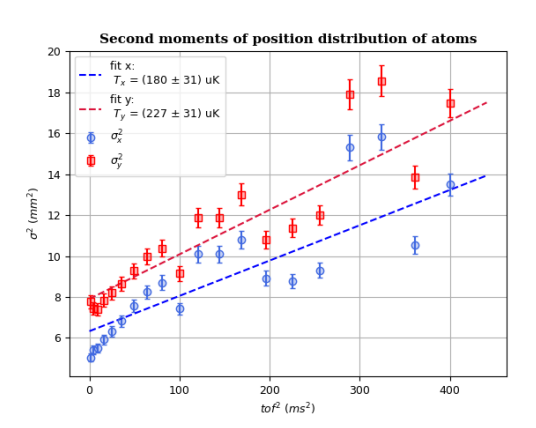


Figure 3.21. Second moments of the atomic cloud's position distribution plotted against tof^2 along with the corresponding fits. (Left) Data processed by selecting a region of interest (ROI). (Right) Data processed by applying a threshold set to three times the background level, setting all pixel values below this threshold to zero.

Fig. 3.20 presents the obtained temperatures, $T_x = (299 \pm 17) \,\mu K$ and $T_y = (150 \pm 7) \,\mu K$. Recalling Eq. (1.47) and Eq. (1.48), and considering $\delta \simeq -2\Gamma$, Doppler theory predicts $T = 2.1 \times 140 \,\mu K$, which is consistent with T_x but deviates from T_y . However, the fact that the temperature along the y-axis was higher than that along the x-axis raised concerns about the reliability of these results, especially since the images showed an evident elongation along the y-axis. Hence, we found that the calculation of the second moments of the atomic cloud's position distribution is particularly sensitive to background noise. In particular, the higher temperature along the x-axis compared to the y-axis may be influenced by the discrepancy in

the number of pixels along the two axes (720 pixels in x vs. 540 pixels in y). To mitigate background effects, I tested two different approaches: applying a threshold to filter out noise and selecting a region of interest (ROI) Fig. 3.21. However, the results varied depending on the chosen threshold or ROI, making the temperature estimates somewhat dependent on these selections. To reduce this dependence, we instead fitted the one-dimensional projections of the atomic distribution (row and column sums) with a sum of two Gaussians.

In Fig. 3.22, we present the results. This approach is particularly useful when the atomic cloud cannot be adequately described by a single temperature or a uniform spatial component. Instead, it may consist of a colder, denser core surrounded by a broader, warmer 'halo' or residual background [30]. By performing a double-Gaussian fit, we can better capture these distinct components than with a single-Gaussian model.

In Fig. 3.22, we plot the squared widths σ_x^2 and σ_y^2 of the narrower Gaussian as a function of tof^2 . Tracking how these widths evolve over time allows us to extract the temperature of the main cloud using the same procedure as before. The temperature obtained for T_y deviate significantly from those previously determined and even after excluding the last four data points, T_y appears to have a higher value. The significant discrepancy between T_x and T_y is likely influenced by the camera not fully capturing the cloud along the y-axis. This effect is particularly pronounced in the last four data points, which have therefore been excluded. When fitting a double Gaussian to the integrated profiles along x and y, the estimation of σ_y appears to be more sensitive to distortions in the cloud's shape. If the cloud is not entirely captured along the y-axis, the fit may return an artificially inflated width, leading to an overestimated temperature. However, given the limitations of the previous method, this approach for determining the temperature is more reliable for our analysis, although it would be preferable to acquire images where the cloud is more centered.

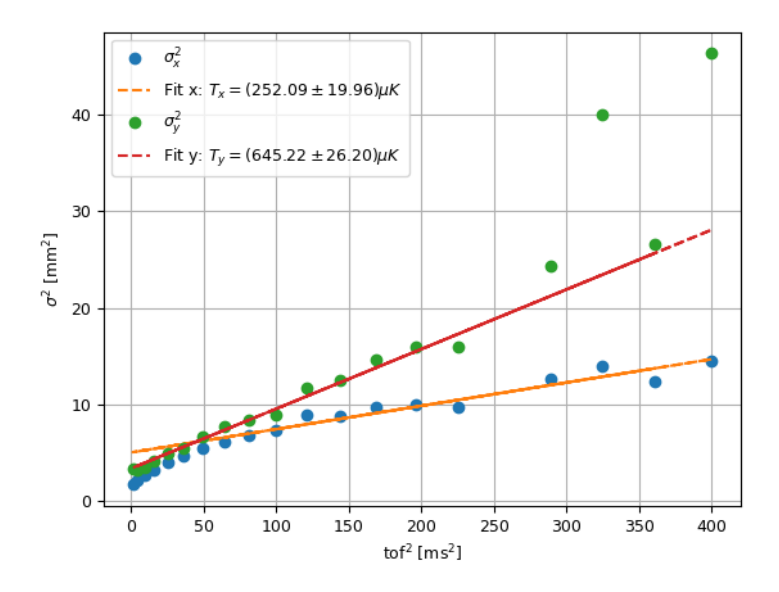


Figure 3.22. squared widths σ_x^2 and σ_y^2 of the narrower Gaussian component, plotted as a function of tof^2 .

3.6 Conclusions

In this work, we have characterized the performance of a magneto-optical trap (MOT) by investigating the dependence of the number of trapped atoms on the laser detuning and the magnetic field gradient. Through a comparative analysis of two measurement methods, we have determined that the MOT is capable of trapping approximately 10^7 rubidium atoms. The optimal trapping conditions were found to be $B' = 9.32 \,\mathrm{G/cm}$ and $\delta = -2.2 \,\Gamma$. Additionally, we observed a strong dependence of the number of trapped atoms on the background pressure inside the MOT chamber. To further investigate this behavior, we found that closing the rubidium source valve can reduce the pressure by up to 80% over a 24-hour period. However, since this method does not allow for measurement and precise control, we leveraged these observations to demonstrate that measuring the background voltage with the magnetic field gradient turned off can help provide an estimate of the pressure. Furthermore, we analyzed the trap lifetime τ , which is also inversely proportional to the partial pressure of rubidium. Under optimal conditions, we obtained a trap lifetime of 0.31 s.

A temperature estimation of the atomic cloud was performed using the time-of-flight (TOF) method. The velocity distributions along the x and y axes yielded temperatures of $T_x = (288\pm17)\,\mu\text{K}$ and $T_y = (150\pm7)\,\mu\text{K}$, respectively. However, we realized that these temperature estimates are unreliable due to the influence of background noise, which affects the second moments of the distribution. To further investigate the temperature, we applied a double-Gaussian fit to the atomic cloud profile and extracted the temperature from the width of the narrower Gaussian component. While the temperature along the x-axis, $T_x = (252.09 \pm 19.96)\,\mu\text{K}$, remained consistent with the previous estimate, the temperature along the y-axis, $T_y = (645.22 \pm 26.20)\,\mu\text{K}$, deviated significantly. This discrepancy, which also departs from the Doppler theory prediction of $2.1 \times 140\,\mu\text{K}$, is likely due to the camera failing to fully capture the atomic expansion along the y-axis. A more accurate estimation of T_y would require acquiring images with the cloud more centered in the field of view.

These findings provide key insights into the optimization of MOT parameters and serve as a foundation for future studies involving the transfer of cold atoms into hollow-core photonic crystal fibers.

One of the main challenges encountered in these experiments was the difficulty in accurately determining the background pressure, on which the number of atoms strongly depends. In our setup, pressure is estimated from the ion pump current, but this method has proven to be unreliable due to the complex relationship between current and pressure, which strongly depends on the specific pump design [34]. A more reliable alternative is to use the trap lifetime τ as an indirect measure of the vacuum pressure [34]. However, this approach presents several challenges, as τ can be affected by additional factors, particularly if the trap depth U_{trap} is relatively low and requires further optimization. Moreover, this method does not provide direct information on the rubidium partial pressure.

Further improvements to the setup could be achieved by increasing the trapping laser intensity to enhance the confinement of the atoms. However, this is currently limited by the second-harmonic generation (SHG) system, which could be damaged under high-power beams. Another crucial adjustment involves optimizing the compensation coils to precisely align the magnetic field zero with the laser beams above the fiber. This would facilitate the implementation of the dipole trap and improve the overall efficiency of atom loading into the hollow-core fiber.



A.1 Hall probe

The Hall effect sensors exploit the Hall effect. Consider a conductor (as shown in Fig. A.1) carrying a current I_x along the x-axis in the presence of a magnetic field B_z along the z-axis.

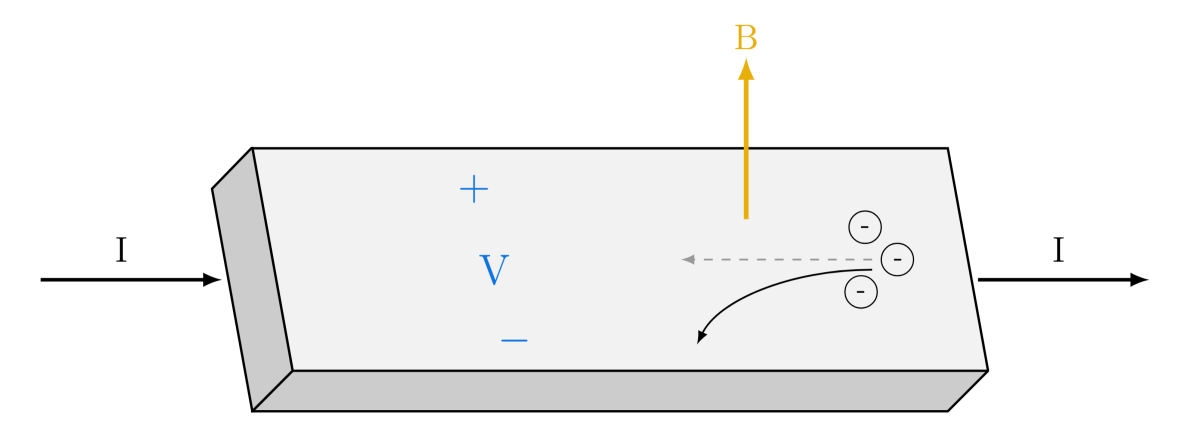


Figure A.1. Schematic representation of the Hall effect in a rectangular conductor. A current I flows from left to right, a magnetic field B is applied upward, and the resulting Lorentz force deflects the charge carriers to one side, generating the Hall voltage V_H .

The moving charge carriers (electrons) experience a Lorentz force given by

$$\vec{F}_L = q \, \vec{v} \times \vec{B},\tag{A.1}$$

which deflects the electrons toward the y-axis. Simultaneously, the corresponding holes (or positive charge carriers) are deflected in the opposite direction. This separation of charge creates an electric field E_y across the y-axis, which, in turn, establishes a Hall voltage V_H . In steady state, the net force on the charge carriers is zero, so

$$\vec{F} = q \left[\vec{E} + \vec{v} \times \vec{B} \right] = q \left(E_y - v_x B_z \right) = 0, \tag{A.2}$$

which implies

$$E_y = v_x B_z. (A.3)$$

The Hall voltage is related to the electric field by

$$V_H = E_u W, \tag{A.4}$$

where W is the width of the conductor (i.e., the distance between the voltage-sensing contacts).

The drift velocity v_x can be expressed as

$$v_x = \frac{I_x}{nqWd},\tag{A.5}$$

where n is the charge carrier density, q is the elementary charge, and d is the thickness of the conductor. Substituting this expression for v_x into the equation for E_y , we obtain

$$V_H = E_y W = v_x B_z W = \frac{I_x B_z}{nq d}.$$
 (A.6)

Thus, the Hall voltage V_H is proportional to the product of the current I_x and the magnetic field B_z , and inversely proportional to the charge carrier density n and the conductor's thickness d.

We employed an A3508 linear bipolar Hall-effect sensor Fig. A.2, whose output is proportional to the magnetic flux density. The sensor's output voltage ranges between 0 and V_{cc} , the single rail supply voltage, with a nominal sensitivity of 2.5 mV/G for $V_cc = 5$ V. In the absence of a magnetic field, the sensor's quiescent voltage is given by $V_Q = V_{cc}/2$. Each monolithic circuit integrates several key components: a quadratic Hall element, temperature compensation circuitry to reduce the intrinsic sensitivity drift of the Hall element, a small-signal high-gain amplifier, and a rail-to-rail, low-impedance output stage. This ensures that the sensor delivers a clean, stable signal that accurately reflects changes in the magnetic field [37].

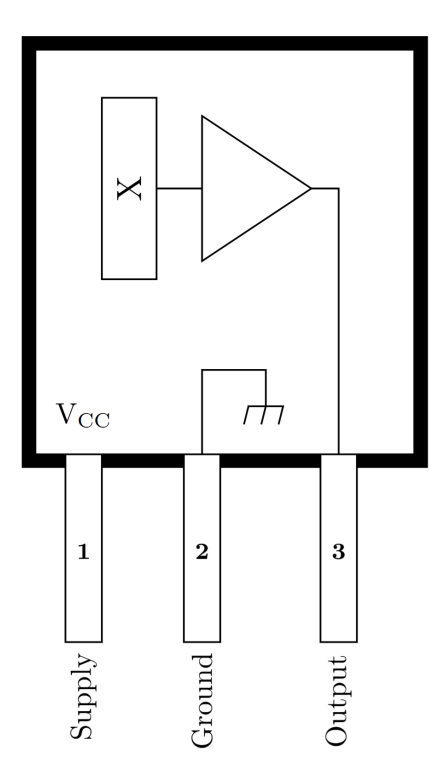


Figure A.2. Simplified block diagram of a linear Hall-effect sensor, showing the Hall element (X), the internal amplifier, and the three pins (supply, ground, and output).

A.2 Hollow-core photonic crystal fiber

In different applications, there is a need for fibers capable of transporting not only light but also physical objects, such as nanoparticles, within their core. These fibers are known as Hollow-Core Photonic-Crystal Fibers (HCPCFs). This is not possible with standard optical fibers, which typically contain a solid glass core, preventing the insertion of physical objects.

To better understand the principles behind Hollow-Core Photonic-Crystal Fibers, a brief discussion on Optical Fibers and Polarization-Maintaining Fibers will be introduced. In particular, the latter played a crucial role in our experiment.

A.2.1 Optical fiber

Regular solid-core optical fibers are cylindrical dielectric waveguides, usually made of silica glass (SiO_2) . The absorption spectrum of this material has a minimum at approximately 1550 nm, which is, in fact, the standard telecommunications wavelength [38]. These fibers consist of a central core with a refractive index n_1 , where light is guided, surrounded by a cladding layer with a refractive index n_2 , and finally protected by a polymeric coating, as illustrated in Fig. A.3.

The fundamental principle that allows optical fibers to function is total internal reflection. When the incidence angle θ_i at an interface between refractive indices n_1 and n_2 exceeds the critical angle θ_c (Fig. A.3), the ray is confined within the fiber. Otherwise, it will be transmitted into the cladding. The critical angle can be determined using Snell's Law [39], yielding:

$$\theta_c = \arcsin\left(\frac{n_2}{n_1}\right). \tag{A.7}$$

As of now, we have considered light as a ray, but a more accurate approach involves treating light propagation in optical fibers as an electromagnetic wave phenomenon. This requires solving Maxwell's equations along with the boundary conditions imposed by the cylindrical dielectric core and cladding. The special solutions of these equations, known as modes, each have distinct propagation constants, characteristic field distributions in the transverse plane, and independent polarization states that remain unchanged as the mode propagates through the fiber. An optical fiber can be considered as a dielectric medium with a refractive index n(r). In the simplest case of a step-index fiber (Fig. A.3), the refractive index is defined as:

$$n(r) = \begin{cases} n_1, & r < a \pmod{n} \\ n_2, & r > a \pmod{n} \end{cases}$$
 (A.8)

where the outer cladding radius is assumed to be much larger than the core radius $(b \gg a)$, allowing it to be considered infinite. Each component of the monochromatic electric and magnetic fields in the fiber satisfies the Helmholtz equation:

$$\left[\nabla^2 + n^2(r)k_0^2\right]U = 0 (A.9)$$

where U represents the electromagnetic potential, and the vacuum wavenumber is $k_0 = 2\pi/\lambda_0$.

To solve the Helmholtz equation in an optical fiber, we exploit the cylindrical coordinates (r, ϕ, z) and we assume a solution of the form [40]:

$$u(r,\phi,z) = R(r)e^{il\phi}e^{i\beta z},\tag{A.10}$$

where l is an integer representing the angular dependence, and β is the propagation constant along the z-direction. This leads to a differential equation for R(r) (see Chapter 9 of [40]) whose solutions are:

$$R(r) = \begin{cases} AJ_l(k_1r), & r < a \text{ (core)} \\ BK_l(k_2r), & r > a \text{ (cladding)} \end{cases}$$
(A.11)

where $J_l(k_1r)$ is the Bessel function of the first kind and order l, and $K_l(k_2r)$ is the modified Bessel function of the second kind of order l and:

$$k_1^2 = n_1^2 k_0^2 - \beta^2, \quad k_2^2 = \beta^2 - n_2^2 k_0^2.$$
 (A.12)

Eq. (A.11) gives the radial distribution of the possible bound modes in a step-index optical fiber with core diameter a. The boundary conditions at the core-cladding interface for the electric and magnetic fields determine that β has to obey for each mode. In particular, for any azimuthal index l, there exists multiple solutions to the boundary conditions with discrete values β_{lm} , m = 1, 2, 3... each representing a different mode. Depending on the properties of the fibre, a different number of modes can actually propagate through it.

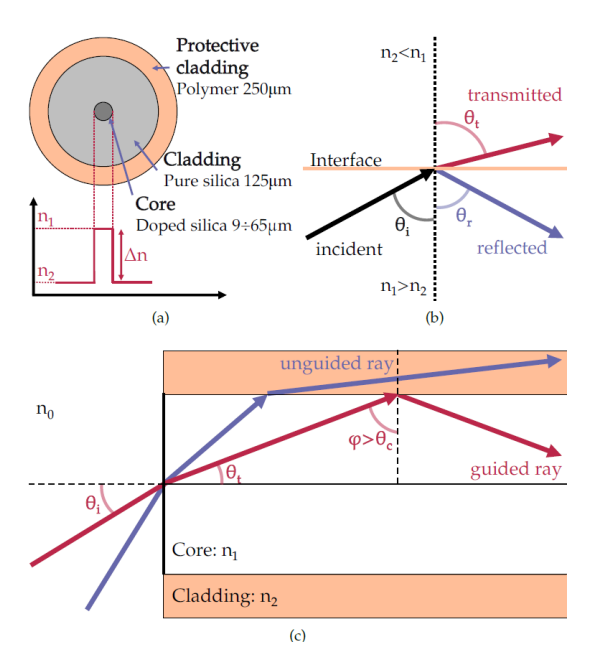


Figure A.3. (a) Cross section of a typical step index optical fibre, highlighting its main components. (b) Visual representation of Snell-Descartes law. (c) Schematic view of light ray guiding in a step index fibre: the incoming light is refracted in the fibre core, if and if its incidence angle at the core-cladding interface is greater than the critical value for total internal reflection θ_c , then the ray can be guided by the fibre.

A.2.2 Polarisation Maintaining Fibres

In an optical fiber with a circular cross-section, each guided mode has two independent polarization states with the same propagation constant. Ideally, no power exchange occurs between them. However, imperfections, mechanical strains, and temperature variations can induce random coupling, leading to the transformation of linearly polarized light into elliptically polarized light at the output.

While this does not affect the total transmitted power and may not pose issues in some applications, it can be problematic in our experiment and others where maintaining polarization is crucial. Therefore, Polarization-Maintaining (PM) fibers are required. As shown in Fig. A.4, none of these fibers exhibit circular symmetry, ensuring polarization preservation.

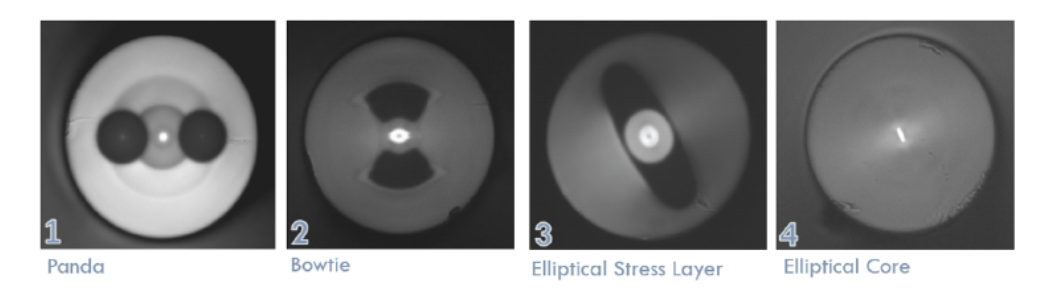


Figure A.4. Cross section images of various types of PM fibres. Credits:[41]

A.2.3 Hollow-Core Photonic Crystal fiber

Hollow-Core Photonic Crystal Fibers (HCPCFs) address the limitations of solid-core optical fibers by utilizing photonic crystal structures in the cladding. These structures consist of periodically varying optical nanostructures that modify the refractive index. Fibers that rely on this approach are known as Photonic Crystal Fibers (PCFs). Moreover, a core defect is introduced with a different geometrical shape or refractive index compared to the unit cell of the cladding.

The Fig. A.5 schematically represents the core and cladding modal content for three distinct types of hollow-core fibers at a fixed frequency: Total Internal Reflection (TIR), Photonic BandGap (PBG), and Inhibited Coupling (IC).

The following discussion is based on the review by Debord et al. [42], which serves as the main reference. As shown in Fig. A.5, the core and cladding modes are further illustrated by the colored bands along the $n_{\rm eff}$ axis, where $\beta = n_{\rm eff} k$. In the figure, cladding modes are represented as orange rectangles, while the intensity profiles of the core modes are also depicted.

In the case of **TIR**, the cladding is a uniform dielectric with a refractive index n_g , allowing modes to exist only within the continuum where $n_{\text{eff}} \leq n_g$. Consequently, the cladding does not support propagating modes for $n_{\text{eff}} > n_g$. However, introducing a core defect with a higher refractive index n_{dg} enables the guidance of discrete core modes within the range $n_g < n_{\text{eff}} < n_{dg}$. These modes remain confined within the core, as the cladding prevents the propagation of modes at their respective effective indices.

The **PBG** utilizes a structured cladding instead of a uniform refractive index and this can overcome of an higher refractive index. This structure gives rise to bands, where cladding modes exist, and gaps, where no cladding modes are allowed. The photonic bandgap effect enables mode confinement even for $n_{\text{eff}} \leq n_{\text{air}} = 1$, thereby supporting guided modes in hollow-core defects filled with gases.

A distinct guiding mechanism, known as **Inhibited Coupling** (IC), is illustrated. Unlike TIR or PBG fibers, IC guidance does not require a higher-index core or a photonic bandgap structure. Instead, core and cladding modes can coexist, maintaining the same (ω, n_{eff}) while remaining isolated from each other without hybridization or leakage. This is possible because modes with the same n_{eff} do not necessarily share the same wavevector. IC guidance has the overlap between the core mode field $|\phi_{\text{core}}\rangle$ and the cladding field $|\phi_{\text{clad}}\rangle$ significantly reduced. Mathematically, this condition is expressed as:

$$\langle \phi_{clad} | \Delta n^2 | \phi_{core} \rangle \to 0,$$
 (A.13)

where Δn represents the transverse refractive index profile function. This condition can be achieved by either reducing the spatial overlap between core and cladding photonic states or by introducing a strong mismatch in their transverse spatial phase.

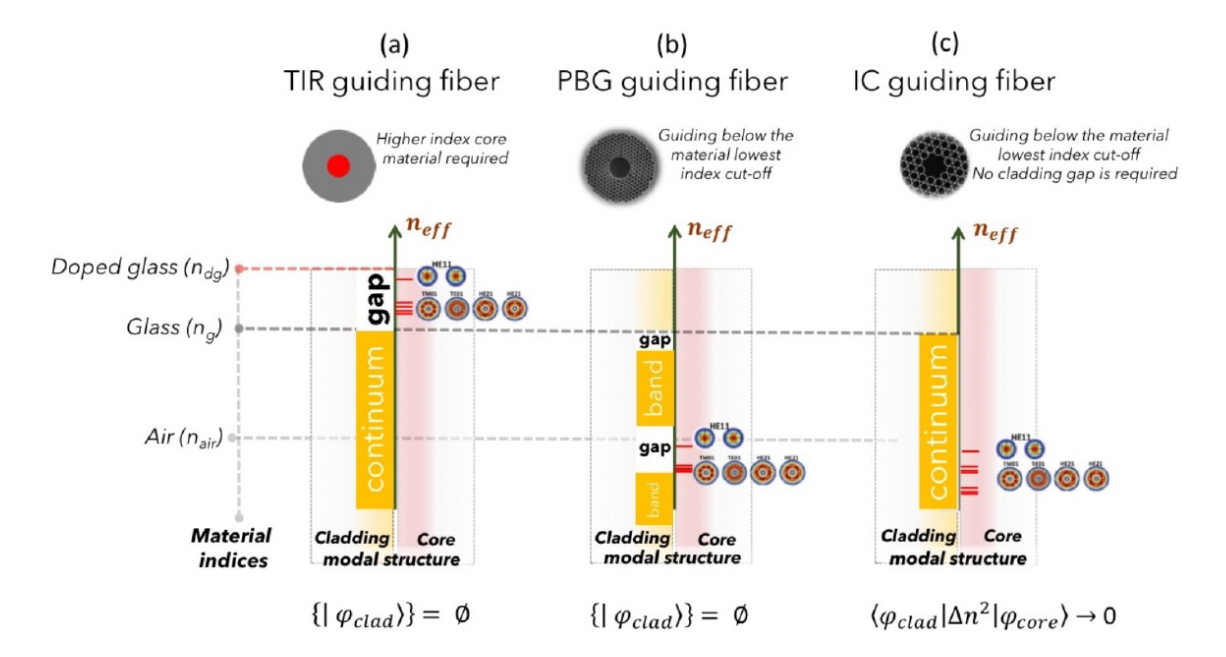


Figure A.5. Modal content representation of the three different optical guiding fibres: (a) Total Internal Reflection (TIR); (b) Photonic Band Gap (PBG); (c) Inhibited Coupling (IC).

A.3 Photodetector Gain

In order to study the photodiode's response to the atomic cloud's photoemission, a Thorlabs Mounted Absorptive Neutral Density (ND) filter with a specified optical density (OD) was installed above it. This setup simulates the few milliwatts of power that will impinge on the photodiode, allowing us to determine the appropriate gain to employ. This ND has a broadband antireflection coating for the 650 - 1050 nm range (near IR) deposited on both surfaces. Optical density (OD) indicates the attenuation factor provided by an optical filter, i.e. how much it reduces the optical power of an incident beam. OD is related to the transmission, T, by the equation [43]:

$$OD = \log_{10}\left(\frac{1}{T}\right) \tag{A.14}$$

where T is a value between 0 and 1. Choosing an ND filter with a higher optical density will translate to lower transmission and greater absorption of the incident light. Sometimes the measure in dB is useful, hence OD can be written also in this way:

$$OD_{dB} = 10\log_{10}\left(\frac{P_{in}}{P_{out}}\right) \tag{A.15}$$

Using the Digital Power Analyzer, we measured the power levels before and after the ND filter (Table A.2). We then examined the response of our photodiode to an input light source and evaluated the effect of different gain levels. Table A.1 illustrates the relationship between the photodiode gain (in dB) and the photodiode voltage (PD) at an OD setting of 34 dB. Multiple ND filters were combined to simulate the low signal levels anticipated in MOT photoemission measurements

Gain (dB)	$PD\left(mV ight)$
0	18
10	32
20	55
30	125
40	348
50	1045
60	3380
70	10420

P_{out} (mW)	OD (dB)	$P_{in} \text{ (mW)}$
0.62	5	1.60
0.58	6	1.60
0.28	10	1.60
0.12	13	1.60
0.0039	34	1.53

Table A.1. Photodiode gain (in dB) and the photodiode voltage (PD) at an OD setting of 34 dB. Table A.2. Power values before (P^{in}) and after (P^{out}) applying the ND filter.

However, the polarizer positioned before the photodiode reduces the power reaching the photodiode. Additionally, we measured the saturation voltage, $V_{sat} = 10.890 \text{ V}$ and $V_{Dark} = 15 \text{ mV}$.

A.4 Saturated Absorption Spectroscopy

Rubidium (85 Rb) atoms exhibit hyperfine splitting on the order of tens or even hundreds of megahertz. In a simple absorption spectroscopy setup, it's often not possible to resolve these hyperfine components due to Doppler broadening. The Doppler width $\Delta\omega_D$ for an atomic transition can be estimated using a Maxwell-Boltzmann velocity distribution at temperature T:

$$\Delta\omega_D = \omega_0 \sqrt{\frac{8 k_B T}{m c^2}},\tag{A.16}$$

where $\omega_0 = 2\pi \times 384$ THz [28] is the transition frequency in the rest frame of the atom, k_B is the Boltzmann constant, $m \simeq 1.41 \cdot 10^{-25}$ kg is the mass of the atom, c is the speed of light, and T is the temperature of the atomic vapor, in this case $\Delta\omega_D \simeq 2\pi \times 520$ MHz. Hence $\Delta\omega_D$ becomes comparable to or larger than the hyperfine splittings.

Saturated absorption spectroscopy (often called Doppler-free spectroscopy) [20] is a technique that overcomes Doppler broadening by exploiting velocity-selective saturation. The setup typically involves two counter-propagating beams:

- A **pump beam**, which is intense enough to saturate the transition for a specific velocity class of atoms.
- A **probe beam**, which is weaker and monitors the absorption at or near the same frequency.

$$\begin{array}{ccc}
\Omega \\
& & \\
\text{Pump} & v \to & \\
& & \\
& & \\
\text{Probe} \\
& & \\
\text{(Weak)}
\end{array}$$

Figure A.6. Basic schematic of a saturated absorption setup, showing a strong pump beam and a weaker probe beam counter-propagating around an atom moving with velocity \vec{v} in the lab reference frame. Here, Ω is the Rabi frequency, proportional to the laser intensity.

In the laboratory frame, an atom moving with velocity \vec{v} experiences different Doppler shifts for each beam:

$$\omega_{\text{probe}} = \omega_L + k_{\text{probe}} \cdot v, \quad \omega_{\text{pump}} = \omega_L - k_{\text{pump}} \cdot v,$$
 (A.17)

where k_{probe} and k_{pump} are the wavevectors of the probe and pump beams, respectively, with the sign convention determined by Fig. A.6, and ω_L is the laser frequency. An atom absorbs a photon if its frequency matches the resonance frequency of a hyperfine atomic transition, denoted ω_0 . Consequently, only those atoms with sufficiently small velocity components along \vec{k} can simultaneously interact with both beams at the unshifted, intrinsic transition frequency. Because the pump beam is intense, it saturates the transition for those atoms, causing them to spend a significant fraction of the time in the excited state and thus reducing their probability of absorbing the probe beam. In effect, a "hole" is burned in the velocity distribution of ground-state atoms that would otherwise absorb at the probe frequency. This phenomenon appears as a narrow peak (or a dip in absorption) when scanning the laser frequency. In many references, this feature is referred to as a Lamb dip or transparency peak [20].

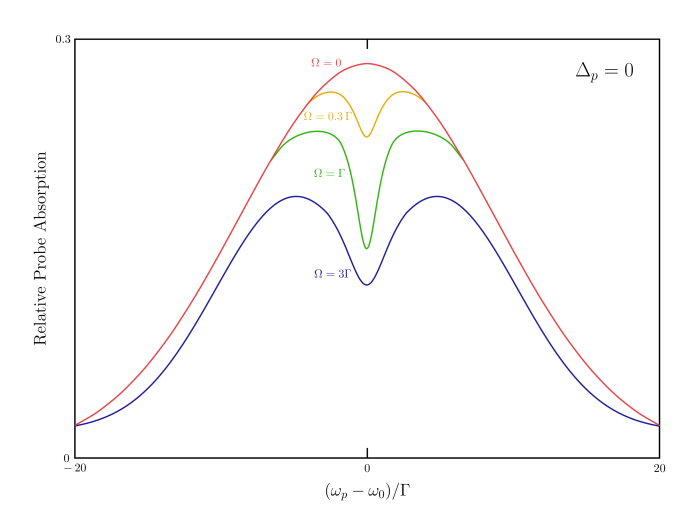


Figure A.7. The saturation spectrum for a degenerate pump-probe pair, i.e. with the same frequency. Without a pump ($\Omega = 0$), we simply get the Doppler-broadened line. As the pump becomes stronger, the dip becomes more pronounced.

Fig. 2.7 shows a the basic arrangement for saturated absorption spectroscopy: a single laser is split into pump and probe paths. The pump beam is sent through the vapor cell in one direction, and the probe beam is sent in the opposite direction, then measured with a photodiode. The resulting saturated absorption profile can exhibit very narrow features (well below the Doppler width), allowing resolution of hyperfine components.

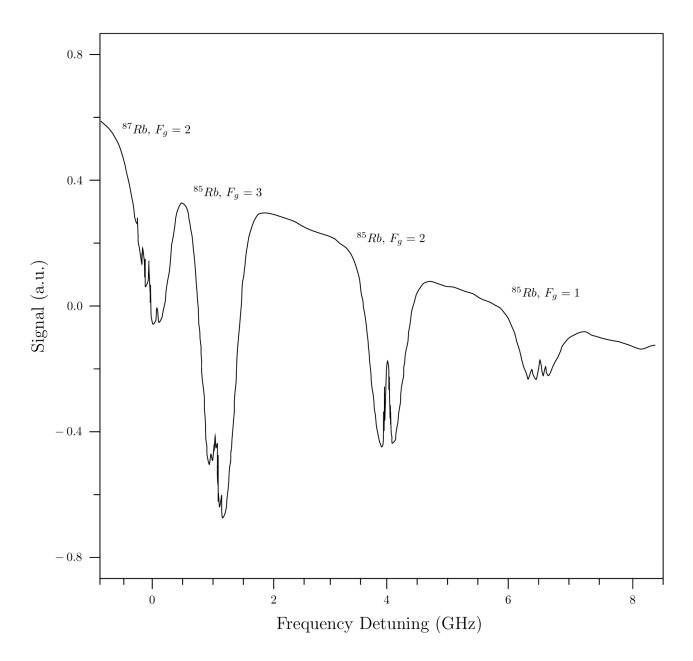


Figure A.8. Saturated absorption spectrum of a Rb vapor.

We have not yet discussed one of the key phenomena in saturated absorption spectroscopy: the crossover resonance. In real, multi-level atoms, two additional features arise: the *crossover resonance* and *optical pumping*, which are associated, respectively, with the presence of multiple upper levels and multiple lower levels to which an excited level can decay.

If multiple transitions lie within the Doppler width, one would naturally expect the saturation spectrum to exhibit a Lamb dip for each individual transition. However, *crossover resonances* introduce additional, narrow absorption dips. Consider the following scenario, as illustrated in Fig. A.9:

- We have two excited energy levels, labeled 1 and 2, with resonance frequencies to the ground state (labeled 0) given by ν_1 and ν_2 , respectively.
- The separation $|\nu_1 \nu_2|$ is smaller than the Doppler width, so without the pump beam the net absorption profile is the sum of two Gaussian lines centered at ν_1 and ν_2 , which would appear as a single broadened absorption profile.

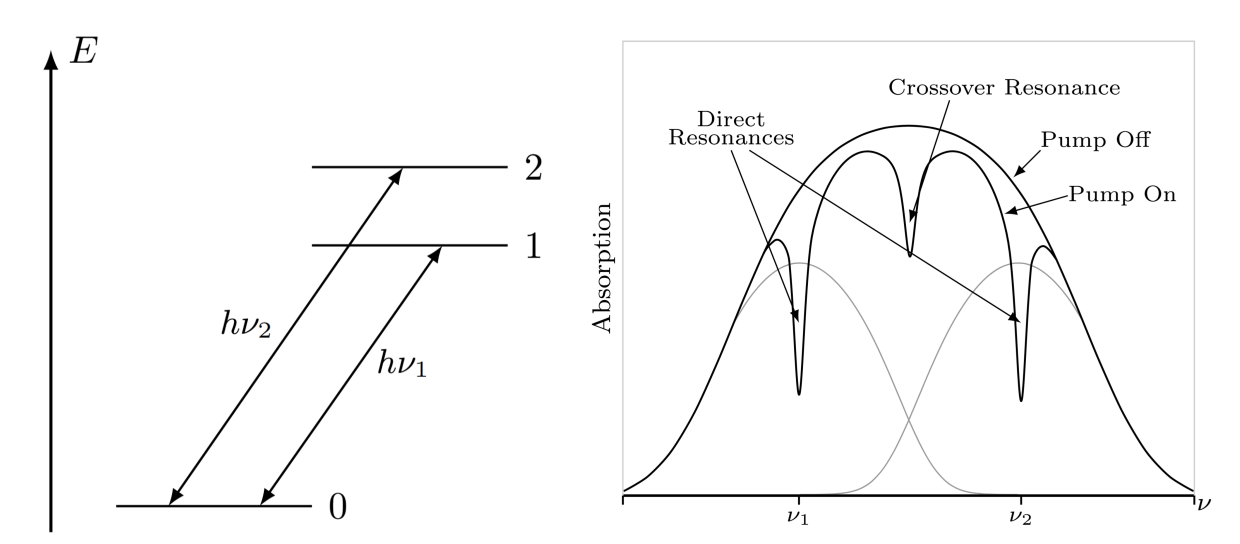


Figure A.9. Schematic of the crossover resonance system.

Figure A.10. Saturated absorption spectrum of a three-level atom.

When the pump beam is turned on, two "holes" are burned in the ground-state velocity distribution at the velocities corresponding to resonance with ν_1 and ν_2 . These velocity classes depend on the laser frequency ω_L . For instance, at $\omega_L = \nu_1$, the probe absorption involving upper state 1 originates from atoms near $v \approx 0$, while the probe absorption involving the higher-energy state 2 comes from some nonzero, positive-velocity atoms. At this frequency, the pump beam burns one hole in the ground state for $v \approx 0$ atoms (due to upper state 1) and another hole for some positive-velocity atoms (due to upper state 2).

As in a two-level system, the hole at $v \approx 0$ reduces absorption to upper state 1 and yields a saturated absorption dip at $\omega_L = \nu_1$. A similar argument shows there is also a saturated absorption dip at $\omega_L = \nu_2$.

A third dip, the crossover resonance, arises at a frequency midway between $\nu_{12} = (\nu_1 + \nu_2)/2$, where the pump and probe beams become resonant with the same velocity group but on different transitions. Atoms in this velocity group are resonantly excited to state 1 by the probe and to state 2 by the pump:

$$\begin{cases} \nu_1 &= \omega_L - k_{probe} v \\ \nu_2 &= \omega_L + k_{pump} v \end{cases} \Rightarrow \begin{cases} 2\omega_L &= \nu_1 + \nu_2 \\ 2k_{pump} v &= 2\nu_2 - \nu_1 \end{cases}$$
 (A.18)

Consequently, the pump beam burns a hole in the ground-state population at the above velocity, and this hole affects the absorption of the probe beam, which is simultaneously interacting with these same velocity. This leads to an additional, narrow dip in the absorption profile precisely at the *crossover* of ν_1 and ν_2 , giving rise to the characteristic crossover resonance observed in saturated absorption spectroscopy.

A.5 87 Rb and 85 Rb D_2 transition hyperfine structure

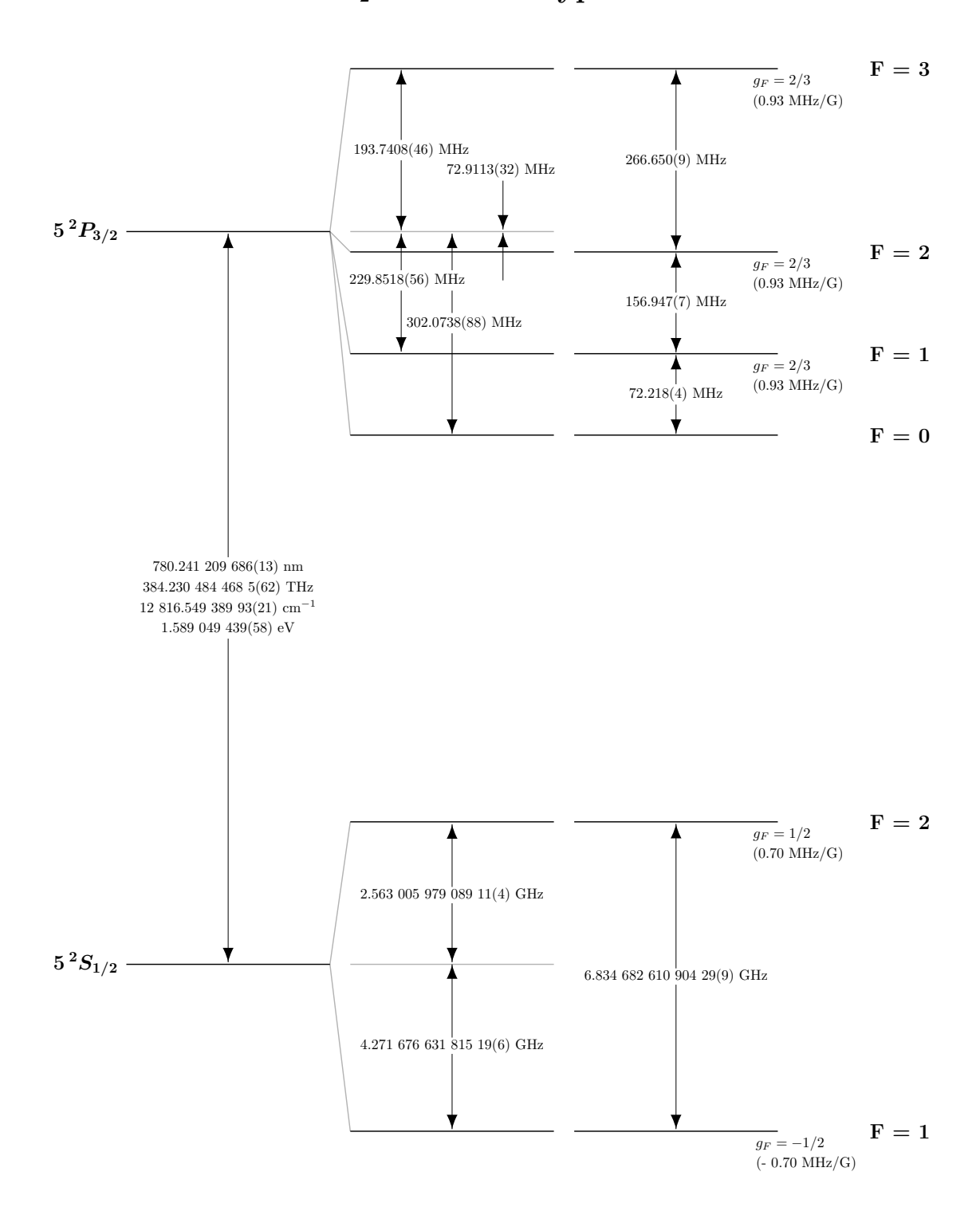


Figure A.11. 87 Rb D_2 transition hyperfine structure, with frequency splittings between the hyperfine energy levels. Credits: [18]

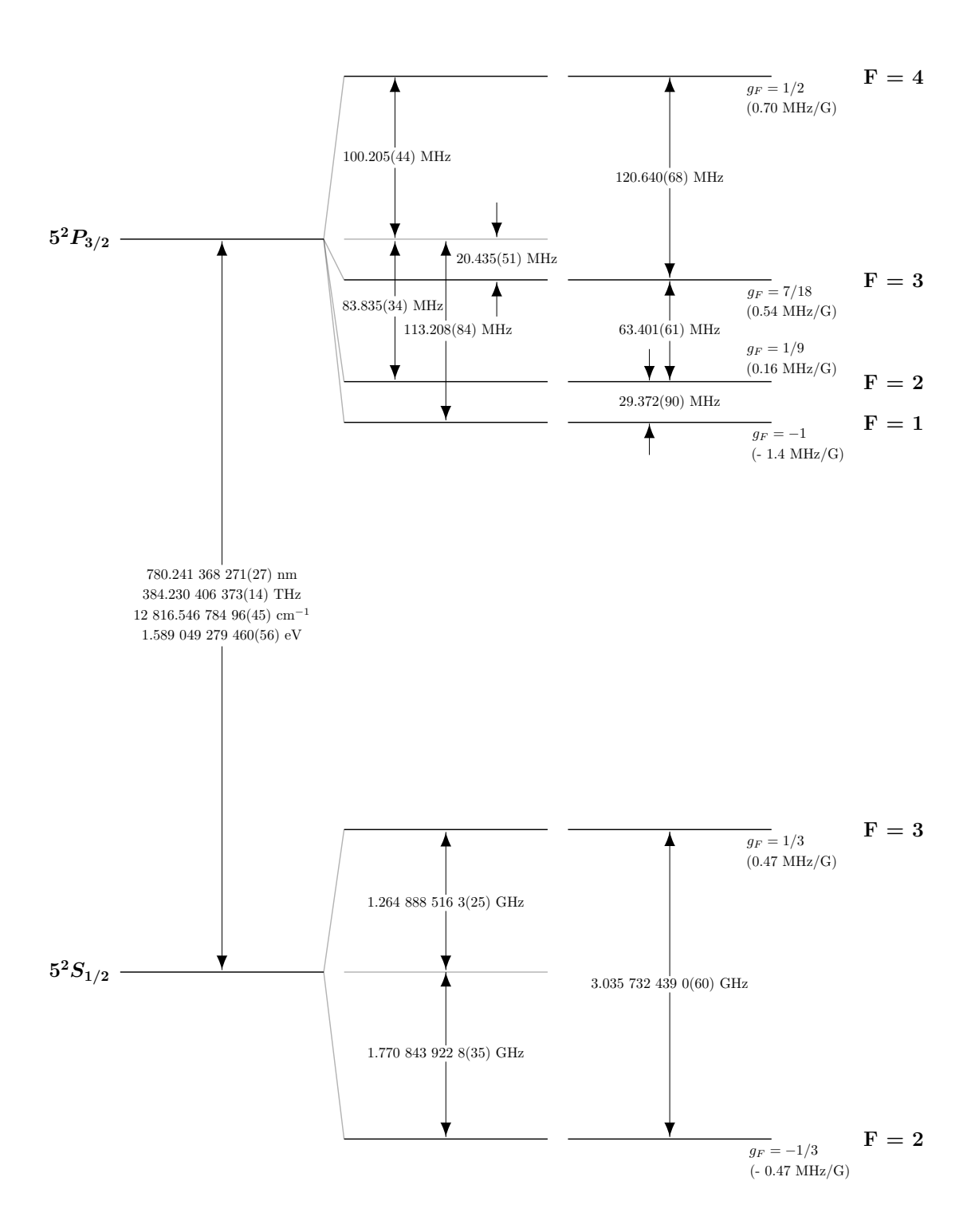


Figure A.12. Rubidium 85 D2 transition hyperfine structure, with frequency splittings between the hyperfine energy levels. Credits: [28]

A.6 Results

A.6.1 Number of atoms estimation-First method

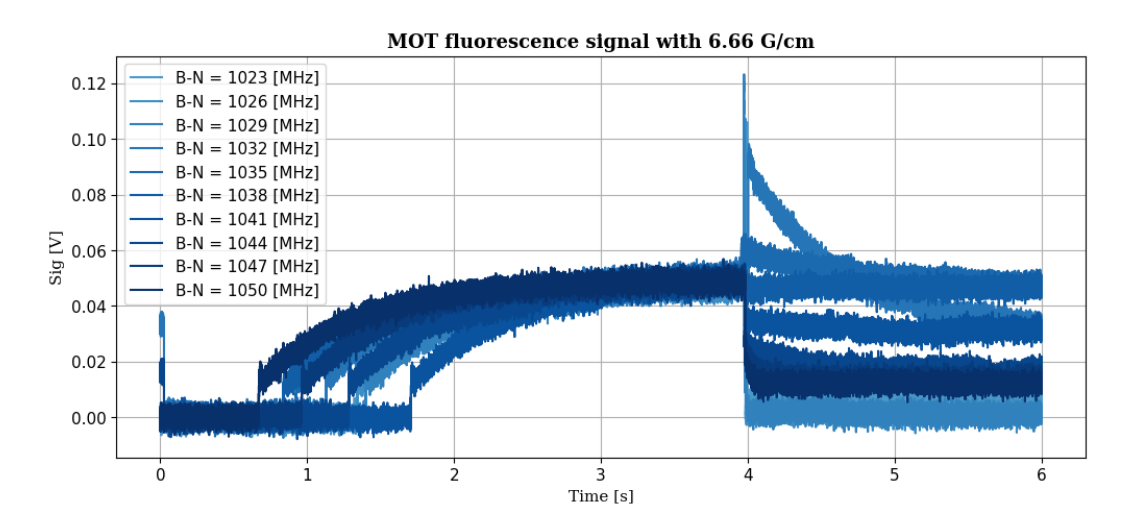


Figure A.13. Capture dynamics of the MOT photoemission for $B' = 6.66 \,\mathrm{G/cm}$, as recorded on the oscilloscope for various beat-note frequencies.

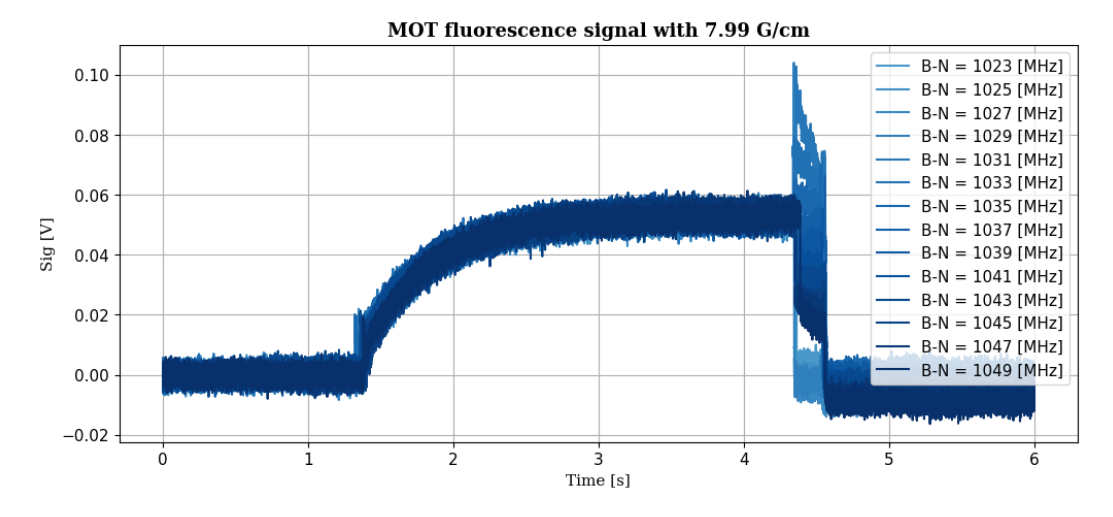


Figure A.14. Capture dynamics of the MOT photoemission for $B' = 7.99 \,\mathrm{G/cm}$, as recorded on the oscilloscope for various beat-note frequencies.

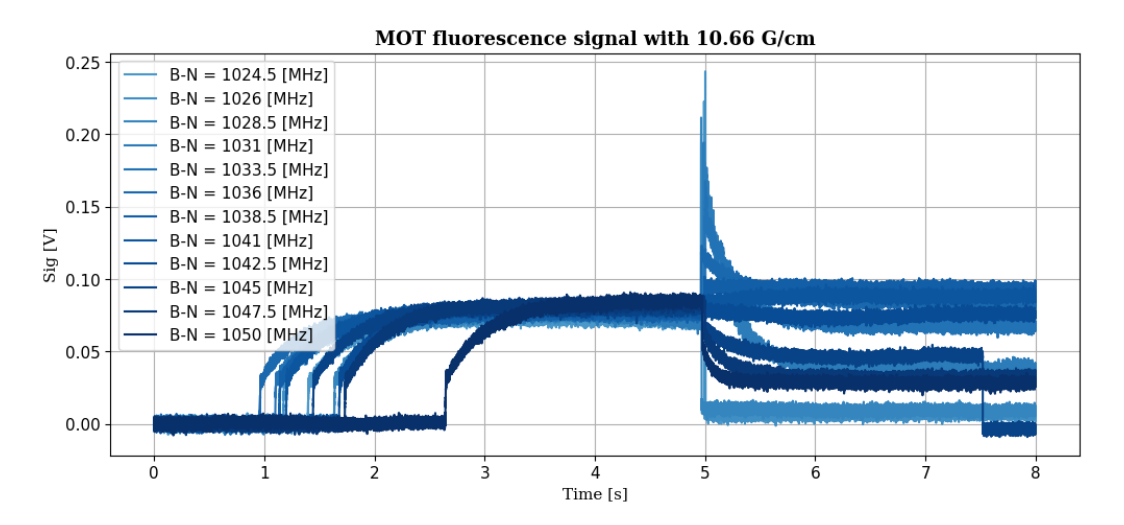


Figure A.15. Capture dynamics of the MOT photoemission for $B' = 10.66 \,\mathrm{G/cm}$, as recorded on the oscilloscope for various beat-note frequencies.

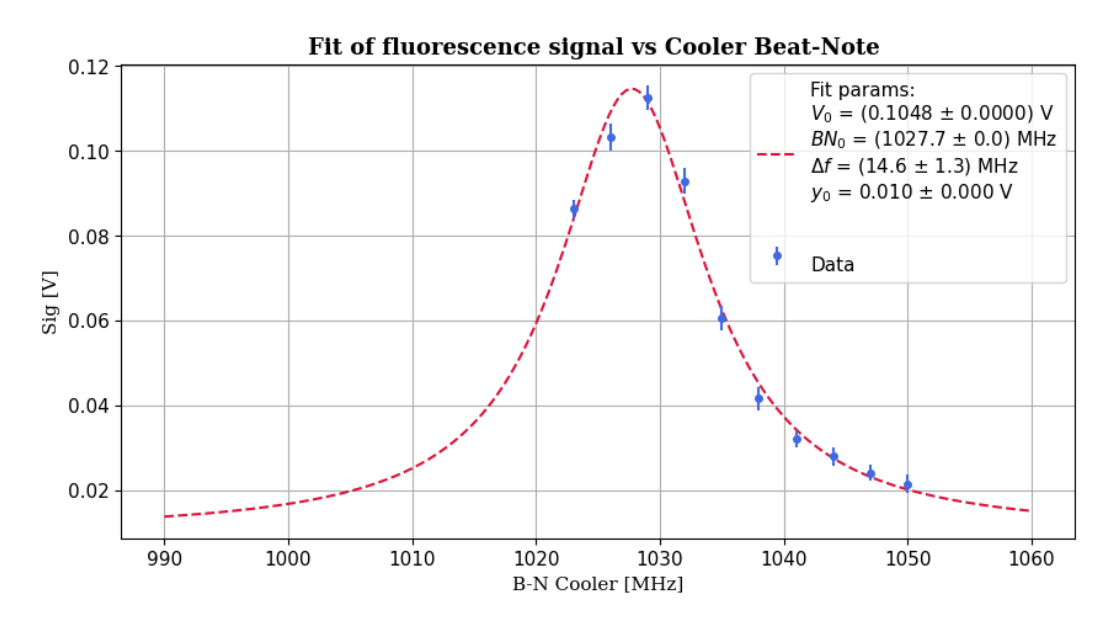


Figure A.16. Lorentzian fit for $B' = 6.66 \,\mathrm{G/cm}$.

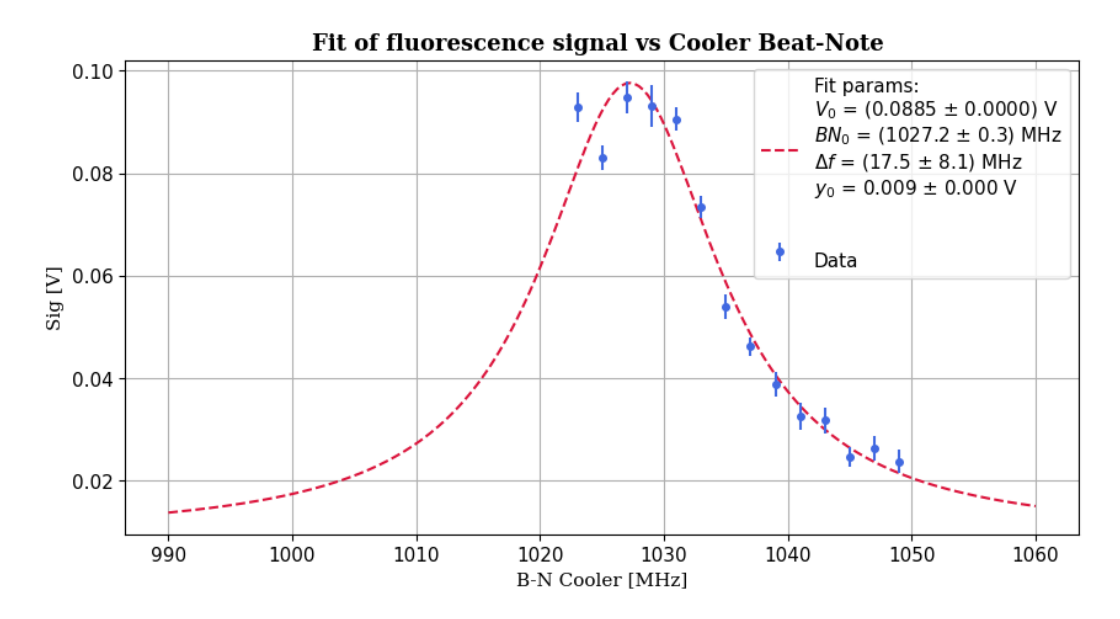


Figure A.17. Lorentzian fit for $B' = 7.99 \,\mathrm{G/cm}$.

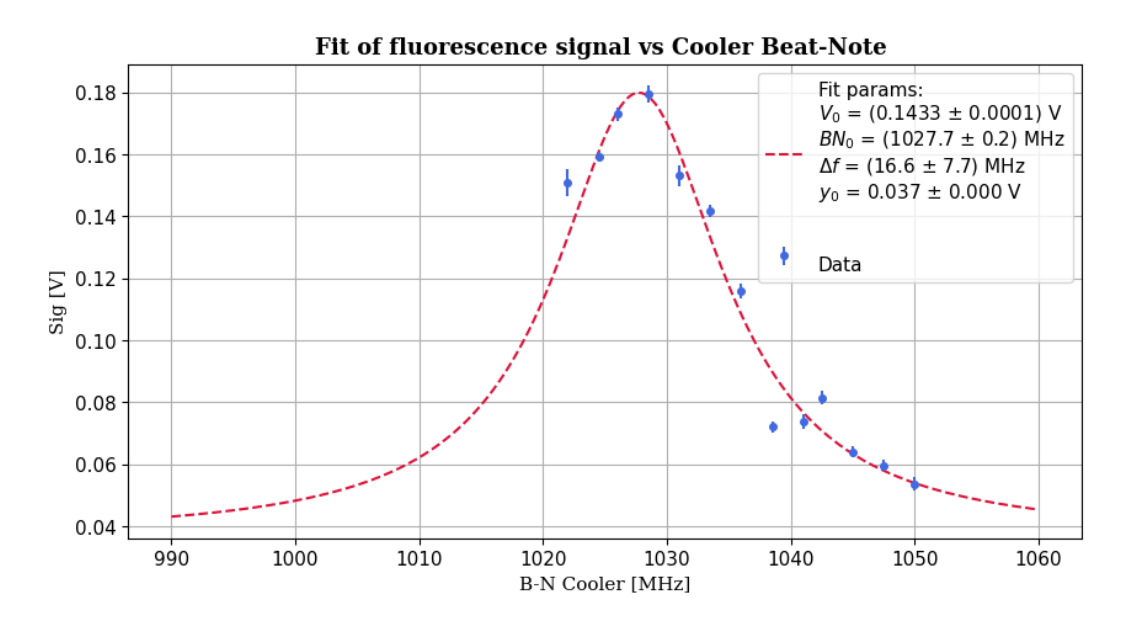


Figure A.18. Lorentzian fit for $B' = 10.66 \,\mathrm{G/cm}$.

A.6.2 Number of atoms estimation-Second method

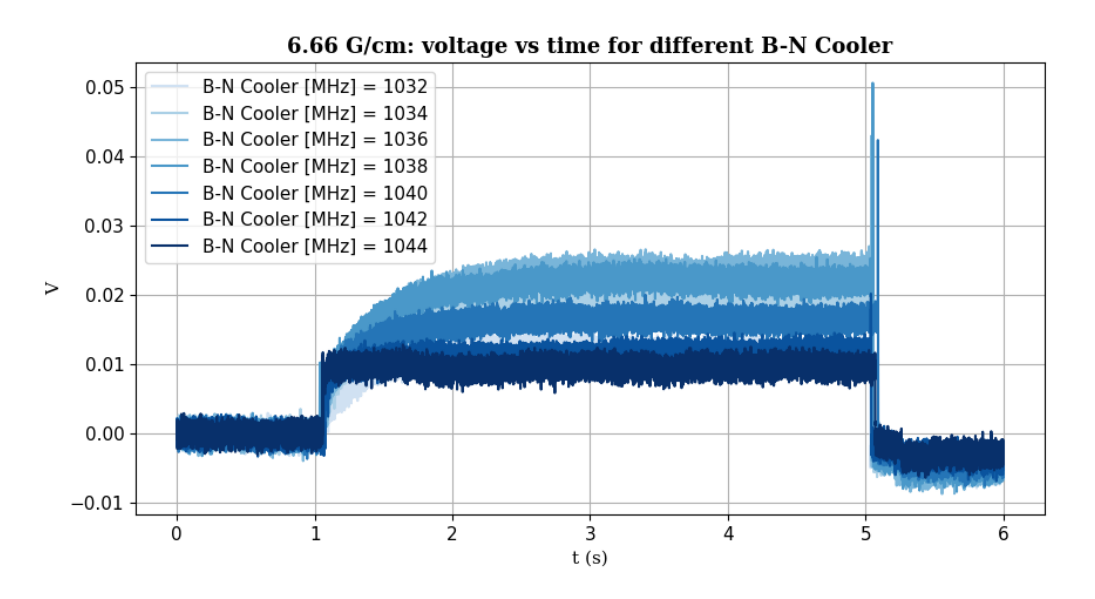


Figure A.19. Time traces of the MOT fluorescence for different cooler beat-note frequencies (from $1032 \,\mathrm{MHz}$ to $1044 \,\mathrm{MHz}$) and magnetic fields gradient $B' = 6.66 \,\mathrm{G/cm}$.

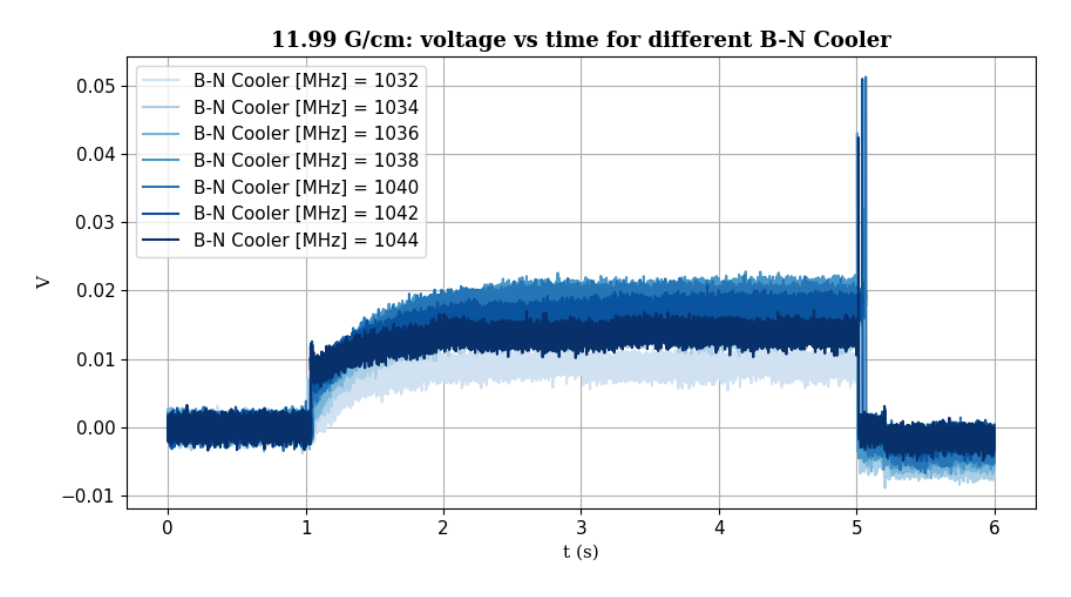


Figure A.20. Time traces of the MOT fluorescence for different cooler beat-note frequencies (from $1032 \,\mathrm{MHz}$ to $1044 \,\mathrm{MHz}$) and magnetic fields gradient $B' = 11.99 \,\mathrm{G/cm}$.

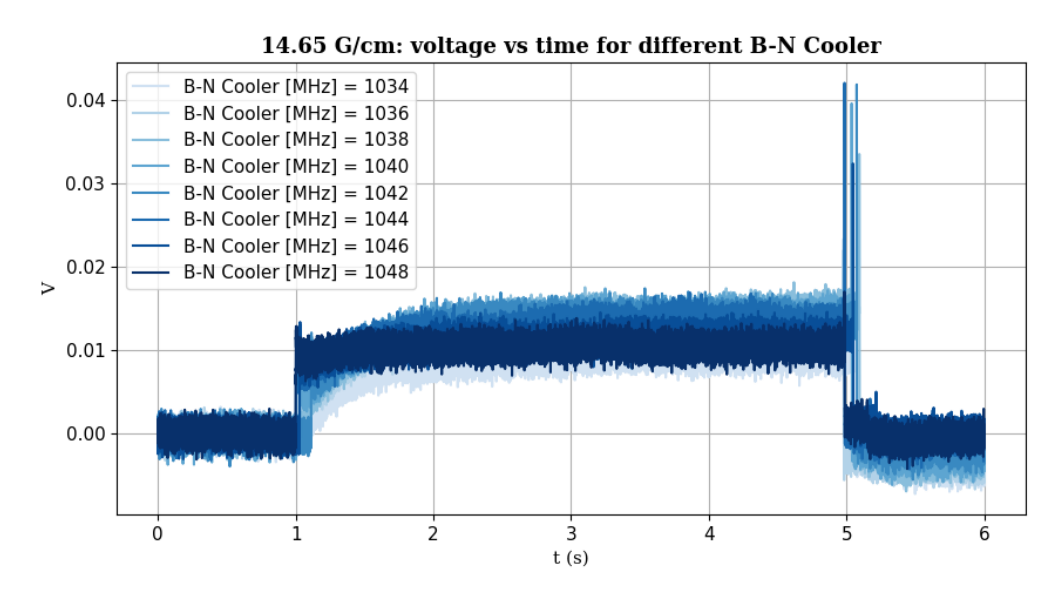


Figure A.21. Time traces of the MOT fluorescence for different cooler beat-note frequencies (from $1032\,\mathrm{MHz}$ to $1048\,\mathrm{MHz}$) and magnetic fields gradient $B'=14.65\,\mathrm{G/cm}$.

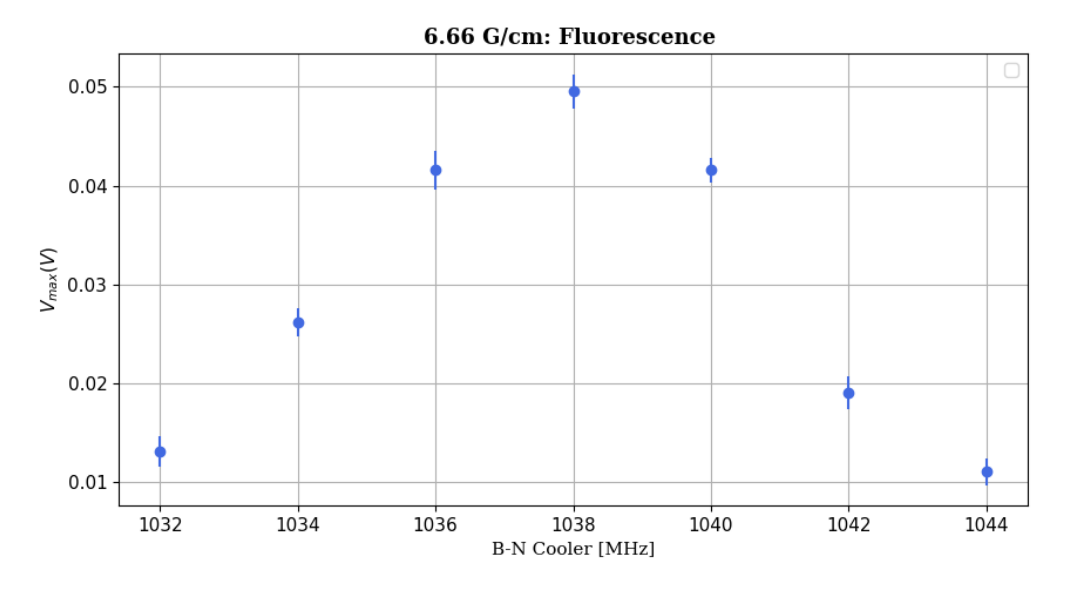


Figure A.22. Measured peak voltages for $B' = 6.66 \,\mathrm{G/cm}$ as a function of the cooler beat-note frequency, with error bars representing the standard deviation of the background subtracted to set the offset.

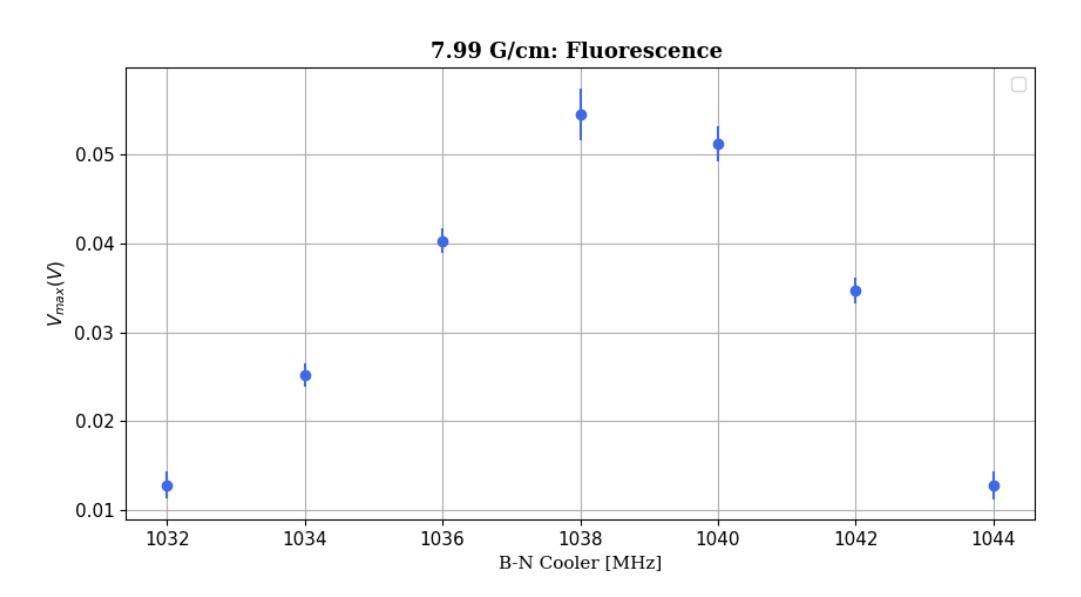


Figure A.23. Measured peak voltages for $B' = 7.99 \,\mathrm{G/cm}$ as a function of the cooler beat-note frequency, with error bars representing the standard deviation of the background subtracted to set the offset.

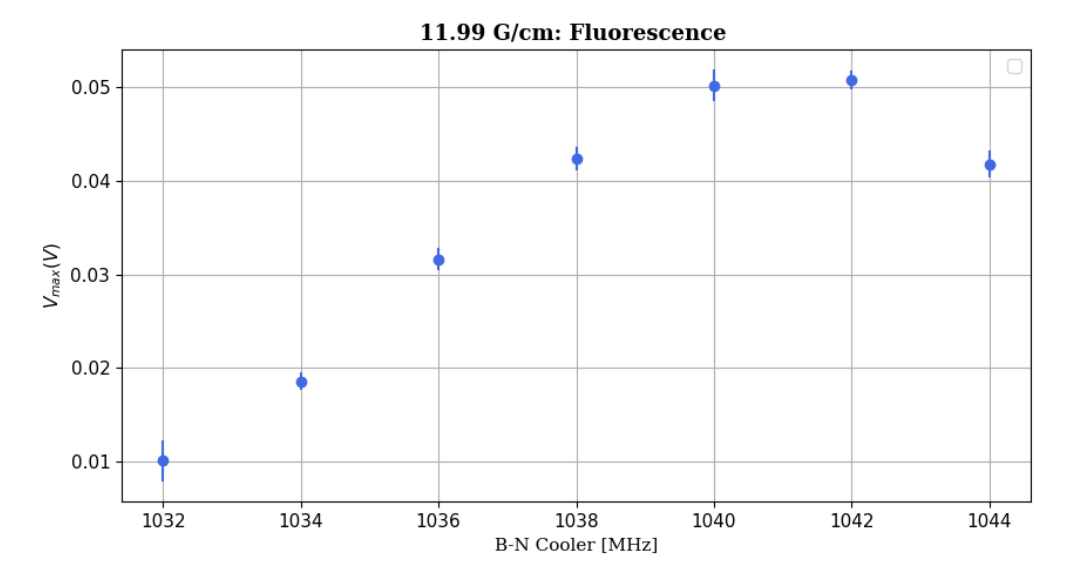


Figure A.24. Measured peak voltages for $B' = 11.99 \,\mathrm{G/cm}$ as a function of the cooler beat-note frequency, with error bars representing the standard deviation of the background subtracted to set the offset.

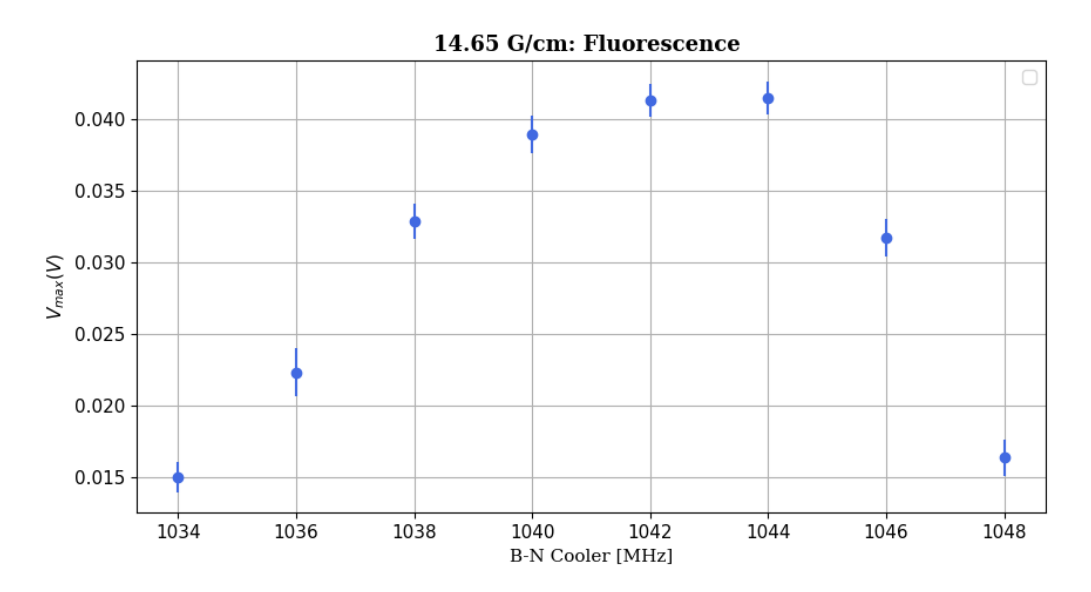


Figure A.25. Measured peak voltages for $B' = 14.65 \,\mathrm{G/cm}$ as a function of the cooler beat-note frequency, with error bars representing the standard deviation of the background subtracted to set the offset.

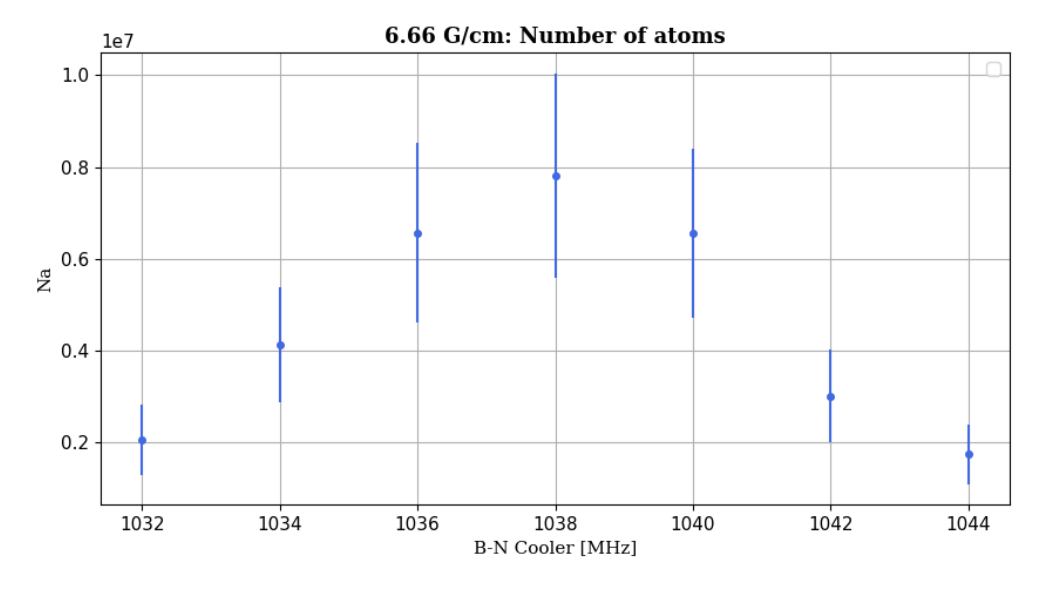


Figure A.26. Number of trapped atoms as a function of the cooler beat-note frequency for $B'=6.66\,G/cm$. The error bars indicate the uncertainties in the atom number measurements.

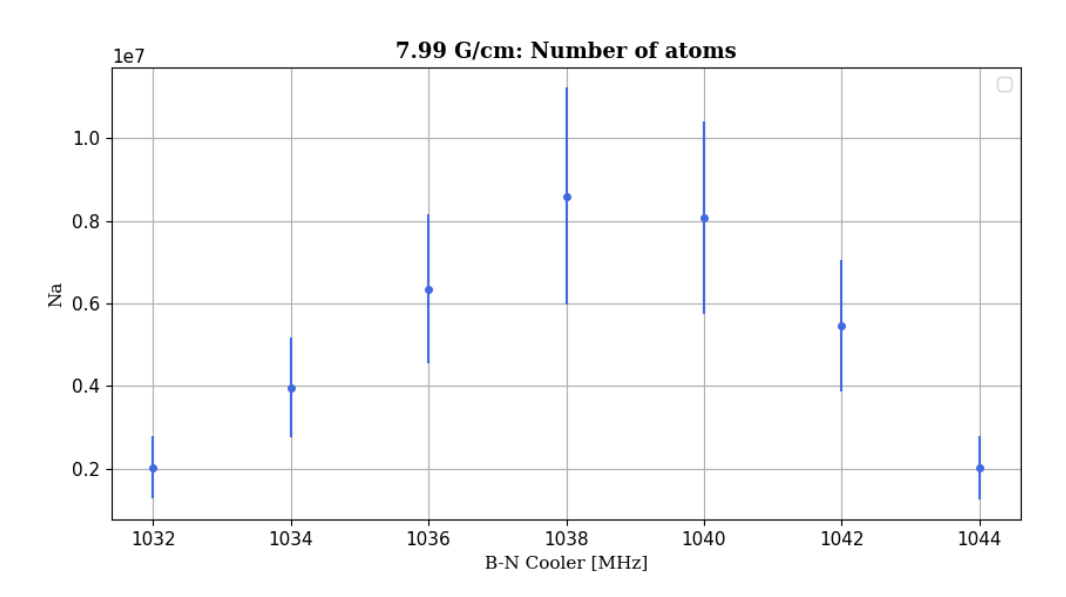


Figure A.27. Number of trapped atoms as a function of the cooler beat-note for $B' = 7.99 \,\text{G/cm}$ frequency for four different magnetic field gradient values .The error bars indicate the uncertainties in the atom number measurements.

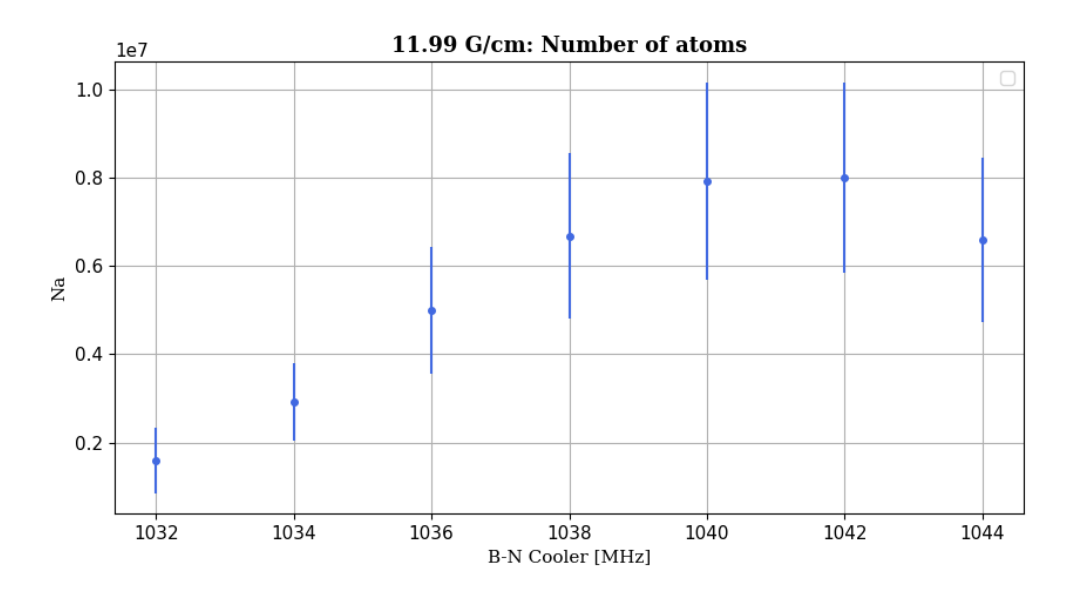


Figure A.28. Number of trapped atoms as a function of the cooler beat-note frequency for $B' = 11.99 \,\mathrm{G/cm}$. The error bars indicate the uncertainties in the atom number measurements.

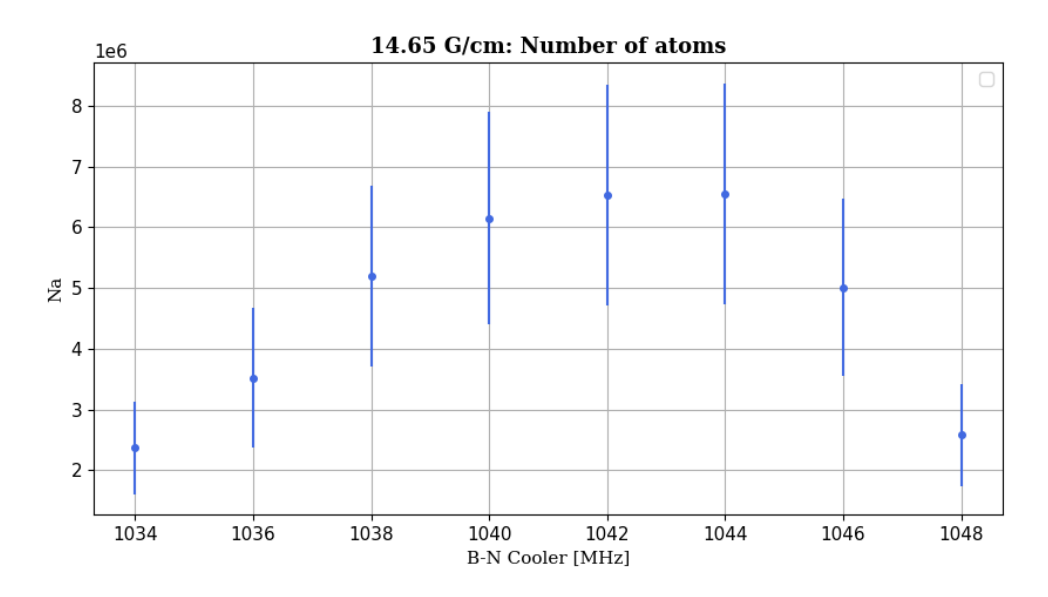


Figure A.29. Number of trapped atoms as a function of the cooler beat-note frequency for $B' = 14.65 \,\mathrm{G/cm}$. The error bars indicate the uncertainties in the atom number measurements.

Bibliography

- [1] T. Hansch and A. Schawlow, "Cooling of gases by laser radiation", *Optics Communications*, vol. 13, pp. 68–69, 1975, DOI: 10.1016/0030-4018(75)90159-5.
- [2] D. J. Wineland and W. M. Itano, "Laser cooling of atoms", Phys. Rev. A, vol. 20, pp. 1521–1540, 4 1979, DOI: 10.1103/PhysRevA.20.1521.
- [3] "The Nobel Prize in Physics 1997". Accessed: 2025. (1997), Available: https://www.nobelprize.org/prizes/physics/1997/advanced-information/.
- [4] C. Degen, F. Reinhard, and P. Cappellaro, "Quantum sensing", Reviews of Modern Physics, vol. 89, p. 035002, 2017, DOI: 10.1103/RevModPhys.89.035002.
- [5] E. Riis *et al.*, "Compact platforms for cold-atom clocks", in *Laser Science*, Optica Publishing Group, 2024, FM1A–1, DOI: 10.1364/LS.2024.FM1A.1.
- [6] J. Wang et al., "Cold atom interferometers and their applications in precision measurements", Frontiers of Physics in China, vol. 4, pp. 179–189, 2009, DOI: 10.1007/s11467-009-0045-3.
- [7] J. Lim, H.-g. Lee, and J. Ahn, "Review of cold Rydberg atoms and their applications", Journal of the Korean Physical Society, vol. 63, pp. 867–876, 2013, DOI: 10.3938/jkps.63. 867.
- [8] P. Jessen and I. Deutsch, "Optical Lattices", Advances in Atomic, Molecular and Optical Physics, vol. 37, pp. 95–138, 1996.
- [9] A. Einstein, "Quantentheorie des einatomigen idealen gases", Sitzungsberichte der Königlich Preußischen Akademie der Wissenschaften, vol. 261, pp. 1914–1932, 1924.
- [10] T.-F. Zhang et al., "Supersolid phase of cold atoms", The European Physical Journal D, vol. 74, pp. 1–13, 2020, DOI: 10.1140/epjd/e2020-10127-3.
- [11] C. C. Gerry and P. L. Knight, *Introductory Quantum Optics*. Cambridge University Press, 2005.
- [12] C. Cohen-Tannoudji, Atomic motion in laser light. Elsevier Science Publishers B.V., 1992.
- [13] V. F. Weisskopf and E. Wigner, "Berechnung der naturlichen Linienbreite auf Grund der Dirac schen Lichttheorie", Z. Phys., vol. 63, pp. 54–73, 1930, DOI: 10.1007/BF01336768.
- [14] M. I. Sargent, M. O. Scully, and W. E. J. Lamb, Laser physics. Westview Press, 1974.
- [15] A. Einstein, "On the quantum theory of radiation", Physik. Zeit., vol. 18, p. 121, 1917.
- [16] P. W. Milonni, "Why spontaneous emission?", American Journal of Physics, vol. 52, p. 340, 1984, DOI: 10.1119/1.13886.

- [17] H. J. Metcalf and P. van der Straten, Laser Cooling and Trapping. Springer, 1999.
- [18] Steck, Daniel Adam, Rubidium 87 D Line Data, Los Alamos National Laboratory, 2003, Available: http://steck.us/alkalidata/rubidium87numbers.pdf.
- [19] Cohen-Tannoudji, C., "Manipulating atoms with photons", Reviews of Modern Physics, vol. 70, p. 707, 1998, DOI: 10.1103/RevModPhys.70.707.
- [20] D. A. Steck, Quantum and Atom Optics. Department of Physics, University of Oregon, 2007.
- [21] L. F. Loranca Cruz, "Towards atomic crystallization in a hollow-core fiber", Ph.D. dissertation, Université de Bordeaux, 2024.
- [22] R. Grimm, M. Weidemuller, and Ovchinnikov, "Optical dipole traps for neutral atoms", Advances in Atomic, Molecular and Optical Physics, vol. 42, pp. 95–170, 2000, DOI: 10.1016/S1049-250X(08)60186-X.
- [23] K. Kowalski et al., "Magneto-optical trap: Fundamentals and realization", Computational Methods in Science and Technology Special Issue (2), pp. 115–129, 2010, DOI: 10.12921/ cmst.2010.SI.02.115-129.
- [24] P. J. Ungar *et al.*, "Optical molasses and multilevel atoms: Theory", *J. Opt. Soc. Am. B*, vol. 6, no. 11, p. 2058, 1989, DOI: 10.1364/JOSAB.6.002058.
- [25] M-Marqe. "MOT_setup_cads-at-DIFA_unibo". (2024), Available: https://github.com/M-Marqe/MOT_setup_CADs-at-DIFA_UniBo.
- [26] M. Marchesini, "A new magneto-optical trap for cold atoms in hollow-core fibers", Ph.D. dissertation, Alma Mater Studiorum Università di Bologna, 2025.
- [27] H. V. SAES, Nextorr Z 200, 2024, Available: https://www.saesgetters.com/highvacuum/solution/nextorr-d-z-uhv/.
- [28] D. A. Steck, *Rubidium 85 D Line Data*, Oregon Center for Optics and Department of Physics, University of Oregon, 2001, Available: http://steck.us/alkalidata/rubidium85numbers.pdf.
- [29] I. Thorlabs, *PDA100A-EC Si Switchable Gain Detector*, Rev F, 2017, Available: https://www.thorlabs.de/thorProduct.cfm?partNumber=PDA100A.
- [30] C. G. Townsend *et al.*, "Phase-space density in the magneto-optical trap", *Physical Review A*, vol. 52, no. 2, pp. 1423–1423, 1995, DOI: 10.1103/physreva.52.1423.
- [31] K. Lindquist, M. Stephens, and C. Wieman, "Experimental and theoretical study of the vapor-cell zeeman optical trap", *Physical Review A*, vol. 46, pp. 4082–4090, 1992, DOI: 10.1103/PhysRevA.46.4082.
- [32] C. Monroe *et al.*, "Very Cold Trapped Atoms in a Vapor Cell", *Physical Review Letters*, vol. 65, pp. 1571–1571, 1990, DOI: 10.1103/PhysRevLett.65.1571.
- [33] F. Reif, Fundamentals of Statistical and Thermal Physics. McGraw-Hill, 1965.
- [34] T. Arpornthip, C. A. Sackett, and K. Hughes, "Vacuum-pressure measurement using a magneto-optical trap", *Physical Review A*, vol. 85, p. 033420, 2012, DOI: 10.1103/PhysRevA.85.033420.

- [35] M. Haw et al., "Magneto-optical trap loading rate dependence on trap depth and vapor density", Optical Society of America, vol. 29, pp. 475–483, 2012, DOI: 10.1364/JOSAB. 29.000475.
- [36] S. D. Gensemer *et al.*, "Trap-loss collisions of 85^rband87^rb: Dependence on trap parameters", *Physical Review A*, vol. 56, p. 4055, 1997, DOI: 10.1103/PhysRevA.56.4055.
- [37] A. MicroSystems, A3507-8 hall-effect sensor datasheet, Accessed: 2001, 2001, Available: https://www.allegromicro.com/-/media/files/datasheets/a3507-8-datasheet.ashx.
- [38] G.-D. Peng, Ed., Handbook of Optical Fibers. Springer, 2019.
- [39] M. Born and E. Wolf, *Principles of optics*. Cambridge University Press, 1959.
- [40] B. E. A. Saleh and M. C. Teich, *Fundamentals of Photonics* (Wiley Series in Pure and Applied Optics), Third. Wiley, 2019.
- [41] F. O. Center, *Polarization-maintaining fibers explained*, Accessed: 2021, 2021, Available: https://focenter.com/blog/polarization-maintaining-fibers-explained.
- [42] B. Debord *et al.*, "Hollow-core fiber technology: The rising of "gas photonics"", *Fibers*, vol. 7, p. 16, 2019, DOI: 10.3390/fib7020016.
- [43] Thorlabs, Ne03a-b neutral density filters, Accessed: 2000, 2000, Available: https://www.thorlabs.com/newgrouppage9.cfm?objectgroup_id=6274&pn=NE03A-B.